# The Portevin-Le Chatelier effect in nickel-base superalloys: Origins, consequences and comparison to strain ageing in other alloy systems

B.S. Rowlands [a], C. Rae [a], E. Galindo-Nava [b,*]

[a] Department of Materials Science, University of Cambridge, Cambridge CB3 0FS, United Kingdom
[b] Department of Mechanical Engineering, University College London, Torrington Place, London WC1E 7JE, United Kingdom

A B S T R A C T

Dynamic Strain Ageing (DSA) has reached widespread acceptance since its proposal in the 1940's as the mechanism behind the Portevin-Le Chatelier effect in ferritic steels. However, it remains an open question as to whether the classical mechanism can be extended to Face-Centred Cubic (FCC) alloys, including nickel-based superalloys, as often implicitly assumed. Given the historical link between serrated flow and loss of ductility in steels, understanding such consequences in superalloys used in key components of a jet engine demands attention. This review compares plastic instabilities in superalloys to those in ferritic steels, including the effects of temperature, strain rate, compositional, microstructural and extrinsic testing parameters on the extent of serrated flow and consequences on mechanical properties. Outstanding issues are discussed in detail, relating both to the lack of a complete experimental argument depicting the origins of serrated flow and different serration 'Types', as well as the inability of current predictive models to fully account for multiscale experimental observations. Proposed explanations for plastic instabilities in FCC alloys are discussed, including but not limited to classical DSA, with the aim to guide future experiments to elucidate the origins of serrated flow across length scales and improve key properties such as fatigue life.

## 1. Introduction

As demand for air travel continues to increase, meeting climate change targets provides ongoing motivation for technological advancements to increase turbine engine efficiency [1]. However, achievable turbine entry temperatures and, by extension, efficiency are ultimately limited by material failure of the most demanding components. Polycrystalline nickel-based superalloys remain the material of choice for turbine discs, but there is a constant drive to improve their high temperature and stress capabilities, to which an understanding of their deformation mechanisms is fundamental for accurate service life predictions. While the high temperature creep properties of single crystal blade superalloys have been extensively researched, to the point where creep is no longer always considered the life limiting factor [2], a full picture of the intermediate temperature deformation mechanisms is still emerging, particularly around the temperatures experienced by the turbine disc in practice [3]. One aspect of this is the widespread tendency to demonstrate a plastic instability termed serrated flow (Section 2).

---
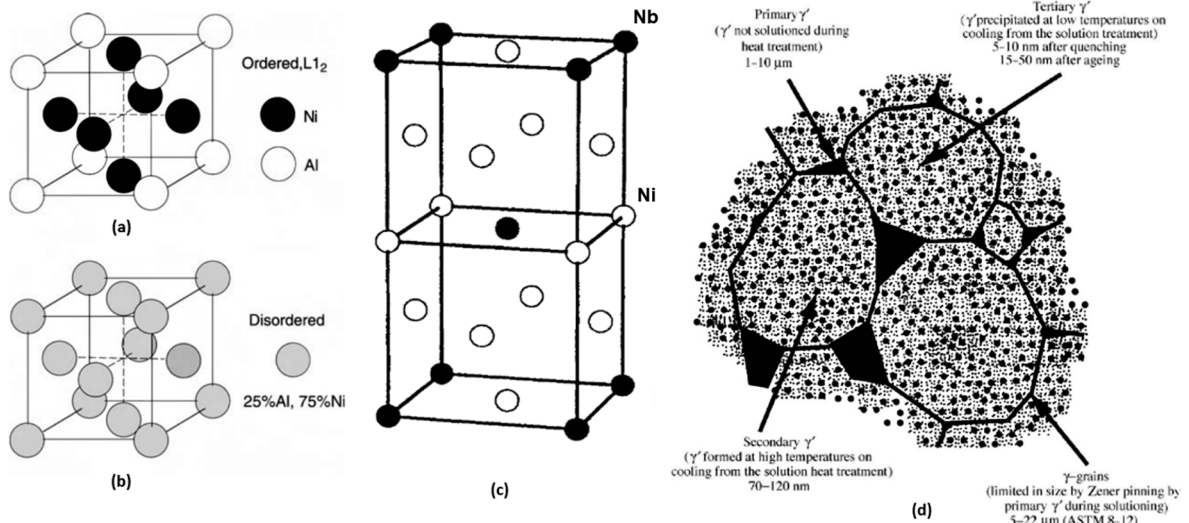
**Fig. 1.** Crystal structures of the main phases in nickel-base superalloys (a) $\gamma'$ $Ni_3Al$ (b) $\gamma$ (Ni) (c) $\gamma''$ $Ni_3Nb$ [25,33]. (d) Microstructure of a subsolvus heat treated superalloy [34].

From a technological perspective, serrated flow is often considered undesirable due to its relation to the formation of stretcher-strain surface markings during forming of sheet steel [4], for instance in automobile manufacture. However, this is not particularly relevant during turbine disc manufacture: such markings are usually most prevalent in thin sheet applications (Section 2.4) and in practice, high strength superalloys are typically powder processed to near net shape, with the forging window for subsequent deformation exceeding the temperature range of serrated flow.

Serrated flow may, however, be an important consideration during service. Typical temperatures experienced by the turbine disc range from 400 °C at the bore up to 750 °C at the rim [5], close to the range of plastic instability, around 200 °C – 650 °C [6]. Serrated flow is often associated with a loss of ductility (Section 4.3) [7,8]. However, a ductility minimum is often not clearly attributable to serrated flow in superalloys [9]. Besides a need to clarify its effect on fracture and fatigue (Sections 4.3 and 4.4), serrated yielding is believed to derive from an intermediate temperature strengthening mechanism with the unusual property of decreasing in strength with increasing strain rate, termed a negative Strain Rate Sensitivity (SRS) [10], for instance due to Dynamic Strain Ageing (DSA; Section 3.2). Its exploitation may be of particular concern during engine overspeed [11], referring to a rapid acceleration and increased centrifugal forces on a disc resulting from a loss of load, for instance through failure of the shaft connecting the discs to the compressors [12] and possibly causing a disc burst [12]. Such a failure is considered hazardous as the engine casing is generally not designed to contain the resulting high-energy debris. The negative SRS of the flow stress and ultimate tensile strength accompanying serrated flow means that the high stresses and strain rates resulting from overspeed may coincide with a reduced failure stress.

The concept of DSA [13–19] as the origins of serrated flow in Body-Centred Cubic (BCC) steels is widely accepted, but the extension of strain ageing from BCC steel to Face-Centred Cubic (FCC) alloys is not trivial. Concerns have been raised in some alloys such as Al-Mg [20], Twin-Induced Plasticity (TWIP) steels [21] and superalloys [22] as to whether the temperatures at which serrations are observed are sufficient for long range atomic diffusion to occur. There is wide agreement that the diffusion of solute atoms remains responsible for locking at intermediate temperatures in FCC alloys [23,19], but alternate microscopic mechanisms for solute–defect locking interactions have been proposed (Section 3.3), the details of which lack an accepted explanation. While others use the term DSA more generally e.g. [21,24,20] to encompass such solute locking mechanisms of serrated flow, these are distinguished here by taking DSA to refer only to the classical mechanisms of strain ageing, involving long range diffusion of interstitial or substitutional solute to dislocation cores and elastic locking (Section 3.2). Coupled with a lack of experimental substantiation, details of the mechanisms of serrated flow in several FCC alloys remain unelucidated. Even if strain ageing operates in superalloys, several points require clarification on account of their microstructural and compositional complexity. Section 1.1 briefly describes some well known general aspects of superalloy metallurgy to highlight this point. Clarifying the identity of the interacting solutes, defects and phases in which locking occurs requires careful experimentation.

Furthermore, several experimental features of serrated flow are not fully captured by current accepted models for DSA, in particular regarding the origins of the so-called 'inverse' trend in the critical strain at which serrations begin, despite possible explanations (Section 3.2.2). Moreover a complete explanation is lacking of the link between the atomistic mechanism of DSA and the observation of macroscopic serrations and propagating or non-propagating bands of localised deformation under different conditions, as discussed in Section 3.2.3.

This article aims to review the current understanding of serrated flow in FCC alloys in detail, with a focus on superalloys but drawing comparison to other alloys showing serrated flow in cases.
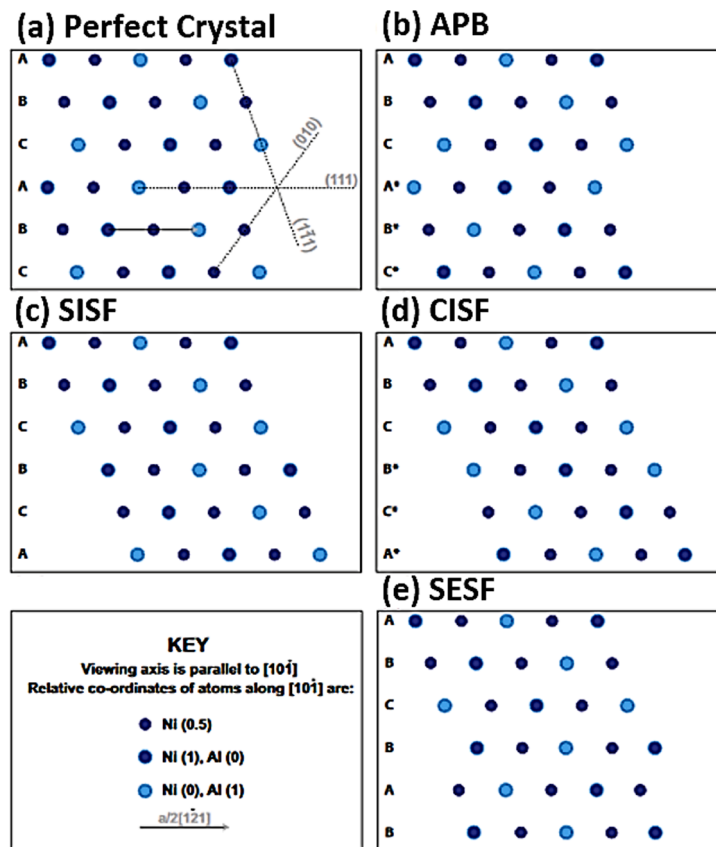
**Fig. 2.** Planar faults in $\gamma'$. Labels A, B and C refer to the packing sequence of {111} planes. * Represents a displacement by a/2<110>{111} from (a) the perfect packing sequence. Translation of bottom half crystal by: (b) a/2[10$\bar{1}$] generates an APB; (c) a/3[1$\bar{2}$1] generates a Superlattice Intrinsic Stacking Fault (SISF) and (d) a/6[$\bar{1}$2$\bar{1}$] generates a Complex Intrinsic Stacking Fault (CISF). (e) Translating two adjacent layers generates a Superlattice Extrinsic Stacking Fault (SESF) [39].

### 1.1. Superalloy metallurgy

Typical superalloys consist of two main phases: a disordered FCC matrix termed $\gamma$ (Fig. 1)) and coherent precipitates of an ordered L1$_2$ phase (Fig. 1(a)), termed $\gamma'$ [25], which confer an anomalous increase in strength [26] with temperature without coarsening. The $\gamma'$ phase has nominal composition Ni$_3$Al, but other $\gamma'$ stabilising elements such as Ti, Ta and Nb are commonly added, substituting on Al sites and raising the energy of the Anti Phase Boundary (APB) formed by passage of a superpartial dislocation. Heat treatments typically lead to a bi- or trimodal precipitate distribution (Fig. 1(d)), depending on whether the homogenisation heat treatment applied to reduce segregation was applied above or below the solvus of the primary $\gamma'$ formed on casting or powder processing, allowing grain size control to balance between fracture toughness and creep resistance [27]. The duration [28], temperature [29] and cooling rate [30] from each heat treatment stage are carefully controlled such that the tertiary $\gamma'$ precipitates have a size close to that for optimal strength [31]. Some Nb-containing commercial superalloys such as IN718 may instead form the orthorhombic D0$_{22}$ $\delta$ phase in equilibrium. This phase precipitates incoherently, offering little strengthening effect, but is often slow to precipitate at temperatures under 800 °C [32]. Instead, metastable Body-Centred Tetragonal (BCT) $\gamma''$ precipitates (Fig. 1(c)) are the main strengthening precipitate, which form coherently at lower temperatures [32]. Elements such as Mo, W, Co and Cr are added as substitutional solute strengtheners. Their addition confers several other beneficial properties: Cr forms a passivating scale for corrosion resistance at temperatures below 800 °C, whereas W reduces the diffusivity of the matrix and hence creep rates. The amount of solid solution strengtheners added is usually such that the matrix is unstable with respect to the formation of Topologically Close Packed (TCP) phases [35,36], which embrittle the disc if allowed to form, but these are usually slow to precipitate [37]. C, B and Zr are typically added as grain boundary strengtheners. These elements segregate to grain boundaries and may form carbides and borides which pin grain boundaries, preventing sliding during creep [38].

The most common slip system in FCC metals is a/2<110>{111}, which dissociates into pairs of a/6<112>{111} partial dislocations. The Burgers vectors of such dislocations are not lattice vectors in the $\gamma'$ phase, so their passage generates various planar faults (Fig. 2).

While deformation maps are not widely available for intermediate temperature monotonic tensile tests in superalloys, creep tests
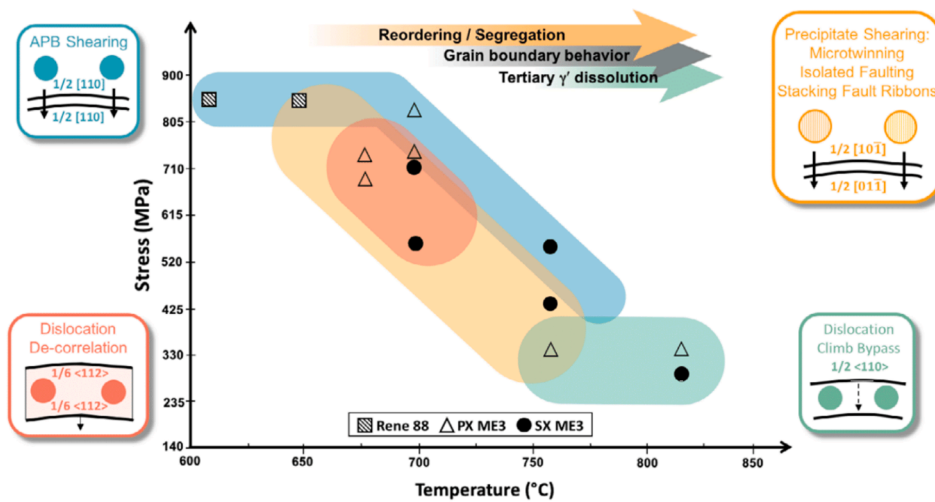
**Fig. 3.** Deformation mechanism map during creep for several turbine disc superalloys [40].
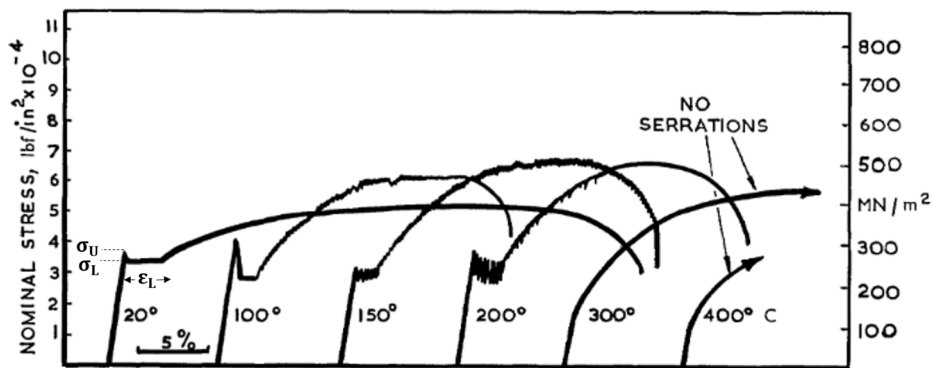


**Fig. 4.** Stress (ordinate) - strain (abscissa) curve of a 0.05 wt.% C mild steel deformed at $10^{-4}$ s$^{-1}$ from 20 °C – 400 °C, showing serrated yielding. The initial upper yield point, $\sigma_U$, lower yield point, $\sigma_L$, and Lüders extension, $\varepsilon_L$, are labelled [60].

commonly show a change in deformation mechanism with temperature [40,41], Stacking Fault Energy (SFE) [42–44] and precipitate fraction [45,42] from the shear of a/2<110>{111} pairs bounded by an APB under 600 °C to Stacking Fault (SF) shear modes related to the deformation by a/6<112>{111} partial dislocations (Fig. 3). Such SF shear modes are characterised by dislocation dissociation and combination reactions of perfect and partial dislocations to form a lower energy fault plane than the APB, enabling glide at lower stresses than that for APB shear. For instance, a SISF has lower energy than that of an APB as no nearest neighbour violations are created [39]. In practice, a wide range of fault structures have been observed *during creep*, for instance dislocation ribbons [46], microtwins [3] and superlattice intrinsic [47] or extrinsic [45,48] faults, either isolated in the precipitates [45] or extending into the matrix [48]. Mechanisms for the formation of such faults commonly require short range diffusion subsequent to the passage of a dislocation to reorder into a low energy fault plane in γ′ [3,40]. Similar changes in deformation mechanism have been reported in the context of serrated flow in superalloys within the temperature range of the plastic instability [49–51].

## 2. The Portevin-Le Chatelier Effect

Serrated or jerky flow refers to a collection of plastic instabilities arising during mechanical testing, manifesting as non-monotonic stress–strain behaviour and accompanied by the localisation of strain [52,53]. In constant strain rate tensile tests, this plastic instability manifests as repeated load drops on the stress–strain curve, named the Portevin-Le Chatelier (PLC) effect after attribution of the first systematic observation of this effect [54] to Le Chatelier in steels [55] and Portevin and Le Chatelier in Al-Cu alloys [56]. Related observations were made much earlier of sudden bursts of extension during stepped loading with fixed weights in brass and steel [57,58], hence sometimes plastic instabilities during load control are referred to as the Savart-Mason effect [59]. However, most literature discussed subsequently opts to test in displacement control. Fig. 4 shows the stress–strain behaviour typical in a Fe-C ferritic mild steel deformed at different temperatures. Within an intermediate range of temperatures, the flow curve is not smooth, but rather shows an initial upper and lower yield point and subsequent load drops. This behaviour has classically been understood to arise due to

**Table 1**

Approximate temperature ranges for serrated flow in selected alloys at a strain rate of $10^{-3}$ s$^{-1}$, both absolute and normalised by the melting point $T_m$.

| Alloy System | Temperature | Homologous |
|---|---|---|
| | range, $T$/ °C | temperature, $T/T_m$ |
| Mild steel (Fe-0.05 wt.% C) | 100 – 300 [60,70,71] | 0.2 – 0.3 |
| Ni-0.16 wt.% C | 0 – 275 [72,73] | 0.15 – 0.3 |
| Ni-based superalloy (Inconel 718) | 200 – 600 [66,67] | 0.3 – 0.5 |
| TWIP/Hadfield steel | −25 – 300 [74,63] | 0.15 – 0.35 |
| Austenitic stainless steel (AISI 316) | 250 – 600 [64,65] | 0.3 – 0.5 |
| Al-Mg alloy (Type 5456) | −50 – 50 [61] | 0.25 – 0.35 |
| High Entropy Alloy (CoCrFeMnNi) | 300 – 600 [62] | 0.35 – 0.55 |
| Ni-21 wt.% Cr (0.05 wt.% C) | 300 – 650 [75,76] | 0.35 – 0.55 |
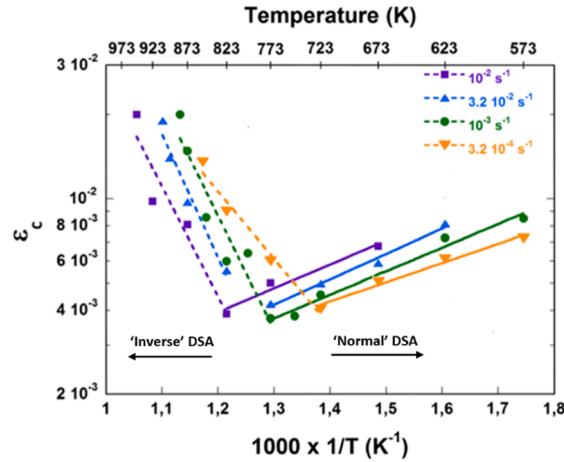


**Fig. 5.** Critical strain to onset of serrations, $\varepsilon_c$, versus temperature and strain rate in IN718 [67].

strain ageing in ferritic BCC steels, referring to a process where the extent of hardening provided by interstitial solutes becomes time dependent when deformed under conditions where solute mobility is possible (Section 3.2).

However, serrated flow is also observed in a wide range of alloys besides ferritic steels, such as substitutional Al alloys [61], High Entropy Alloys (HEAs) [62], TWIP steels [63], austenitic stainless steels [64,65] and nickel-based superalloys [66,67]. While it is widely considered likely that DSA generalises to these other alloy systems [19,23], this is largely unsubstantiated and there exist particular cases where alternate mechanisms, often termed Pseudo-PLC effects if related to solute diffusion (Section 3.3), may account for serrations. For instance, serrations are sometimes observed in metals deformed at cryogenic temperatures [68], even when high purity [69], rendering a long range solute diffusion model implausible in this case. These are often attributed to a thermomechanical instability (Section 3.3.5). The present review is mainly concerned with intermediate temperature plastic instabilities observed in several FCC alloys. Before discussing possible microscopic origins in detail, the following section gives an overview of empirical features of the serrated flow behaviour in these systems.

## 2.1. Temperature/strain rate/strain range of occurrence

While the domain varies for different compositions and microstructures, Table 1 defines approximate temperature ranges where serrated flow is observed in various alloys.

Serrated flow in substitutional FCC alloys is commonly found to begin only after a certain plastic strain, $\varepsilon_c$, is reached, termed the critical strain. Empirically, two different trends of the critical strain are observed with respect to temperature and strain rate. At low temperatures/high strain rates a regime is observed with a relationship of the form

$$\varepsilon_c^{m+\beta} \propto \dot{\varepsilon} e^{\frac{Q}{kT}}, \tag{1}$$

where $m + \beta$ and $Q$ are positive fitting constants. Hence the critical strain increases with strain rate or decreasing temperature, and is commonly termed 'normal' DSA as this follows predictions of DSA models (Section 3.2). Conversely at higher temperatures, the critical strain *empirically* follows the same equation, but $Q$ is a positive and $m + \beta$ a negative fitting constant. This is termed 'inverse' DSA and the critical strain increases with temperature or decreasing strain rate, as shown in Fig. 5. Such a trend has been observed widely in superalloys [67,77,9,78–82], Al alloys [61,83–85], austenitic stainless [86] and TWIP steels [87]. The temperature range over which
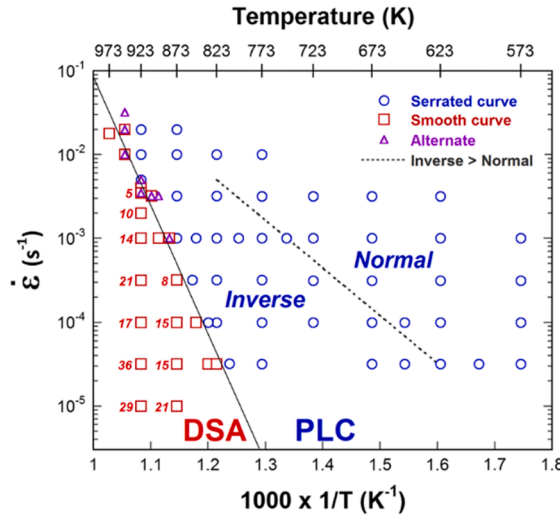
**Fig. 6.** Temperature/strain rate map for the occurrence of serrations in superalloy IN718. Regimes where the critical strain shows 'normal' DSA or 'inverse' DSA behaviour are highlighted [67].
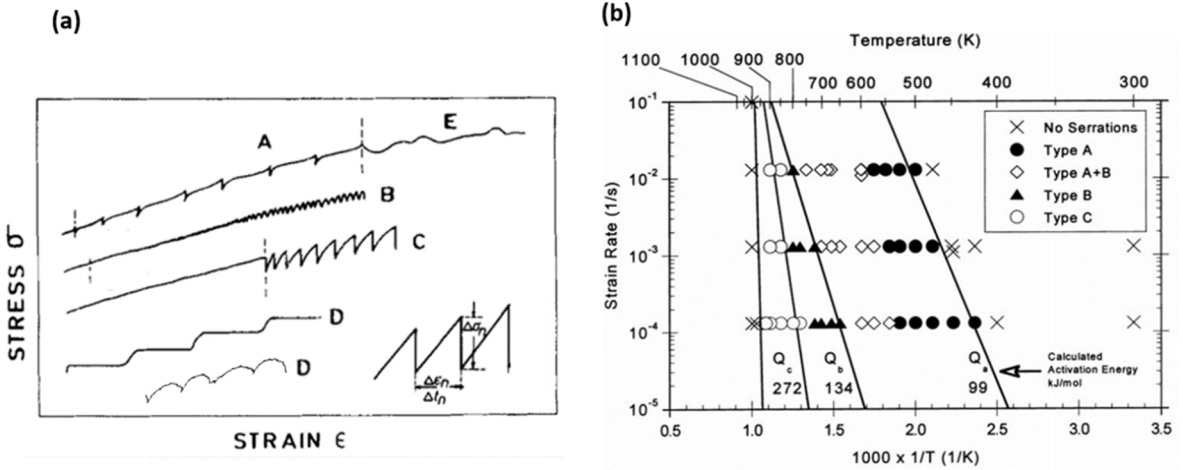


**Fig. 7.** (a) Serration Types A, B, C, D and E observed when serrated yielding operates. Adapted from [53] to include schematic of 'rounded' stress serrations (bottom curve) [100], also commonly referred to as Type D. The serration amplitude, $\Delta\sigma$, and interval between serrations, $\Delta\varepsilon$ in strain or $\Delta t$ in time, are defined. (b) Temperature and strain rate domains where different serration Types are observed in IN718 [66].

different regimes of serrations occur is a function of strain rate (Fig. 6), with the boundaries delimiting 'normal' DSA, 'inverse' DSA and smooth flow each typically fitted to an Arrhenius type law of the form

$$\dot{\varepsilon} = \dot{\varepsilon}_0 e^{-\frac{Q}{kT}}, \tag{2}$$

where $\dot{\varepsilon}$ and $T$ denote a combination of strain rates and temperatures which lay on the stability boundary, $\dot{\varepsilon}_0$ and $Q$ are positive fitting constants and $k$ is the Boltzmann constant [88]. In superalloys, some note only 'normal' [89,80,90–92], only 'inverse' [93–95] DSA behaviour or no trend in the critical strain at all [88,96,22], though in most cases it is not clear if this is a genuine discrepancy or a consequence of the chosen test matrix. A different trend was noted in Nimonic PE16, where the critical strain followed a 'normal' and 'inverse' trend with temperature, but a 'normal' trend only with strain rate [97]. Care must be taken as in some cases the critical strain reported is the total strain to onset of serrations, which may be dominated by the elastic strain to yielding[80,97,98], whereas most report the critical plastic strain [67].

In contrast, an upper and lower yield point are typically observed immediately on yielding in mild steel (Fig. 4), thus there is no clear critical strain, though in some cases a critical onset strain has been reported at the higher temperatures of serrated flow, where no initial yield point was observed, which showed an 'inverse' trend [71].
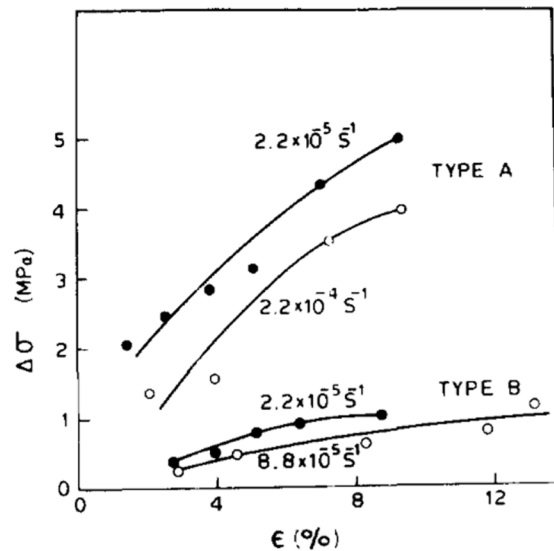
**Fig. 8.** Change in mean serration amplitude with strain and strain rate in an Al-Mn alloy, loaded under tension at room temperature, considering Type A serrations and Type B serrations individually [113].

### 2.2. Classification of serrations

Fig. 7(a) shows schematics of the typical appearance of serrations in displacement control in various engineering alloys [53], with nickel-based superalloys showing similar behaviour [23]. Comparing to the case in mild steel, an initial yield point and Lüders extension are rarely observed in as processed conditions. The appearance of serrations on the stress–strain curve is typically classified into five Types, as shown in Fig. 7(a), with different appearances being typical for different combinations of temperature/strain rate (Fig. 7(b)) [99,53]. Type A serrations are observed at the lowest temperatures/highest strain rates and are characterised by an initial rise above the baseline of the stress–strain curve, followed by a drop to [19] or below [53] the baseline, with the latter case shown in Fig. 7(a). Type A serrations appear regularly spaced with comparatively low frequency, separated by regular intervals of smooth flow. Type B serrations appear at intermediate temperature/strain rate combinations and oscillate about the mean stress, but occur with a greater frequency and smaller magnitude than Type A. Type A and B serrations may coexist. At the higher temperatures/lower strain rates, Type C serrations occur, characterised by sharp drops below the baseline stress [66]. Similar behaviour has been reported in mild steel [71]. Some further differentiate Type C serrations into Types $C_A$ and $C_B$, where the former are separated by regions of smooth flow like Type A whereas the latter are high frequency like Type B [101,102]: thus, those shown in Fig. 7(a) are of Type $C_B$.

Two further Types, D and E, have been classified. There are some discrepancies around the Type D categorisation, as shown in Fig. 7 (a), in some cases referring to step-like serrations [53], of which the factors leading to such behaviour are discussed in Section 5.2. However, others consider Type D behaviour to represent more rounded serrations [103–105], commonly linked to changes in the spatiotemporal deformation behaviour (Section 2.4). Conversely, the classification scheme of Schwink and Nortmann [100] instead refers to these as Type A2 serrations, a convention adopted here, reflecting the fact that either Type A or Type A2 serrations tend to occur in similar domains [100,104], possibly sensitive to the geometry or stress distribution [103]. Type E has a more random appearance and typically succeeds Type A serrations at high strain, when there is little work hardening.

While the qualitative classification scheme discussed above can be subjective and ambiguous in cases, identifying the serration Type enables the prediction of a number of other characteristics of the serrated flow behaviour, based on widespread empirical trends. Type C serrations often coincide with the 'inverse' DSA regime, whereas serrations Types A and B are seen when 'normal' DSA operates [77,78,97,106–110], and different Types may also be linked to changes in the statistics of the stress drop amplitudes (Section 2.3) and accompanying strain localisation (Section 2.4).

### 2.3. Serration amplitudes

The serration amplitude and frequency were defined in Fig. 7(a). The mean serration amplitude has been found to increase with strain, temperature and decreasing strain rate in tin-bronze for Type A serrations [111], Al alloys for Types A [112–114,101] and B [113,101,115,116,84] serrations and for Type B serrations in Ni-based superalloy IN625 [117]. In some cases, such a trend appears to hold right up until the disappearance of serrations [118,22] whereas in other cases, a maximum in the mean serration amplitude with temperature has been reported [77,9,96]. Note, however, that the serration amplitude also depends on the serration Type: smaller Type B serrations appear at higher temperatures/ lower strain rates than Type A, as shown in Fig. 8 [113]. Furthermore, the amplitude of any individual serration appears stochastic in nature. Inferring details of the statistical distribution is challenging, since the microstructure of a sample evolves over a mechanical test, thus the nature of the underlying distribution may evolve. For instance, as
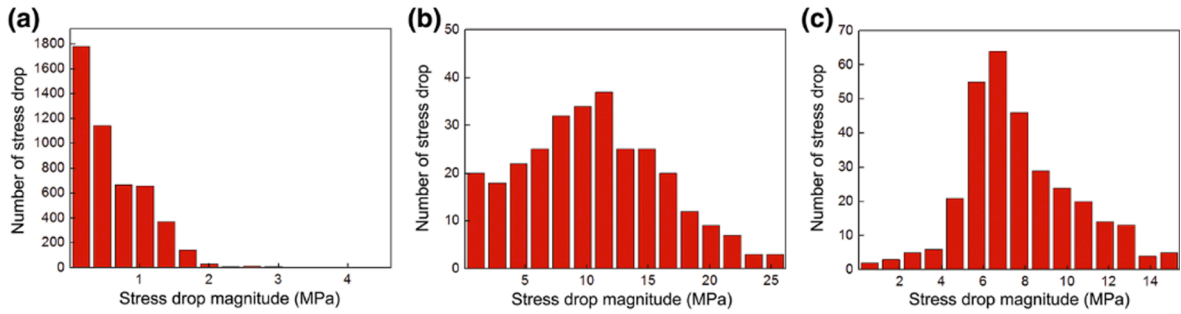
**Fig. 9.** Histogram of observed amplitude for serrations of Types (a) A, (b) B and (c) C in superalloy Nimonic 263, deformed at $4 \times 10^{-4}$ s$^{-1}$ and (a) 200 °C (b) 500 °C and (c) 760 °C, respectively [77].
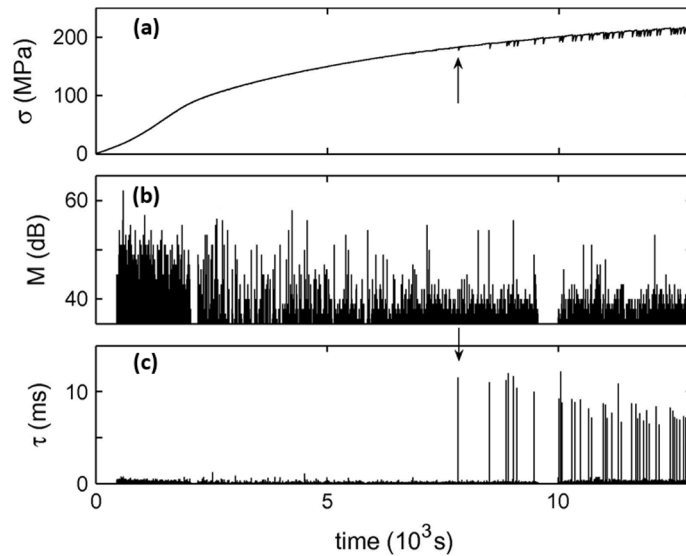


**Fig. 10.** a) Stress–time subplot for an Al-3 Mg binary alloy deformed at room temperature and $2 \times 10^{-5}$ s$^{-1}$, showing Type C serrations. An arrow indicates the critical strain. b) Logarithmic amplitude, M, of individualised AE events detected in the same interval. c) Duration of AE events detected in the same interval. The spikes in AE event duration accompanying serrated flow were interpreted as multiple overlapping deformation events [139].

noted above, the mean serration amplitude appears to increase with strain. It is commonly assumed that the distribution of serration amplitudes, when normalised by the strain-dependent mean amplitude, does not evolve with strain [119], though without clear justification. Under such assumptions, the amplitude of each serration Type appears to follow distinct statistical distributions, as shown in Fig. 9 [77]. Serration Types B and C in superalloys follow a peak or double peak shaped distribution of stresses about a mean, whereas Type A serrations showed an asymmetric distribution in Al-Mg and superalloys [120–122,80,123,14,50,124], with the frequency of a given amplitude versus amplitude fitted well by a power law [125,124]. As discussed in a recent review article [19], It has been suggested that the power law statistics of Type A serrations resemble the dynamics of Self-Organised Criticality (SOC) [126–129], referring to the possibility for catastrophes of any size in driven systems with individual components each close to the point of failure, as initially applied to model avalanche sizes in toppling sand piles [130]. Some recent papers assert that serrations are not stochastic in nature during Type B serrated flow, but rather the apparent randomness stems from a low dimensional deterministic chaos [131–133,127,128]. Up to six degrees of freedom were found sufficient to describe the evolution of stress in time, as determined by analysis of the correlation of stress in time [131,132,128]. It is widely noted that serrations, particularly of Type C, are accompanied by an audible 'click' e.g. [66]. Acoustic Emission (AE) offers an alternate technique to probe the magnitude of strain burst events, discussed in the context of serrated flow in a recent review in more detail [19], with the amplitude of AE events related to the energy dissipated in plastic deformation [134,19]. Typical results are presented in Fig. 10. It has been demonstrated that intermittent AE amplitude bursts are observed during smooth sections of the stress strain curve, displaying approximate power law distributions of amplitudes [135,136]. These bursts are widely accepted to reflect the intermittent nature of dislocation avalanche activation on the mesoscale [137,138,19], indicative of the ability of AE to detect mesoscale/microsecond time scale events which are smoothed out in the macroscopic stress strain behaviour.

During load drop events, it was observed that individual AE events did not show substantially different character, with the
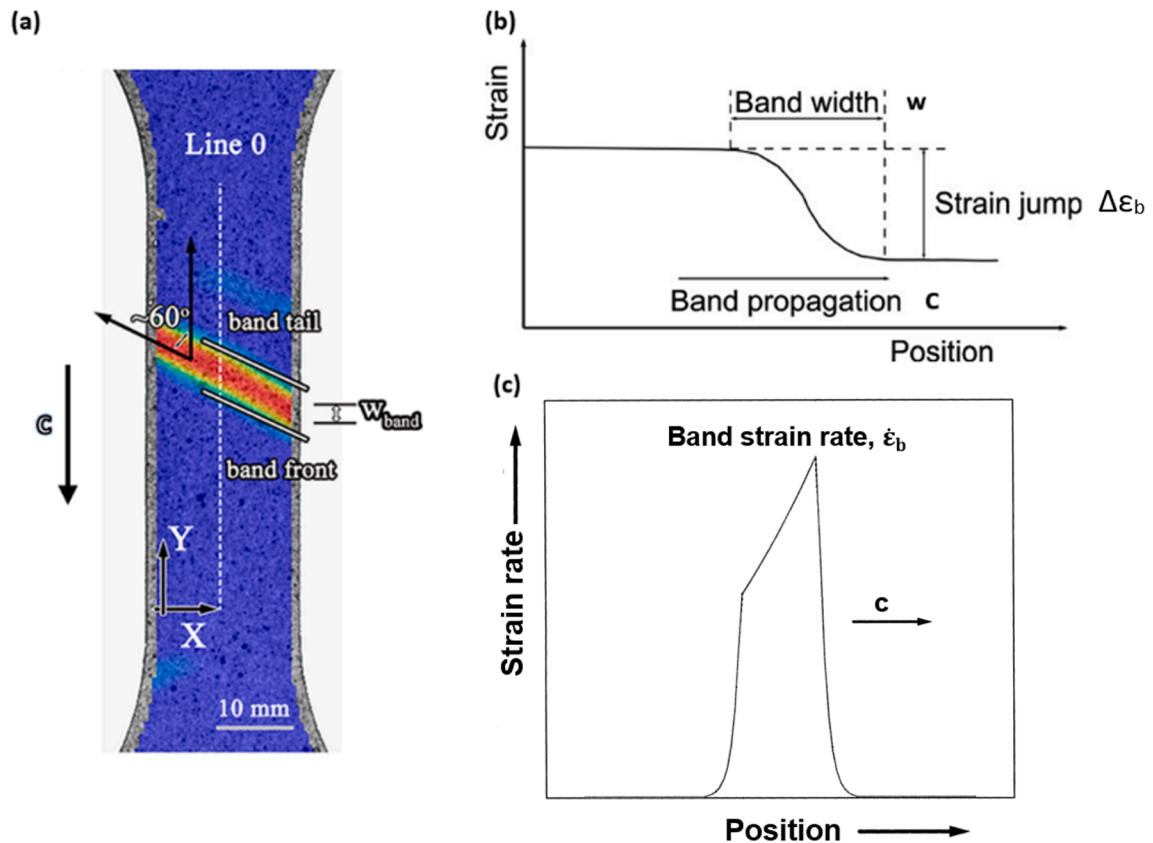
**Fig. 11.** (a) DIC reconstruction of a localised deformation band in Al alloy 5456 deformed at room temperature and $9 \times 10^{-4}$ s$^{-1}$. The band width, $w$, and band velocity, $c$, are labelled [152]. The normal strain in the y-direction is represented by a heat map, with red indicating higher strains than blue. (b) Schematic strain distribution along the gauge length for a continuously propagating deformation band [153]. The strain increment, $\Delta\varepsilon_b$, is labelled. The total plastic deformation accumulated in a time interval $dt$ is $\Delta\varepsilon_b c dt$. (c) Schematic strain rate distribution along the gauge length for a continuously propagating deformation band [154]. The band strain rate, $\dot\varepsilon_b$, is labelled.

statistical distributions showing comparable amplitudes to the smooth deformation case (Fig. 10)) and resembling the statistics of SOC in both cases [139,135,140]. This apparent inconsistency between the distribution of AE amplitudes and serration amplitudes was resolved by noting that serrations are accompanied by a time period of the order 1–10 ms with a raised frequency of activation of discrete AE events [139], as shown in Fig. 10)) and particularly prevalent for Type C serrations [139,136]. Thus, the occurrence of macroscopic load drops can be related to the linked activation of multiple slip events within a short space of time, referred to as synchronisation [139] and discussed further in Section 3.2.3.

### 2.4. Localised flow

Experimentally, serrations are accompanied by the formation of macroscopic localised bands of deformation, as shown in Fig. 11 for an Al alloy. Localised bands tend to form inclined at an angle of roughly 60° to the tensile axis [141] for flat specimens, resembling Lüders bands in mild steel [142].

Strain localisation during serrated flow has been studied through various means such as extensometry [112,143,141], direct observation of surface roughening [118], interferometric techniques [144,145], Digital Image Correlation (DIC) [146] and Infrared (IR) thermographic imaging [147–149]. A recent review discusses in detail several more specialised techniques used to image strain localisation in serrated flow[52]. These studies have largely focused on localised strain in aluminium alloys such as Al-Mg [118,150,151], likely due to the relative experimental ease of in situ measurements at room temperature, where serrations are present in this system (Table 1). Early studies indirectly observed the propagation of what were assumed to be localised deformation bands in an aluminium alloy by attaching two extensometers, one at either end of the gauge length. The local strain rate recorded by each extensometer would increase when the band passed between that extensometer's arms, allowing an estimate of the band's location at different points in time, and hence its propagation velocity [141].

Full surface displacement mapping techniques such as DIC allow more direct observation of strain localisation. In Al-Mg at room temperature, direct observation of strain localisation into bands was found through surface roughening [118]. The spatiotemporal behaviour of the bands was found to depend on the serration Type, following the classification scheme of Section 2.2 (Fig. 12). Type A
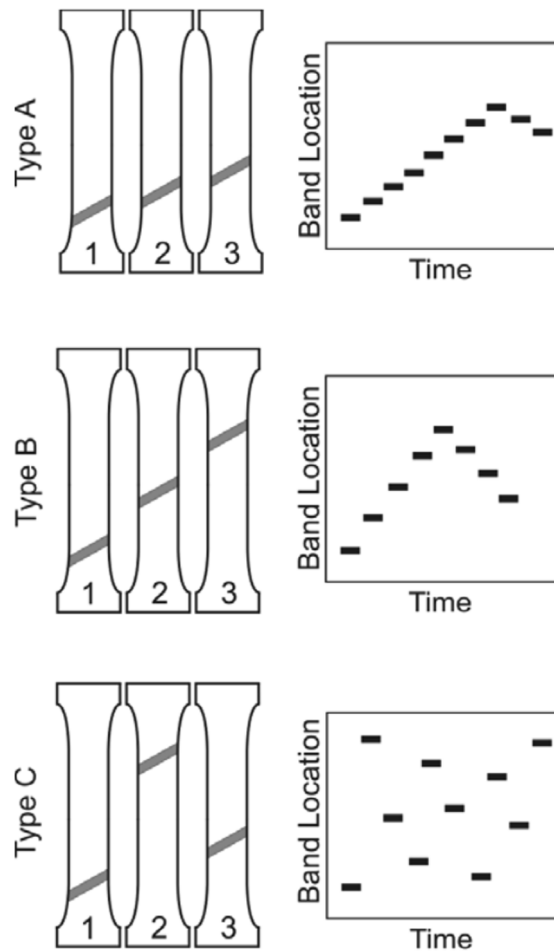
**Fig. 12.** Correlation diagrams showing schematic band position along gauge length, *y*, versus time, *t*, for serration Types A, B and C [151].

serrations accompanied the initiation of a continuously propagating band, such that a new band initiated when the prior had traversed the gauge length. Initial band nucleation is often found to take place at the ends of the sample, likely owing to any stress concentration. Type B serrations were associated with the nucleation of non-propagating [155] bands at successive positions along the gauge length and Type C serrations were associated with non-propagating bands, which nucleated at random positions on the gauge length. Type A2 serrations are commonly found to have similar behaviour to Type A, but the band would reflect upon traversing the gauge length rather than a new band nucleating [141,156,103]. While the above observations widely hold for conventional DIC performed at frame rates on the order 10 Hz, the use of high-speed cameras (1000 + Hz) for correlation has offered new insights into the spatiotemporal behaviours of bands. Type A bands have been shown to propagate in a 'hopping' manner resembling Type B behaviour, distinguished by the jump distance being a fraction of the band width and thus giving the appearance of continuous propagation on coarser time scales [157]. Further, the development of individual Type B bands has been captured, with most strain developing over a timescale of a few milliseconds [155].

In some cases, different band propagation patterns have been observed during Type C (more particularly, the less common Type $C_A$) behaviour [158], shown in Fig. 13. Weak propagating bands resembling Type A behaviour were observed in the smooth regions of deformation separating load drops, with stronger non-propagating localised bands nucleating upon load drops. Unlike the conventional Type C band spatiotemporal behaviour, the location of the non-propagating bands was non-random, but rather occurred at the location of the weak propagating band. Similar weak propagating bands have been observed, without stronger non-propagating bands nucleating, in alloys exhibiting largely smooth flow [158]. To date, these observations appear limited to some precipitate hardened [158] or grain refined [158] alloy systems, for which possible influences are discussed in Section 5.3. While bands appear at an inclination of roughly 60° at any instant, they are commonly observed to swap between two symmetrical orientations during propagation [158–160], taking on a 'cross-like' appearance when bands of both orientations are captured, as shown in Fig. 14(a). Band swapping is commonly explained since, unusually for a polycrystalline material, the occurrence of a localised band leads to a relative lateral displacement of the ends of a sample (Fig. 14(b)) [157], which needs compensating for to keep the sample aligned with the tensile axis [158]. How the band propagation characteristics evolve with differing experimental conditions has been subject to less investigation. Four quantities are typically defined, as in Fig. 11. The strain increment, $\Delta\varepsilon_b$, refers to the strain accumulated at a point
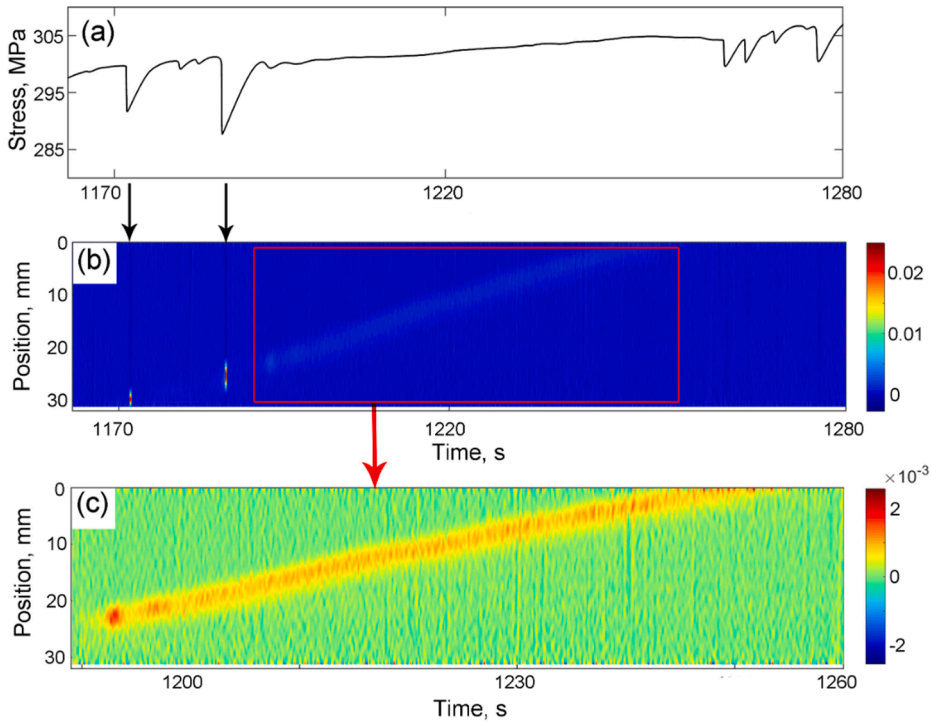
**Fig. 13.** a) Stress–time subplot for a commercial precipitate strengthened Al-Mg alloy tested at room temperature and $1.43 \times 10^{-4}$ s$^{-1}$. b) Corresponding DIC series plotting strain at a position along a line, parallel to the tensile axis and through the centre of the specimen, versus time. c) Enlarged view of DIC section during 'smooth' flow [158].
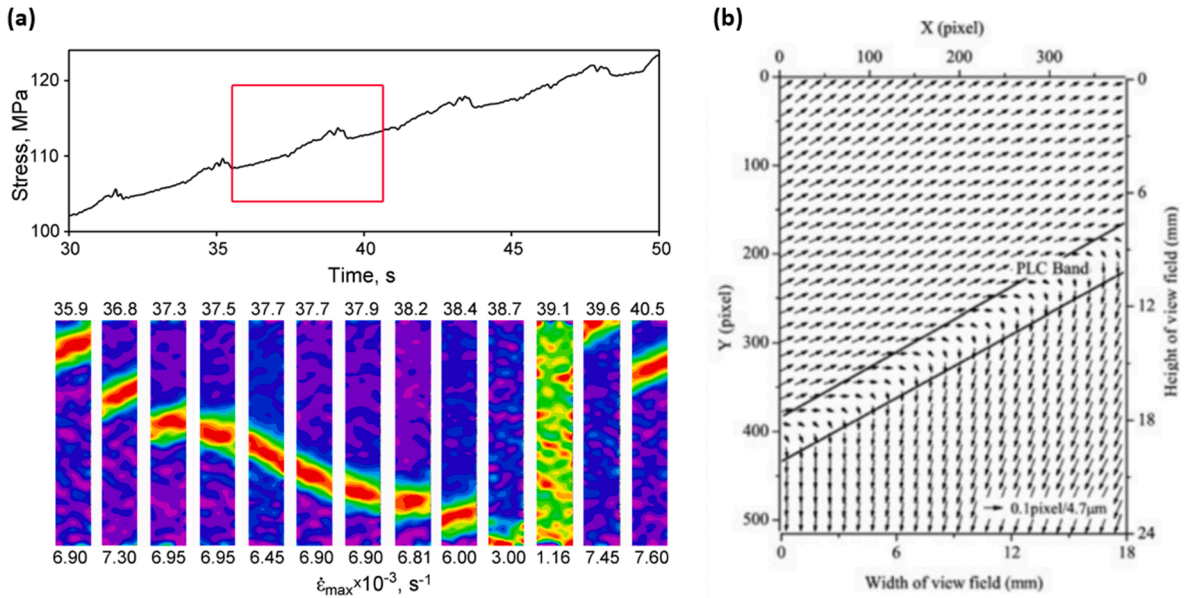


**Fig. 14.** (a) DIC image series showing propagation of a Type A localised band in a binary Al-3 Mg alloy tested at room temperature and $10^{-3}$ s$^{-1}$ [158], showing changes in band orientation during propagation. (b) Displacement vector map associated with a localised band in Al-Cu alloy A2017 deformed at room temperature, obtained through correlation of light speckle patterns [157].

in the specimen after the passage of a band, such that at any time the average strain rate in the band is $\dot{\varepsilon}_b$. During Type A serrations, where the band propagation is believed smooth, if it is assumed that all strain occurs within the band, then

$$\dot{g} = \dot{\varepsilon}_b w = c\Delta\varepsilon_b, \tag{3}$$

**Table 2**

Effects of temperature, strain rate and strain on band propagation behaviour.

| Parameter | Increase crosshead velocity | Increase temperature | Increase strain |
|---|---|---|---|
| $\Delta\varepsilon_b$ | No effect [143,141,161,149] Small increase [162–166] | Decreases [164,163,166] Increases [167] | Increases [143,141,161,162,147,148,168,149,169,24,170,166] |
| $c$ | Increases [166,169,161,141,163,144,118,145,162,146,171,164,172,148,149,165] | Increases [164] Decreases [167] | Decreases [158,166,170,173,146,141,144,145,161,167,162,171,172,147–149,169,24,174,159] |
| $w$ | Decreases [118,148] Increases [166,141,145] Small Increase [143,163–165] No effect [144,148,161] | Decreases [163] | Increases [145,161,146] Decreases [166,143,141,159] |
| $\dot{\varepsilon}_b$ | Increases [161,171,166] | Increases [166] | Increases [158,171,166] |
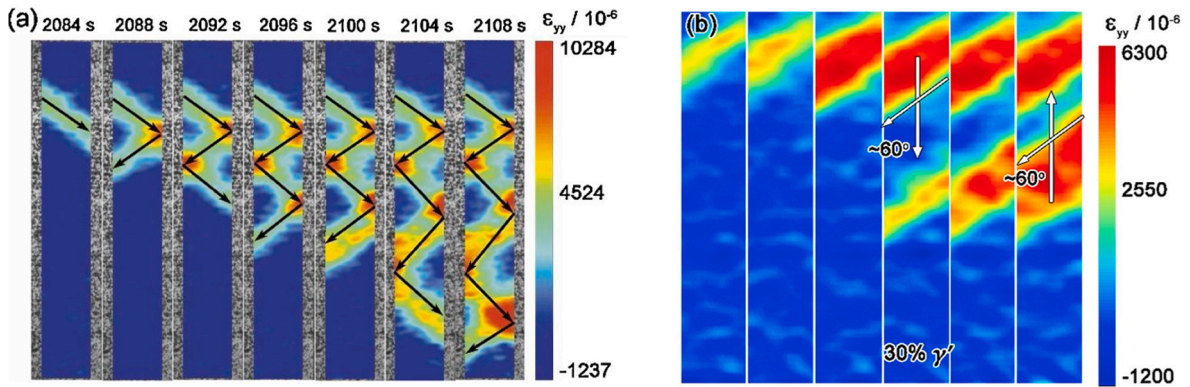
**Fig. 15.** Map of the normal strain along the tensile direction, $\varepsilon_{yy}$, determined through DIC for an experimental Ni-Co superalloy deformed at 500 °C and $10^{-4}$ s$^{-1}$. Adjacent maps (left to right) mark the evolution of time, taken at 4 s intervals. Total sample dimensions were $25 \times 5$ mm$^2$. Maps were taken at strains (a) close to the failure strain of 0.25 [186] (b) of 0.15 [184]. Hopping (Type B) bands appear in (b), whereas the zigzag propagation in (a) has not been observed elsewhere.

where $\dot{g}$ denotes the crosshead velocity, as shown in Figs. 11(b) and (c) [143,141]. Hence the four quantities are linked, such that the product of such pairings should equal the crosshead velocity. Table 2 summarises their variation with strain, strain rate and temperature from several investigations.

The greatest empirical agreement appears to be that the band velocity increases with strain rate and decreases with strain while the strain increment increases with strain. These observations are predominantly made for Type A propagation. As each Type A serration corresponds to the initiation of one localised band which propagates through the sample [143], the band spatiotemporal evolution is manifested on the stress–strain curve. Type A serrations are commonly considered quasi periodic [112,143,111] with the strain and time intervals between serrations increasing with strain in Al-Mg [112,175,176] and Udimet 720 LI [9], consistent with the trends in band propagation characteristics in Table 2.

There is comparatively little experimental evidence describing the band propagation characteristics of Type B/C serrations, though in some cases the trends in Table 2 appear to extend to Type B serrations when considering the average propagation [166,177,146,159]: Type C serrations are typically considered non-propagating thus the band velocity is zero. Each Type B/C serration can be correlated with the initiation of a non propagating band [178,177,155,146], with the jump distance between band initiation events decreasing with strain [177,143,146], though in different cases the time/strain interval between band jumps has been found to increase [143] or decrease [177] with strain.

It is generally believed that these observations apply in all substitutional alloys showing serrations, for instance in superalloys [89,9,106,179,109,180,181]. However, direct evidence for the strain localisation behaviour in superalloys has been subject to limited study [182–186]. Propagating bands were observed at 60° to the tensile axis during deformation of Hastelloy X at elevated temperatures through DIC, though the limited field of view achieved made determination of the spatiotemporal characteristics difficult [182,183]. Propagating localised deformation bands were found in an Inconel alloy induced by raising the temperature under dead weight loading, though the different machine control conditions make comparison to the results above in displacement control challenging [185]. Continuously propagating bands and hopping bands were observed under different conditions in a Ni-Co base superalloy via DIC [184], though a recent study on the same material with the same conditions found a strain localisation pattern unlike that previously reported in superalloys, where localised bands propagated in a 'zigzag' pattern, shown in Fig. 15 [186]. While most analysis limits itself to the evolution of mean band propagation characteristics, it was suggested that spatially resolved strain rate fluctuations can be detected through optical extensometry during the smooth propagation between Type A serrations [187,188]. These fluctuations followed statistics resembling those of SOC (Section 2.4) and were taken to be indicators of the underlying intermittency of deformation [187,188]. However, the authors note that similar fluctuations are observed even if the elastic region and their magnitude implies the need for substantially sub-pixel accuracy to detect, thus this claim may raise questions without a clear analysis of the noise floor.

These observations are usually made on flat specimens: band propagation is harder to detect visually in cuboidal or cylindrical specimens and it has been suggested that the bands in a cylindrical specimen are conical [141], supported by Finite Element (FE) simulations [103,124] performed using methods discussed in Section 3.2.3. While monotonic tension is overwhelmingly the most common loading geometry, DIC performed on flat specimens under shear loading has demonstrated similar band propagation [189–191]. The directions of the band orientation/velocity broadly matched expectations from tensile tests, when considering frames of reference with the principle in-plane axes aligned, though it was noted that band initiation was influenced by the different stress state near free ends of the sample, and the band orientation was observed to change with strain [189–191].

Efforts to investigate biaxial stress states have been performed through sheet punching or bulging [192–194], using a cruciform specimen [195–197], or tensile tests on notched bars [182,198]. In the latter case, band immobilisation in the notched region may be expected [158]. Analysis of the spatiotemporal nature of strain localisation under model biaxial tension conditions is largely limited by the non-ideal stress states achieved experimentally, resembling equibiaxial tension for a subsection of the deforming region only
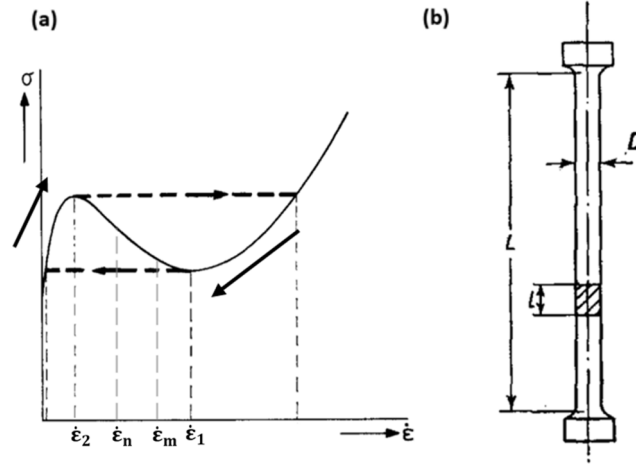
**Fig. 16.** (a) Stress–strain rate plots showing negative SRS in an intermediate strain rate range. A lower force is required to locally deform the specimen at $\dot{\varepsilon}_m = \frac{L}{l}\dot{\varepsilon}_n$ than uniformly at $\dot{\varepsilon}_n$, thus uniform solutions are unstable in the negative strain rate exponent branch. Arrows indicate the time evolution of the local strain rate for a mean strain rate between $\dot{\varepsilon}_1$ and $\dot{\varepsilon}_2$. Upon reaching either extrema, a sudden jump in strain rate occurs [10]. (b) Tensile test sample with gauge length $L$. Deformation is localised within a length $l$ during serrated yielding [14].

[193,199]. Thus, the spatiotemporal patterns observed appear to predominantly reflect the spatial symmetry of the stress state, or local orientation of the major strain axis, outside of the biaxial region. For instance, in the case of die punching of a sheet, concentric patterns of localised deformation were observed outside of the equibiaxial region near the punch centre [192–194], consistent with FE simulations [192]. However, the strain localisation appears less prevalent in a number of geometries in the equibiaxial region, where there is no in-plane shear strain [192,196], or to initiate outside the equibiaxial region [197,193], accompanied by a suppression of the global onset of serrated flow [193,195,196].

To summarise, three different band propagation characteristics are common: continuously propagating, discontinuously propagating or non-propagating [118]. While it is rare to investigate the strain localisation through DIC across as wide range of strain rates, temperatures and strains as the serration characteristics in a tensile test, it is widely believed that these three propagation characteristics correspond to serration Types A, B and C, respectively [53]. Thus, the band propagation characteristics may be predicted from the deformation conditions based on the observed serration Type (Fig. 7(b)).

## 3. Theories for serrated flow

### 3.1. Plastic instabilities

Plastic instabilities such as the PLC effect may develop in cases where there is a drive for strain to localise within the sample. A classical example of this is the onset of necking, where geometrical softening due to a local reduction in area outweighs any local strain hardening [200]. To understand the origins in the case of serrated flow, consider a body initially subject to a uniform stress, $\sigma$, strain, $\varepsilon$, and strain rate, $\dot{\varepsilon}$, with a constitutive relation of the form [201–203]

$$\delta\sigma = h\delta\varepsilon + S\delta(\ln\dot{\varepsilon}), \tag{4}$$

where $h = \left(\frac{\partial\sigma}{\partial\varepsilon}\right)_{\dot{\varepsilon}}$ represents the work hardening index and $S = \left(\frac{\partial\sigma}{\partial\ln\dot{\varepsilon}}\right)_{\varepsilon}$ closely relates to the SRS, $n$, typically defined as $n = \left(\frac{\partial\ln\sigma}{\partial\ln\dot{\varepsilon}}\right)_{\varepsilon}$. Important to serrated flow is that $S$ and $n$ both have the same sign for positive $\sigma$. Such a constitutive form can be justified in cases where the strengthening effects due to strain and strain rate are separable and additive. Suppose a small perturbation, $\delta\varepsilon$, develops in a cross section along the gauge length, as shown schematically in Fig. 16. Assuming we are far from necking (so can neglect the local change in area and hence stress in the perturbation, $\delta\sigma = 0$) and trialling a solution which evolves in time, $t$, as

$$\delta\varepsilon = \delta\varepsilon_0 e^{\lambda t}, \tag{5}$$

for constants $\delta\varepsilon_0$ and $\lambda$, the perturbation will grow in time if $\lambda > 0$, hence if [201–203]

$$\frac{h\dot{\varepsilon}}{S} < 0. \tag{6}$$

This distinguishes two possible types of instability. The first, 'Type S' instability, occurs when the SRS becomes negative [14,10,203,204,201]. By considering the time evolution of the solution to the machine equation,
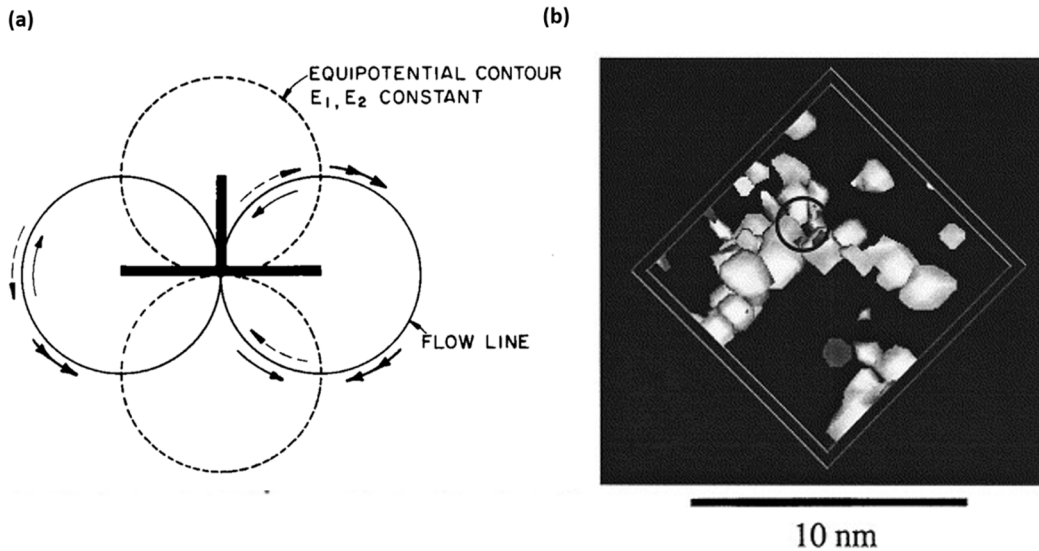
(a)

(b)



**Fig. 17.** (a) Equipotential lines and lines of flow (solid single-headed arrow: negative misfit, dashed arrow: positive misfit) for interstitial solute in the potential field of an edge dislocation centred at the origin and viewed down its line vector, showing schematic tendency for solute accumulation at the core [212]. (b) 4 at.% C isosurface around dislocation centre in Fe-0.85 at.% C martensitic steel following an ageing at room temperature for 24 h [211]. The apparent threefold symmetry around the core was suggested to relate to the theoretical symmetry of the concentration distribution around a <111> screw dislocation aligned with the triad axis of a cube [213].

$$\frac{\dot{g}}{L} = \frac{\dot{\sigma}}{M} + \frac{1}{L}\int_L \dot{\varepsilon}dx, \tag{7}$$

where $M$ is the combined machine and specimen stiffness, $\dot{g}$ denotes the crosshead velocity and the last term represents the plastic strain rate $\dot{\varepsilon}(x)$ averaged over the gauge length $L$, it was shown that homogenous solutions with an average strain rate in the region of negative SRS were unstable [10,205]. Rather, the instantaneous strain rate would approach the imposed strain rate, but jump upon reaching one of the extrema (Fig. 16(a)), leading to relaxation oscillation patterns on the stress–strain curve.

In practice, such relaxation oscillations with a spatially uniform strain rate[1] are not observed (Section 2.4). Rather, under so-called strain rate softening conditions, a lower stress is required to deform a length $l$ of specimen locally at a strain rate $\dot{\varepsilon}_m = \frac{L}{l}\dot{\varepsilon}_n$ than to deform the gauge length, $L$, uniformly at a rate $\dot{\varepsilon}_n$ (Fig. 16). Hence most deformation will be localised in so-called Lüders or PLC bands, which cannot persist indefinitely at the same location. Further local slip is resisted by a combination of unloading (Types B and C) [19], since bursts of plastic strain associated with the PLC band can exceed the imposed strain rate (Eq. (7)); local work hardening and incompatibility stresses, with the latter two effects favouring subsequent localisation of deformation elsewhere in the sample [14,201].

Most cases of obstacle inhibited glide show a positive SRS, since higher strain rates imply a reduced probability of thermally overcoming obstacles [206]. However, during an intermediate range of strain rates, a negative rate sensitivity is almost universally found to accompany serrated flow in substitutional FCC alloys (Section 4.1). While classically DSA (Section 3.2) has been employed to account for serrated flow and a negative SRS in mild steel, this provides a criterion to understand other possible mechanisms for serrated flow, often termed Pseudo-PLC effects (Section 3.3).

Conversely, strain softening 'Type h' instabilities occur when the work hardening becomes negative and are usually associated with upper and lower yield points or necking. Yield point phenomena are sometimes observed in highly perfect crystals due to initial rapid dislocation generation [207], due to geometric softening resulting from slip plane rotation [208], or relating to alternate mechanisms for serrated yielding discussed in Section 3.3, but are most commonly associated with the breakaway of dislocations from their solute atmospheres, termed strain ageing.

### 3.2. Strain ageing

Serrated flow has historically been understood in C–containing ferritic steels through strain ageing. The basic mechanism is as follows [13,209]: over time, interstitial carbon will diffuse to dislocation cores, in order to minimise the energy of the overlapping solute and dislocation strain fields (Fig. 17(a)). This pins the dislocation in a low energy configuration, increasing the stress needed to

---

[1] The possibility of travelling wave solutions with inhomogeneous strain rate was considered [10,205], although it is not clear that a solution existed for the strain rate profile of the waveform, consistent with assumptions of stress equilibrium through the sample. Section 3.2.3 discusses improvements to the classical models.
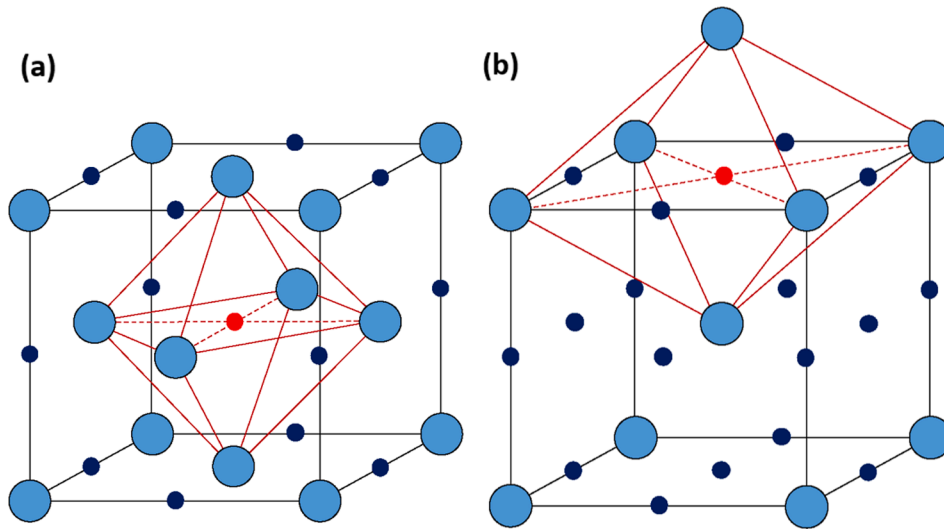
**Fig. 18.** Octahedral interstices in (a) FCC (b) BCC crystal structures [217]. The asymmetric nature of the interstice in BCC leads to shear strain interactions with dislocations.

break free from the so-called Cottrell atmosphere. Once the dislocation breaks free, it will now continue to glide at a lower stress unless arrested for sufficient time for solute to catch up. Static Strain Ageing (SSA) refers to the case where an initially worked test piece is held in the absence of an imposed strain rate at a temperature where solute diffusion is possible, leading to the development of an initial upper and lower yield point [210]. Conversely, DSA occurs at combinations of temperatures and strain rates where solute is sufficiently mobile to catch up with a dislocation while it is temporarily arrested at an obstacle during loading, but insufficiently mobile to migrate with the dislocation. Hence repeated serrations are observed as dislocations repeatedly become locked by and escape from their Cottrell atmospheres. Experimental evidence such as Atom Probe Tomography (APT) has indicated the formation of solute atmospheres in mild steel, as shown in Fig. 17(b) [211].

However, serrated flow is also observed in a wide range of alloys besides ferritic steels, including several FCC substitutional alloys (Section 2). In several cases these alloys contain nominally no carbon in solution: in the case of superalloys, for instance, carbon is believed to segregate to and strengthen the grain boundaries [25]. It is not clear whether sufficient carbon is present in solution to cause serrations in polycrystalline superalloys, and serrations have also been observed in nominally carbon-free polycrystal [214] and single crystal [215] superalloys. However, it is worth noting that the fraction of carbon required in solution for locking is small and may be present as an impurity. In Ni-C, pinning dislocations with 1 C atom for every $\sqrt{2}a$ of dislocation line, where $a$ is the lattice parameter, would require roughly 0.03 at.% C, or 0.0075 wt.% C, assuming a dislocation density of $10^{16}$ m$^{-2}$.

To quote Cottrell, *'It is attractive to suppose that the Portevin-Le Chatelier effect has a similar cause* (in substitutional alloys), *with copper, and magnesium, etc., as the active solute atoms'* [54]. However, as noted, there are some important differences. Substitutional solute diffusion is typically much slower than interstitial solute diffusion, due to the lesser number of vacant lattice sites available for atomic diffusion into: typical vacancy point defect fractions are less than $10^{-3}$ [216], whereas a 50 at.% fraction of interstitial solute would be required to fill every octahedral interstice in an FCC lattice, for instance. Hence, it is not clear that substitutional solute diffusion is sufficiently fast to allow DSA at the temperatures in Table 1.

Furthermore, carbon in ferrite sits in distorted octahedral interstices, leading to a large asymmetric strain field which interacts strongly with both edge and screw dislocations (Fig. 18) [13]. It is not clear that solutes in FCC metals will have as strong of an elastic interaction with dislocations. A counterpoint, however, is that as deformation in FCC metals is often less rate sensitive than in BCC alloys, a weaker interaction is needed for plastic instabilities through a negative SRS (Section 2.1). It is clear that a careful assessment is required to apply DSA to substitutional alloys. The first numerical efforts to describe strain ageing focused on the static case of diffusion of solute to a stationary dislocation core. By considering the drift velocity of solute in the potential field of a stationary edge dislocation (Fig. 17(a)), considering hydrostatic elastic interactions away from the dislocation core, Cottrell showed that the solute concentration $C(t)$ at the core after time $t$ takes the form

$$C(t) = KC_0 \left( \frac{Dt}{kT} \right)^{2/3},$$

(8)

where $C_0$ is the mean solute concentration, $D$ the diffusivity, $T$ the temperature and $K$ is a constant related to the strength of the elastic interactions [13]. The physical origins of the 2/3 exponent can be readily understood. Suppose all solute within a critical radius $r$ has had time to diffuse to the core. Then the total solute at the core scales as $\pi C_0 r^2$. The critical radius $r$ can be estimated by noting that the interaction energy between a solute and the dislocation core scales as $r^{-1}$, where $r$ is the distance of the solute from the dislocation core. The drift velocity $v_{drift}$ scales with the gradient of the potential, hence as $r^{-2}$. Hence the time taken for a solute at distance $r$ to reach the
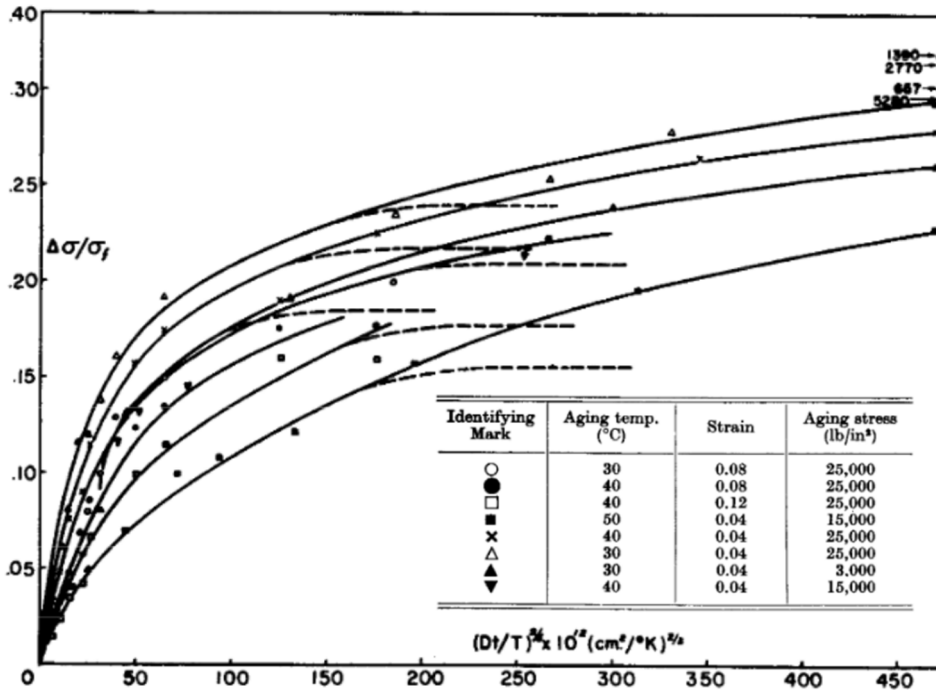
**Fig. 19.** Strain ageing kinetics of ingot iron [223]. Plot of $\frac{\Delta\sigma}{\sigma}$, the magnitude of the static strain ageing yield point normalised by the stress prior to ageing, versus $\left(\frac{Dt}{T}\right)^{\frac{2}{3}}$, for diffusivity $D$, ageing time $t$ and ageing temperature, $T$. The expected linear trend when the Cottrell-Bilby expression (Eq. (8)) holds is observed for short ageing times only.

core scales as $\frac{r}{v_{drift}} = r^3$, or in other words, the critical radius over which solute has time to reach the core scales as $t^{1/3}$ [218]. Similar expressions have been derived for the solute concentration around a screw dislocation in ferrite [219].

Cottrell notes that this expression is only strictly valid for short ageing times, since it neglects back diffusion in the resulting concentration gradient [209]. Indirect measurements of the solute removed from solution based on Internal Friction (IF) [220], resistivity measurements [221], or the yield drop magnitude [13,222,223] may indicate that the build up of solute is overestimated by Cottrell-Bilby kinetics (Eq. (8)) for long ageing times, as shown in Fig. 19. Louat [224] and Harper [220] modify Eq. (8) by noting that the concentration of solute at the dislocation core must remain finite and will saturate once it reaches an equilibrium value $C_{eq}$ [209], which, following Boltzmann statistics, is given by

$$C_{eq} = C_0 \frac{1}{1 + \mathrm{e}^{-\frac{W}{kT}}}, \tag{9}$$

where $W$ is the (positive) solute-dislocation binding energy, such

$$C(t) = C_{eq} \left( 1 - \mathrm{e}^{\frac{KC_0}{C_{eq}}\left(\frac{Dt}{kT}\right)^{2/3}} \right). \tag{10}$$

In practice, different exponents besides 2/3 have been suggested, relating to different diffusion modes such as pipe diffusion [225]. Modelling DSA presents additional challenges as both the solute and dislocations are mobile. Early work supposes that DSA will occur when the drift velocities of solute towards the dislocation core,

$$v_{drift} = -\frac{DW}{kTb}, \tag{11}$$

where $b$ is the Burger's vector, and the mean dislocation velocity,

$$v_{dislocation} = \frac{\dot{\varepsilon}}{\rho_m b}, \tag{12}$$

where $\rho_m$ is the mobile dislocation density, are comparable [226–228]. This simple model captures several experimental observations. First, assuming the dominant effect on temperature is through the diffusivity, this predicts the stability boundary will take the form

**Table 3**
Approximate values of various parameters in domain where serrated yielding occurs in mild steel and a superalloy.

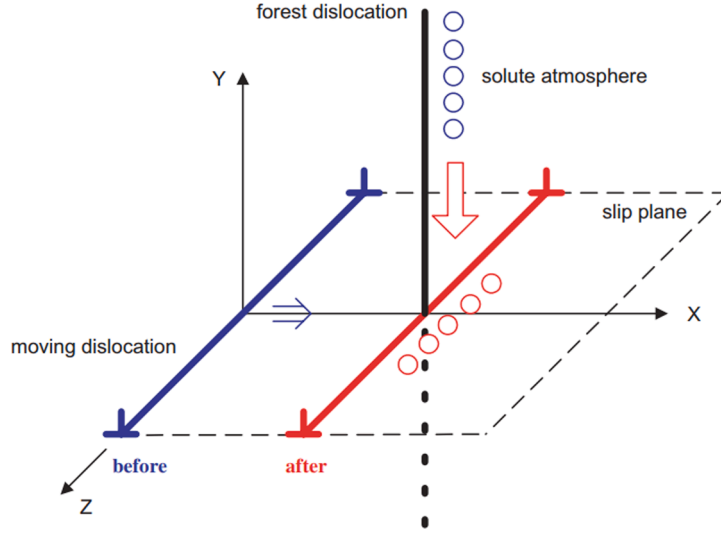| Parameter | Mild Steel | Superalloy |
|---|---|---|
| $T$, K | 350 | 600 |
| $\dot{\varepsilon}$, s$^{-1}$ | $10^{-3}$ | $10^{-3}$ |
| $\rho_m$, m$^{-2}$ | $10^{14}$ | $10^{14}$ |
| $b$, m | $2.5 \times 10^{-10}$ | $2.5 \times 10^{-10}$ |
| $\nabla V$, eV/nm | 2 [231] | 1 [89,22] |
| $D$, m$^2$/s | $10^{-18}$ (C in Fe) [54] | $10^{-18}$ (C in Ni) [232] |
| | | $10^{-25}$ (Cr in Ni) [22] |



**Fig. 20.** DSA mechanism through solute pipe diffusion. Mobile dislocations develop a solute atmosphere while locked at immobile forest dislocations, whose cores are saturated in solute prior [65].

$$\dot{\varepsilon}e^{\frac{Q}{kT}} = \text{constant},\tag{13}$$

where $Q$ is the activation energy for diffusion of the locking solute. This is often observed experimentally (Fig. 6).

Secondly, in substitutional alloys, a critical strain is typically observed such that serrations only begin on the stress strain curve once the critical strain is exceeded (Section 2.1). Here, this can be seen to arise from an increased mobile dislocation density with increasing strain, reducing the mean dislocation velocity, and an increased deformation induced vacancy concentration, increasing the diffusivity and hence drift velocity. Supposing a power law fit in each case [54,15], such

$$D = D_0 \varepsilon^m e^{-\frac{Q}{kT}}\tag{14}$$

and

$$\rho = \rho_0 \varepsilon^\beta,\tag{15}$$

for constants $D_0, \rho_0, m$ and $\beta$, this leads to a predicted critical strain of the form

$$\varepsilon_c^{m+\beta} = \dot{\varepsilon}e^{\frac{Q}{kT}}\left(\frac{-kT}{D_0 W \rho_0}\right).\tag{16}$$

Such a temperature and strain rate dependence is extensively observed at low temperatures/high strain rates in substitutional alloys when DSA operates, termed 'normal' DSA (Section 2.1). However, the model may fail quantitatively. It is not clear that solute diffusivity is sufficiently fast in substitutional alloys for DSA [89,22]. Considering typical values of the parameters in the domain where DSA operates (Table 3), one obtains a dislocation velocity of the order $4 \times 10^{-8}$ m/s and drift velocities of the order $2 \times 10^{-8}$ m/s, $2 \times 10^{-15}$ m/s and $6 \times 10^{-8}$ m/s for carbon in nickel, chromium in nickel and carbon in ferrite, respectively. Similar concerns have been raised in Al-Mg [20] and TWIP steels [21,229]. Various suggested refinements may offer explanations for the differences, for instance relating to the deformation induced enhancement of diffusivity [54,15] or through faster diffusion modes such as pipe diffusion [230],
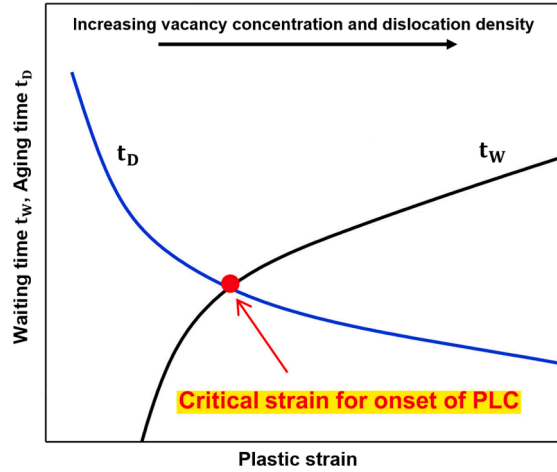
**Fig. 21.** Time required for solute diffusion to a dislocation core, $t_{D*}$, and waiting time of a dislocation at an obstacle, $t_W$, versus strain. $t_{D*}$ decreases with strain due to an enhanced vacancy concentration, while $t_W$ increases with strain due to a greater dislocation density and hence lower mean dislocation velocity. Serrated yielding begins when $t_D * < t_W$ [233].

but with few experimental investigations into the diffusivities of superalloys at the temperatures of serrated flow, it is not clear to date whether long range substitutional solute diffusion should be possible[2].

In some cases, experimentally measured activation energies, $Q$, typically based on critical strain measurements, are found to be lower than that for bulk atomic diffusion [9]. It has been suggested that pipe diffusion may be responsible for DSA, if solute is able to diffuse to static forest dislocations, then drain onto mobile dislocations while a mobile and forest dislocation temporarily intersect (Fig. 20) [14,230]. Clearly this mechanism still relies on being able to form aged forest dislocations. McCormick proposed a refinement to the condition for DSA by noting that dislocation motion occurs in discontinuous jumps: hence solute diffusion to the dislocation cores can occur during the time when a mobile dislocation is temporarily arrested at an obstacle [15]. Hence, DSA can be treated similarly to SSA, but now the ageing times are determined by the imposed strain rate rather than a heat treatment duration. If the flight time between obstacles is assumed negligible, the arrest time, $t_W$, of a dislocation at an obstacle, is given by

$$t_W = \frac{d\rho_m b}{\dot{\varepsilon}}, \tag{17}$$

where $d$ denotes the mean spacing between obstacles. DSA was proposed to occur when the arrest time exceeds a critical ageing time, $t_{D*}$, required to form a sufficient atmosphere, $C_{crit}$, given by

$$t_{D*} = \frac{kT}{D}\left(\frac{C_{crit}}{KC_0}\right)^{3/2}, \tag{18}$$

which follows from rearranging Eq. (8) for static strain ageing [15]. Combining Eqs. (17) and (18) and noting their strain dependencies (Fig. 21) leads to a critical strain of similar form to Eq. (16), but also accounts for some microstructural effects (Section 5), through the effects on obstacle spacing. Understanding the effect of formation of a Cottrell atmosphere on subsequent deformation requires an appreciation of the mechanisms by which continued plastic flow can occur. Three processes have been envisaged: the rapid generation of new solute free mobile dislocations [234,15]; the dragging of the solute atmosphere at the dislocation core [209] or the breakaway of existing dislocations from their solute atmospheres [235]. Most models consider the latter process. A major advancement in understanding serrated flow came from recognition that plastic instabilities may develop due to strain rate softening (Section 3.1). It can be shown that a consideration of the stress required to break a dislocation from its solute atmosphere may predict a negative SRS [236]. To see this, an Arrhenius strain rate law, of the form

$$\dot{\varepsilon} = \rho_m b \nu_0 e^{-\frac{H}{kT}}, \tag{19}$$

is commonly assumed, where $\nu_0$ represents an attempt frequency to overcome an activation energy barrier

$$H(t, t_D) = \frac{\partial H}{\partial \sigma}(\sigma(t) - \sigma_0) + \frac{\partial H}{\partial C}C(t_D), \tag{20}$$

---

[2] McCormick's model [15] attempts to partially explain this discrepancy through the discontinuous nature of dislocation motion, though the question perhaps remains as to why this refinement is not necessary for carbon in ferrite.
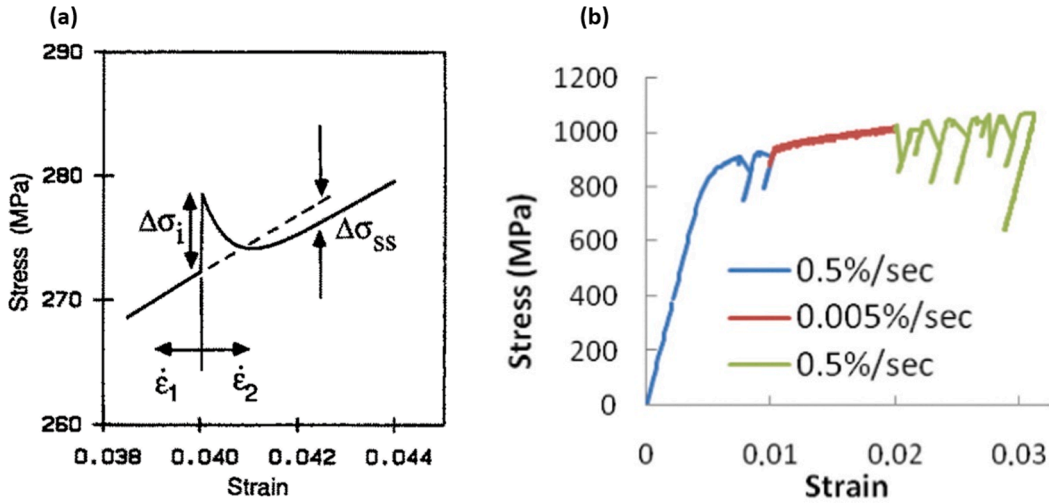
**Fig. 22.** (a) Flow stress transient on a sudden increase in strain rate to $\dot{\varepsilon}_2 > \dot{\varepsilon}_1$. The instantaneous stress response $\Delta\sigma_i$ and the steady state response $\Delta\sigma_{ss}$ are of opposite signs [17]. (b) Strain rate jump tests performed on RR1000 at 600 °C. Little change in mean stress was observed on a rate jump [250].

for constants $H_0, \sigma_0$ and $\frac{\partial H}{\partial C}$, where $V = -\frac{\partial H}{\partial \sigma}$ is the activation volume, the applied stress is a function of time, $t$, and the solute concentration is a function of the ageing time, $t_D$, since the previous dislocation unpinning event. In other words, the rate of thermally activated dislocation motion depends on the probability of overcoming an activation energy barrier which depends on both stress and the solute concentration around a dislocation core. Further, it is assumed sufficient to consider the mean solute atmosphere which forms around the dislocation cores while they are stationary at obstacles under steady state conditions [236,17]: hence Eqs. (8) and (17) can be combined to predict the mean solute concentration. Rearranging for the stress gives

$$\sigma = \sigma_0 + \frac{1}{V}\left(kT\ln\frac{\dot{\varepsilon}}{\rho_m b \nu_0} + \frac{\partial H}{\partial C}C(t_W)\right). \tag{21}$$

The first term in the brackets represents the standard positive SRS in the absence of DSA whereas the second term represents the negative SRS term arising due to the increased mean solute concentration build up at lower strain rates. Applying the condition

$$\frac{d\sigma}{d(\ln\dot{\varepsilon})} < 0 \tag{22}$$

leads to a condition for DSA of the form

$$\left(\frac{Dt_W}{kT}\right)^{2/3} > \alpha \tag{23}$$

if saturation is not assumed by combining Eqs. (8), (17) and (21) [236,16,17,237], where the various constants have been grouped into a parameter $\alpha$.

Conversely, accounting for the possibility of solute saturation leads to a condition of the form

$$\left(\frac{Dt_W}{kT}\right)^{2/3} e^{-\left(\frac{Dt_W}{kT}\right)^{2/3}} > \alpha', \tag{24}$$

obtained by combining Eqs. (10), (17) and (21) [204,237], for a different constant, $\alpha'$. A 'normal' critical strain is predicted by Eq. (23). The origins of the disappearance of serrations at slow strain rates in this model can be understood as for very slow strain rates, virtually all dislocations are saturated in solute, such that there is little change in mean solute concentration with strain rate.

This framework also predicts that DSA will have an effect on the mean stress level, through the effect on the mean solute build up around a dislocation, $C(t_W)$. In particular, DSA would lead to an increase in work hardening rate (through $D$ and $\rho_m$) and an increased gradient with respect to temperature (through $D$), as both factors raise solute mobility and hence the amount of solute build up [236].

The models discussed above, developed by McCormick [15] and van den Beukel [236], remain the most commonly used to account for features during serrated flow in superalloys, such as the occurrence of a critical strain. However, on top of concerns about whether DSA operates in superalloys, there remains significant room to develop models for DSA further. Some of the major shortfalls are discussed in turn.
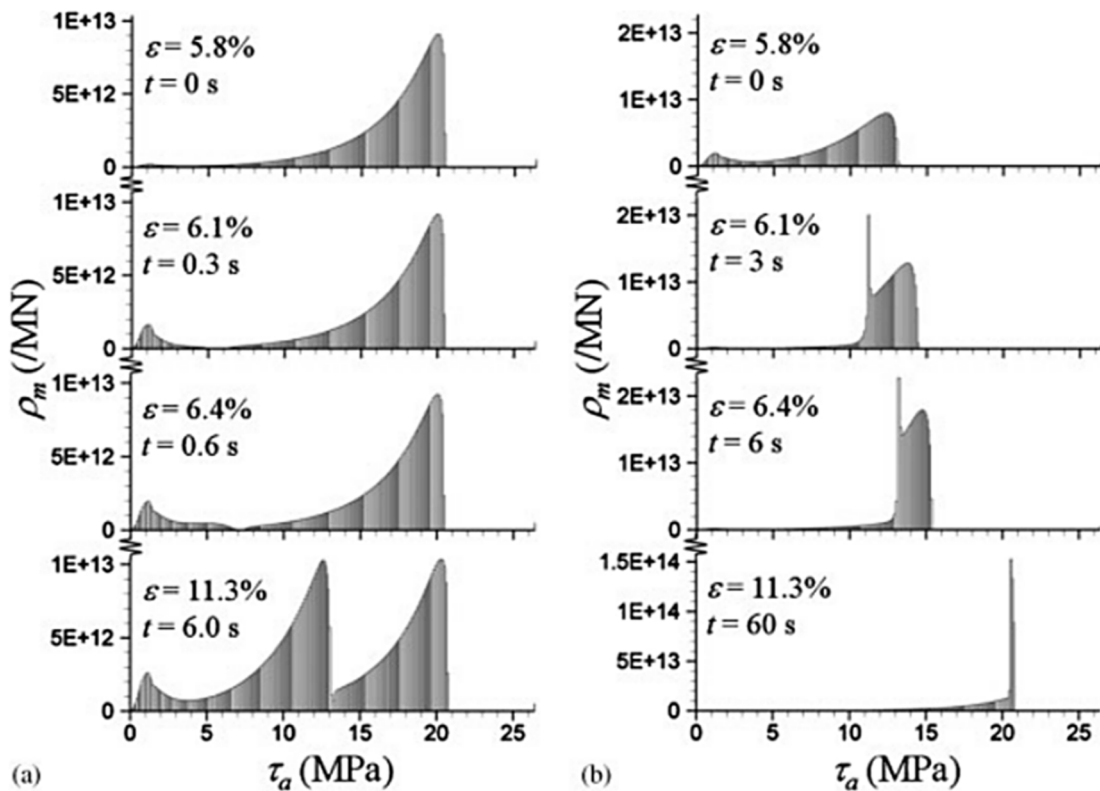
**Fig. 23.** Simulated distribution functions of the instantaneous number of dislocations, $\rho_m(\tau_a)$, with a given solute atmosphere pinning strength, $\tau_a$, and its evolution in time. A change in strain rate is performed at t = 0 s. The initial distributions (t = 0 s) show a peak about a mean obstacle strength. (a) Upon a rate increase, dislocations must slip more frequently, thus over time dislocations unpin and subsequently spend a reduced time arrested between flight. (b) Upon a rate decrease, the rate of dislocation escape from their solute atmospheres decreases, thus the mean time a dislocation spends arrested increases to a new steady state [261].

### 3.2.1. Transient behaviour

The explicit time dependence of solute diffusion to dislocation cores was removed in the DSA model presented, by assuming it is sufficient to consider its time average in a steady state ($t_D = t_W$, Eq. (17)). Hence the model fails to predict deformation history effects. In reality, flow stress transients have been observed upon a sudden strain rate change in the domain of serrated flow, including in TWIP steels [24], stainless steels [238–240], Au-Cu [241,242], superalloy Inconel X-750 [243] and Al-Mg-Si alloys [244–247], characterised by a positive initial SRS, followed by relaxation to a negative SRS, as shown in Fig. 22(a) [17,248,249]. Contrary to in other systems, previous strain rate jump tests on RR1000 at 600 °C – 775 °C did not show much evidence of a transient response on a jump in strain control, neither did they show much rate sensitivity except at the highest temperatures where the rate sensitivity was positive (Fig. 22 (b)) [250,251][3]. Flow transients have also been reported in high purity FCC metals such as Al [252] and Cu [253,254] and for smoothly deforming Ti alloys [255], though maintaining a positive SRS in steady state. These are typically not believed to relate to DSA, but rather time dependent changes in the dislocation structure following a strain rate jump, for instance through a change in the balance between dislocation generation, through multiplication, and removal processes, through annihilation, locking reactions or dynamic recovery [249,256–258]. Effects of strain rate on the densities of mobile and immobile dislocation populations are neglected in the models for DSA presented above [256][4].

However, transient behaviour may also be expected due to DSA [17,249], and it is suggested that this dominates when DSA operates [260]. The transients observed during serrated flow have unique characteristics from those typically associated with changes to the dislocation population, in that they initially overshoot ('inverted' transients [249]) but such that the initial change is in the opposite direction to the steady state change (Fig. 22(a)). McCormick explains this because, on a sudden change in strain rate, there can be no sudden change in the solute distribution around dislocations [17]. Hence the instantaneous response will be that with the structure fixed, which is invariably characterised by a positive SRS. On a strain rate increase, the instantaneous strengthening effect

---

[3] Refer to Section 5.2 for potential difficulties in comparison between the tests performed under crosshead displacement control and extensometer measured strain control, such as those in [250].

[4] See the Aninthakrishna model [234,259] for an alternate DSA model which focuses on the changes in mobile and immobile dislocation densities through a dislocation reaction–diffusion scheme, rather than on effects on the activation energy barrier.
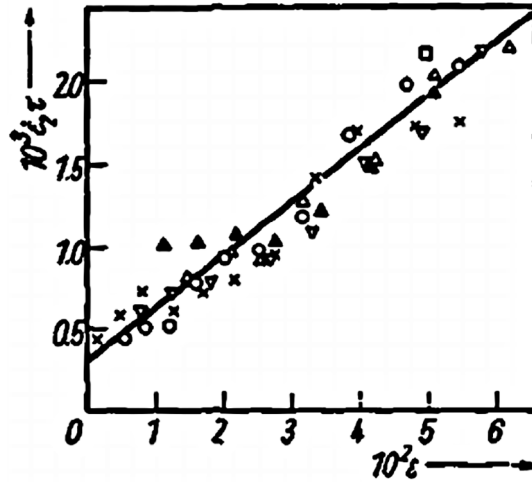
**Fig. 24.** Plot of the relaxation strain, $\dot{\varepsilon}_2 t_0$, versus strain $\varepsilon$ at which rate jump was performed for Au-4.5 at.% Cu deformed at room temperature, where $\dot{\varepsilon}_2$ is the strain rate after the rate jump and $t_0$ is the relaxation time [241].
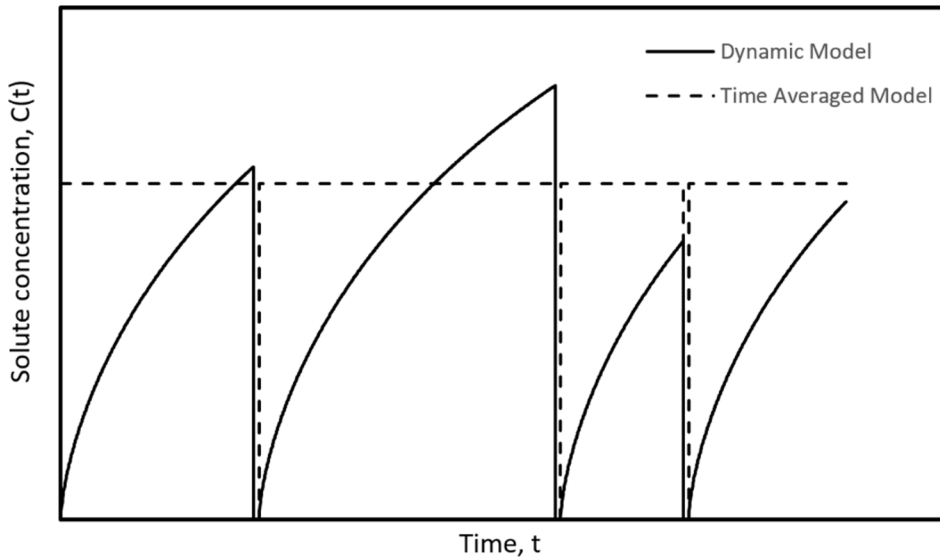


**Fig. 25.** Schematic plot of the evolution of solute concentration around a single dislocation core with time. Early models which introduce a mean arrest time of dislocations [236] assume the rapid formation of a solute atmosphere which does not vary in size, whereas dynamic theories [235] for DSA track the evolving solute concentration around a dislocation with time.

due to DSA is greater than that expected in steady state, since the dislocations present at the slower strain rate had a greater average arrest time hence greater solute build up. The converse argument can be made upon a rate decrease. Hence, over time additional solute will diffuse to dislocations (strain rate decrease) or dislocations will break free from their excess atmosphere (strain rate increase), leading to a time dependent relaxation to the new steady state negative SRS (Fig. 23). Several have accounted for this relaxation in an ad hoc manner by assuming that the activation enthalpy [262,154,263], SRS [17,248,204] or, most commonly, the instantaneous mean dislocation arrest time, $t_D(t)$, [17] displays first order relaxation kinetics between steady states, such that the mean arrest time evolves as

$$\frac{dt_D(t)}{dt} = \frac{t_W - t_D(t)}{t_0},$$
(25)

for a relaxation time $t_0$, relaxing towards a steady state value equal to the mean waiting time (Eq. 17) [17]. Each approach differs only in the mathematics.

The factors controlling the relaxation time $t_0$ are unclear. McCormick suggests that the relaxation time will be of the order of the new waiting time (Eq. (17)), since on average, each dislocation should have had time to be reactivated and thus break free from its pre-
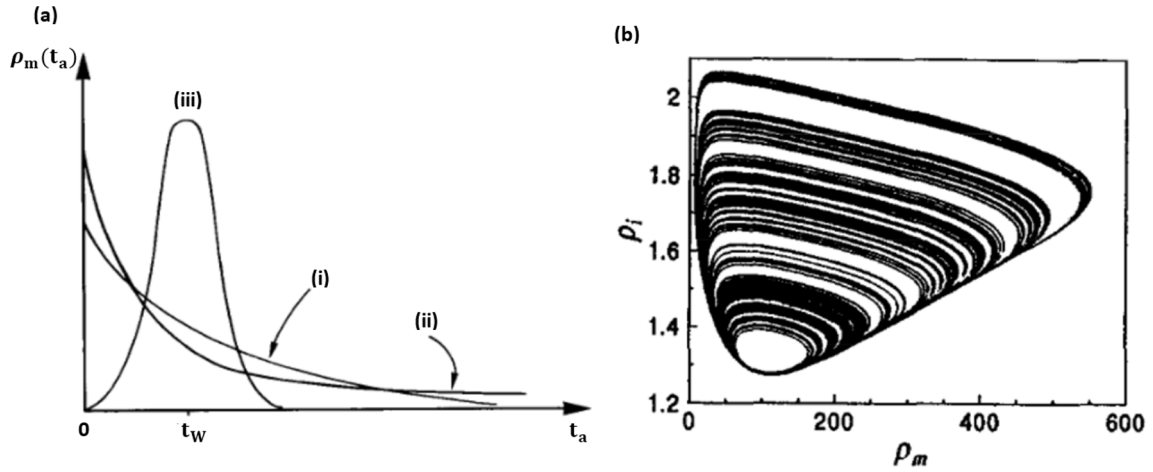
**Fig. 26.** (a) Schematic distribution functions of waiting times for non interacting dislocations [235]. (i) Distribution in the absence of DSA resembles a lifetime distribution, where the escape probability is independent of time. (ii) Distribution function in the presence of DSA. Strain ageing increases the proportion of deformation carried by scarcely aged dislocations, but also increases the fraction of heavily aged dislocations. (iii) Proposed $\delta$-function like distribution in previous models such as [15]. The Ananthakrishna model [234,259] correspond to $\delta$-function peaks at $t_a = 0$ and $t_a = \infty$ (not shown). (b) Time evolution of mobile and immobile dislocation densities in the Ananthakrishna model. Serrations are associated with bursts of increasing mobile dislocation density [131].

existing atmosphere, determined by the prior strain rate, and form a new atmosphere [236,249,17]. Limited results indicate that the relaxation time increases with strain [264,241] or decreasing strain rate after the jump [241], as predicted (Fig. 24). Some authors suggest using a different relaxation time for increasing and decreasing solute concentration, noting that different processes control the relaxation (solute diffusion and dislocation breakaway) [154,247]. Brief attention is drawn to the dynamic theories for DSA of Ananthakrishna [234,259] and of Hähner [265,235] (further advanced in [266–268], respectively), which do not remove the explicit time dependence from strain ageing by introducing a mean waiting time (Fig. 25), hence are able to predict history effects. Starting from an Arrhenius law of the form of Eq. (19), their models differ by allowing a distribution of mobile dislocations, $\rho_m(t, t_D)$, with different ageing times $t_D$ at time $t$, such that, by averaging over all the possible ageing times, the strain rate is given by

$$\dot{\varepsilon}(t) = bd\nu_0 \int_0^\infty \rho_m(t, t_D) e^{-\frac{H(t, t_D)}{kT}} dt_D, \tag{26}$$

where $d$ is the mean glide distance of a dislocation once unpinned and the activation energy $H(t, t_D)$ is given by Eq. (20), without assuming steady state conditions. Thus, the time evolution of the system can be evaluated if the time evolution of the dislocation population is known (Fig. 26(a)).

The Ananthakrishna model assumes a simplified form of the distribution of ageing times, such that all mobile dislocations are either free from solute ($t_D = 0$) or heavily aged ($t_D$ large such that the probability of unpinning tends to zero) [234,259]. Thus, based on a simplified set of dislocation reactions, where a fraction of mobile dislocations immobilise or a fraction of immobile dislocations break free per unit time, the evolution of dislocation populations can be modelled (Fig. 26(b)). Clearly this oversimplifies the ageing process[5]. Hähner derives details of the mobile dislocation distribution by considering how the existing distribution evolves in time. At a given time $t$, the number of mobile dislocations with ageing time $t_D$ will be equal to the number which became pinned at $t - t_D$, multiplied by the probability that they do not escape at times $t'$ in the range $t - t_D < t' < t$, given by [267]

$$\rho_m(t, t_D) dt_D = \left( \frac{\dot{\varepsilon}(t - t_D)}{bd} dt_D \right) e^{-\int_{t-t_D}^t \nu_0 e^{\frac{H(t', t'-t+t_D)}{kT}} dt'}, \tag{27}$$

where the left and right terms represent the former and latter contribution, respectively. Hence, combining Eqs. (26) and (27) enables prediction of the evolution of plastic strain from past strain rates. Hähner uses this to derive a more complex expression for the relaxation time [265]. The steady state behaviour can be predicted from the normalisation condition

---

[5] Another difficulty in application of the Ananthakrishna model to FCC alloys arises, since the saturated locking force is typically believed to be weak [20]. In the model, the generation of new mobile dislocations occurs only through dislocation multiplication or remobilisation of immobile (for instance sessile) dislocations. It is not clear whether neglecting the breakaway of dislocations from weak solute atmospheres will substantially alter the physics. Dependences of ageing on temperature and strain are also neglected. Nonetheless, the model has found some success in predicting the behaviour of serrations, for instance reproducing power law and chaotic states at different strain rates [269].
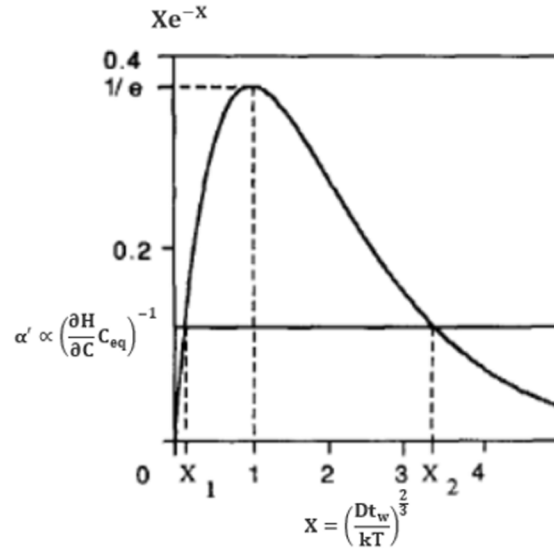
**Fig. 27.** Stability criterion for serrated flow [237]. A negative strain rate sensitivity is observed within two critical conditions $X_1$ and $X_2$, where $Xe^{-X} > \alpha'$, as predicted by Eq. (24).

$$\int_0^\infty \rho_m(t, t_D) \mathrm{d}t_D = \rho_m, \tag{28}$$

since the integrand is no longer a function of time *t*. Soare and Curtin give slightly different derivations of the same expressions [267,268].

One conclusion reached in Hähner's model is that DSA of non interacting dislocations does not lead to a negative SRS in their framework, on the basis that the derivative of the steady state strain rate (combining Eqs. (27) and (28)) with respect to stress is positive definite [267,235]. Both note that this is clearly at odds with experiment. This result should perhaps not be considered surprising, since following the ideas of Penning [10], spatially and temporally homogenous solutions exist only when the SRS is positive. Thus, additional justification is needed as to how strain localisation develops [270].

### 3.2.2. Inverse DSA

The classical models for DSA discussed predict a 'normal' critical strain dependence, since higher strain rates or lower temperatures lead to the balance between solute and dislocation mobility being met at higher strains (Fig. 21). However, in many substitutional alloys showing serrated flow, this trend holds at low temperatures/high strain rates only, for instance as shown in Fig. 5. This could indicate the operation of other Pseudo-PLC effects (Section 3.3), but several papers have rationalised 'inverse' behaviour within the framework of DSA.

Classes of models exist which attempt to explain 'inverse' DSA through consideration of the strain dependencies of terms in Eqs. (17) and (24), for which the resulting stability criterion is sketched graphically in Fig. 27 [237]. Conventional models treat $\alpha'$ (as defined in Eq. (24)) as a constant and X, defined in Fig. 27, as increasing with strain (through the diffusivity and mobile dislocation density), temperature (through the diffusivity) and decreasing strain rate (through the waiting time), predicting serrations begin when $X_1 \leqslant X$, leading to a 'normal' critical strain. Conversely, Kubin and Estrin assume that forest hardening is the dominant strengthening mechanism, in which case the obstacle spacing, $d \propto \rho_f^{-1/2}$, decreases with strain, where $\rho_f$ is the forest dislocation density [237]. Thus, the waiting time (Eq. (17)) and hence X both show a maximum with strain, due to the competition between increasing forest and mobile dislocation densities. Provided the maximum value of X is greater than $X_2$, serrations will first appear in the range $X_1 \leqslant X \leqslant X_2$, but then disappear, and reappear when $X \leqslant X_2$, leading to an 'inverse' behaviour of the critical strain in the latter case [237]. However, it is not clear that this can explain the range of alloys and microstructural conditions in which serrations occur: in particular, this always predicts a domain of 'normal' DSA preceding the 'inverse' domain on the stress–strain curve. Further, experimental measurements of the waiting time do not appear to indicate a maximum with strain [247].

Böhlke et al. note that an 'inverse' trend can also be reproduced if the conventional model is modified to allow the saturation locking strength, $\frac{\partial H}{\partial C}C_{eq}$, to be a increasing function of strain [124,271,272]. In particular, this implies graphically that $X_2$ and X both increase with strain. It is possible to envisage a scenario where $X_2$ increases with strain faster than X, predicting an 'inverse' trend with serrations beginning when $X \leqslant X_2$ first. While data availability is not widespread, experimental measurements based on fitting of DSA models to strain-rate jump transients or yield point phenomena may indicate that such trends in the parameters does hold [230,273,274,247]. Physically, the increase in saturation locking strength has been related to an increased total length of dislocation line with strain, thus greater capability for DSA [272], though it is not clear whether it is sound to apply this argument in a model which averages to consider the mean locking around a single dislocation.
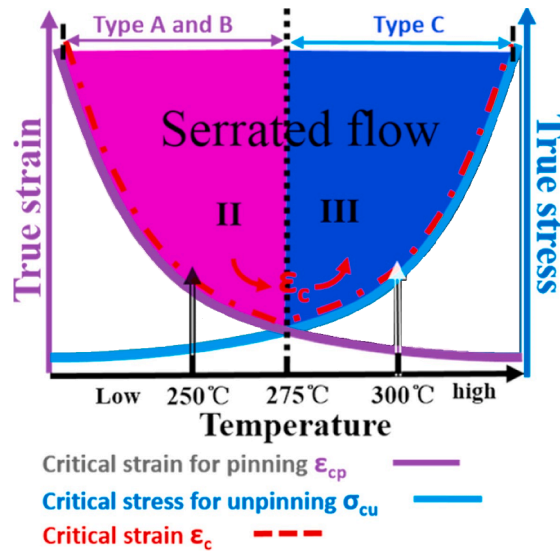
**Fig. 28.** Predicted critical strain versus temperature relation if limited by dislocation unpinning at high temperatures. At low temperatures, the critical strain decreases with temperature as classically, whereas the stress to break free of a solute atmosphere increases with temperature as a larger solute atmosphere forms [277].

Other classes of models rationalise the 'inverse' behaviour by assuming that under high temperature/low strain rate conditions, solute atmospheres rapidly form round a dislocation, and that dislocations only begin breaking free from their solute atmospheres once the stress has reached a sufficient level [61,83,275,276]. This suggests that prior to the onset of serrations, most plastic deformation must be mediated by newly generated atmosphere-free dislocations, or dislocations slowly moving with their solute atmospheres: two processes neglected in the classical models. Some simplistic efforts to model the behaviour at high temperature have been made [61,275]. Fu et al. argue that the critical stress needed for dislocations to break free from their atmospheres will scale with the DSA strengthening effect (Eq. (21)) [61,83]; thus a similar trend in this critical stress may follow, increasing with temperature and decreasing strain rate (Fig. 28). Another interpretation suggests that the transient nature of DSA is responsible for 'inverse' DSA [265]. The usual condition for serrated flow states that serrations begin when the SRS becomes negative, but the instantaneous change in stress upon forming a localised deformation band should be positive, since the instantaneous SRS is positive (Fig. 22), thus opposing the tendency for flow localisation. A more stringent condition for serrated flow by DSA reads [265,17,204]

$$S_{ss}\mathrm{d}(\ln\dot{\varepsilon}) + (h-\sigma)t_0\mathrm{d}\dot{\varepsilon} < 0, \tag{29}$$

where $S_{ss}$ is the steady state SRS after the relaxation time $t_0$ (Eq. (25)). Qualitatively this can be understood, since inside the localised band, there is an increase in strain rate, $\mathrm{d}\dot{\varepsilon}$, and hence an increase in work hardening rate with respect to time. In order for the stress to be lowered by forming a localised band, the extra work hardening over the time where the SRS relaxes to its negative value must be offset by the SRS. In other words, serrated flow will only begin once the SRS hits a finite negative value.

This delay to the onset of serrations associated with the transient behaviour of DSA also appears to be the origin of 'inverse' DSA in Hähner's model for serrated flow [265]. Qualitatively, at slower strain rates, the relaxation time is greater [17]. Hence the SRS value at which serrations begin becomes more negative, requiring more strain accumulation to reach. However, it is not clear that this accounts for the accompanying 'inverse' trend in temperature, nor that the relaxation time is an appropriate measure of the time required for localised band initiation [247]. While it is common to use the relaxation times $t_0$ in Eqs. (25) and (29) interchangeably, it is noted that the time scale over which a localised band develops is typically distinct and much shorter than the relaxation time upon a rate jump, with the former representing the mean time for a dislocation to be reactivated and thus break free from its prior solute atmosphere, whilst the latter represents the time scale over which correlated dislocation motion occurs [247].

It is considered plausible that these arguments, particularly the former two, may enable understanding of 'inverse' DSA without requiring an entirely distinct mechanism between 'normal' and 'inverse' DSA, as is commonly suggested. It is worth noting that it is common in the literature to attempt to extract an activation energy for solute diffusion from the critical strain when 'inverse' DSA operates using Eq. (16). Without an accepted model for 'inverse' DSA, it is not clear without further justification that it is reasonable to consider the exponent $Q$ to be equal to an activation energy for diffusion in this case. For example, Hayes and Hayes assume that the calculated activation energy is the enthalpy of reaction for carbide precipitation responsible for the disappearance of serrated yielding [278].

### 3.2.3. Spatial coupling and synchronisation

A key approximation in the classical models described prior (Eq. (21)))) is to limit consideration to a single non-interacting 'average' dislocation. It is perhaps unsurprising that modelling the critical strain is their biggest success, since the approach taken
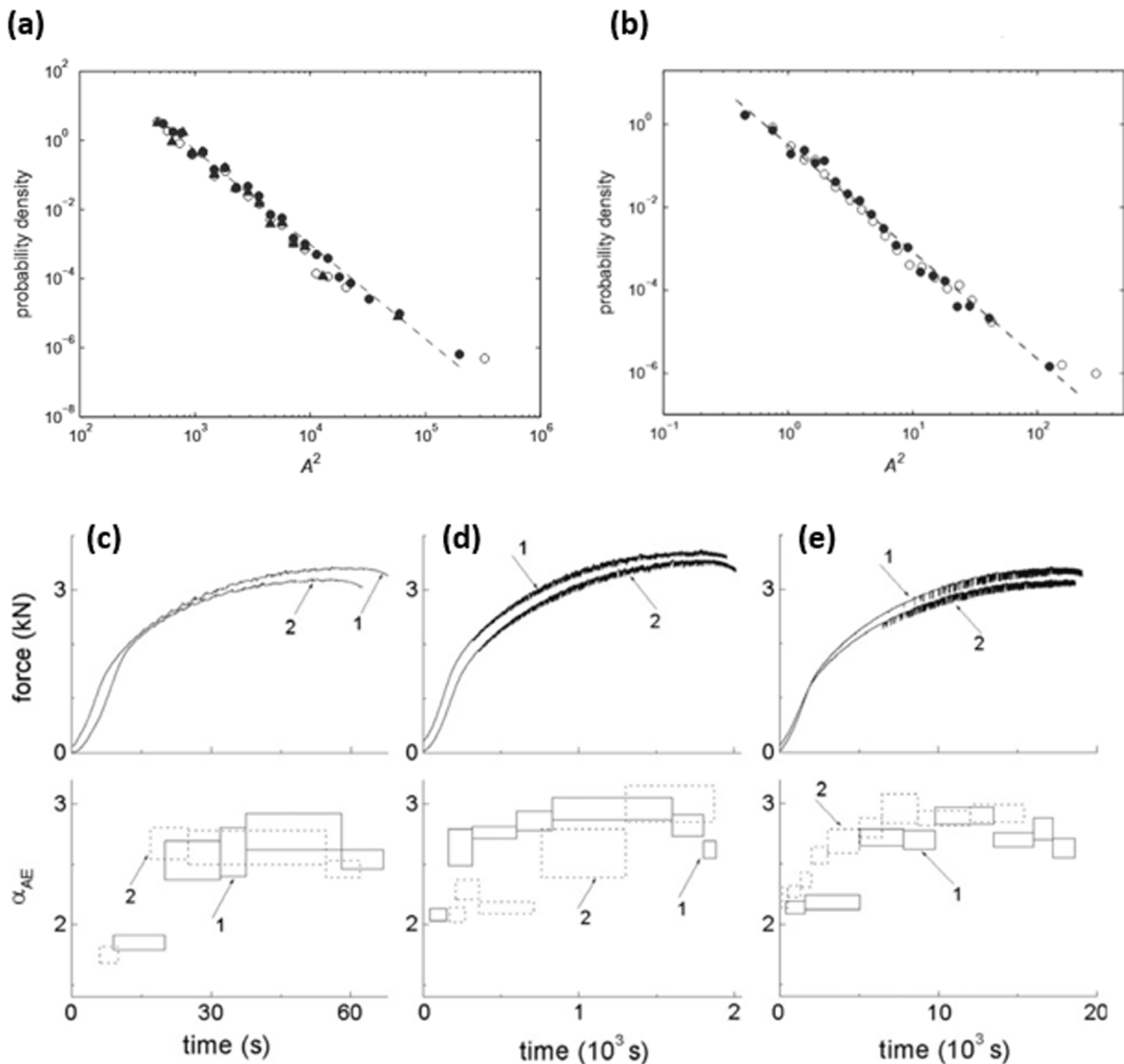
**Fig. 29.** Top: distribution of stress drop avalanches, P($A^2$), observed in a Al-3 Mg binary alloy deformed at room temperature and (a) $2 \times 10^{-5}$ s$^{-1}$, Type C (b) $6 \times 10^{-4}$ s$^{-1}$, Type A/B. Solid/filled circles represent changes to analysis parameters. Bottom: force–time plots for the same alloy deformed at (c) $6 \times 10^{-3}$ s$^{-1}$, Type A (d) $6 \times 10^{-4}$ s$^{-1}$, Type B (e) $6 \times 10^{-4}$ s$^{-1}$, Type C. A repeat test was performed for each condition. Corresponding values of the power law exponent, $\alpha_{AE}$, are represented below each plot as rectangles, with vertical dimension representing the uncertainty and horizontal dimension representing the range of times used for analysis [139].

considers the limit of stability of a stable (temporally and spatially homogenous) system, where consideration of an 'average' dislocation may constitute a more reasonable approximation.

When one attempts to describe details of the stress–strain spatiotemporal behaviour during serrated flow, the inadequacy of this approach becomes clear. As discussed in Section 2.1, Penning showed that stress–strain oscillations follow from consideration of the evolution of a flow stress model with negative SRS, such as Eq. (21) [10]. Simplistic arguments take the serration amplitude to be proportional to the DSA strengthening effect (Eq. (21)) [111,101,102,115,117,278,114,279,280], since serrations are linked to the breakaway of dislocations from their Cottrell atmospheres. The predicted increase in serration amplitude with temperature, strain and decreasing strain rate has been observed in some instances (Section 2.3). However, it is unclear how such an approach can account for the various observed statistics of serration amplitudes (Section 2.3), or predict the absolute magnitude of stress drops. Empirically, plastic strain bursts can be of the order 0.1 %, requiring the concurrent movement of tens of thousands of dislocations.

Thus, key to the advancement of DSA models is the inclusion of spatially dependent interactions or couplings between dislocations [281,282,269,19], to account for collective dislocation dynamic effects. Experimental evidence based on AE, as presented in Section 2.3, provides some hints about the nature of the coupling involved. As shown in Fig. 10, results suggest that serrations are accompanied by a number of mesoscale slip avalanches, not individually dissimilar from those in periods of smooth flow or in materials exhibiting
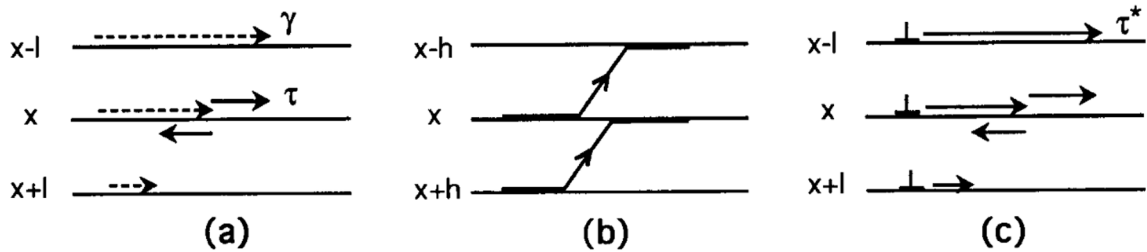
**Fig. 30.** Schematic illustration of proposed mechanisms for spatial coupling [281]. (a) Elastic incompatibility stresses required to compensate for differences in local plastic strain, $\gamma$, between finite elements, for continuity of total strain. Dotted arrows represent the magnitudes of plastic strains in three finite elements. The element at position $x$ experiences two additional stresses, $\tau$, represented by solid arrows, due to the difference in accumulated plastic strain from its neighbours: forward and back stresses for total strain continuity with the elements at $x-l$ and $x+l$, respectively. (b) Exchange of dislocations between slip planes by cross slip. (c) Elastic interactions between dislocation stress fields, for instance tending to align dislocations on parallel planes in arrays.

smooth flow [139,135,140]. Such intermittent avalanche processes are widely considered ubiquitous to plastic flow [137,138,283,19], reflecting the activation of further dislocations upon stress redistribution.

Conceptually, one might suppose that DSA would lead to larger avalanche events since, once the first dislocation remains free of its solute atmosphere, it may continue gliding more easily and leads to a greater need for local stress redistribution, inciting further breakaway [284]. It should be noted that the empirical evidence [139,135,140], for instance in Fig. 10, does not rule this out, since a direct comparison of smooth/jerky flow is only easily made under a single set of experimental conditions exhibiting DSA, taken before/ after the critical strain respectively. It is widely accepted that DSA is still operative prior to the critical strain, as evidenced by a SRS decrease (Section 4.1), just in conditions insufficient to generate macroscopic serrations.

Indeed, some differences in the elementary slip events do seem present in cases where DSA operates, as shown in Fig. 29. Empirical investigations of AE event statistics have indicated that avalanches in the presence of DSA may tend to show larger power law exponents, $\alpha_{AE}$ [139,136,135,19], where

$$P(A^2) \propto A^{-2\alpha_{AE}} \tag{30}$$

relates the probability, $P(A^2)$, of slip events of magnitude $A$. $\alpha_{AE}$ also showed weak dependencies on strain and strain rate (Fig. 29) [139,284]. Thus, there often appears to be a preference towards relatively (though not necessarily absolutely) smaller avalanches when serrated flow is observed, compared to in pure or smoothly deforming materials. However, the opposite (and perhaps more intuitive) trend was observed in [285], with a relative preference for larger avalanches during the PLC effect attributed to synchronisation. The increased $\alpha_{AE}$ observed in some cases was suggested to relate to the presence of increased strengthening obstacles, which inhibit large avalanches or correlations [139,284]. This was suggested to be a consequence of DSA [139], though could also be expected, due to the use of larger strains to investigate the PLC regime in Fig. 29, in order to exceed the critical strain. Alternatively, one could also speculate whether the increase in $\alpha_{AE}$ arises from a finite size effect [188]. For instance, as sample dimensions become a more prominent factor in limiting the volume over which an avalanche can propagate, or since the spatiotemporal inhomogeneity of deformation implies that only a smaller sub region of dislocations may be close to criticality. However, experimental evidence suggests that individual slip events are not sufficient for serrations, even if enhanced by DSA. Rather, multiple chained slip events are required for serrated flow, particularly for Type C serrations and presumably occurring locally as evidenced by the formation of distinct slip bands (Section 2.4) [139,135,140]. This idea can be compared to classical concepts of serrated flow (Eq. (5)), that a distinct serration only develops when conditions favour the growth of perturbations, through the chained occurrence of dislocation avalanches [247].

Further understanding is necessary on the mechanisms of the spatial interactions or couplings responsible for the distinct spatiotemporal patterns of serrated flow on different length and time scales and under different conditions [19]. In particular, experimentally it is found that synchronisation of avalanches is most prevalent for Type C serrations, and thus it was suggested that the change in serration amplitude statistics between Types A and C (Fig. 9) reflects a change in coupling interactions [139,136]. Generic mathematical models for avalanche behaviours can reproduce avalanche statistics resembling power law distributions expected for SOC models or peaked distributions with avalanche synchronisation, depending on the nature of the coupling between elements [286]. However, a detailed explanation is lacking of how the coupling between elemental avalanches varies with experimental conditions, resulting in distinct serration statistics. Further, clarification is needed on why coupling is more apparent on mesoscopic time scales between avalanches, than on the timescale of an avalanche itself.

Various mechanisms have been proposed for the spatial interactions at different length scales, as shown in Fig. 30: see e.g. [281,282,269] for a review. The most common are based on elastic interactions, considering instantaneous incompatibility stresses between discrete elements at the macroscale, required for continuity of total strain between heterogeneously deforming elements [287,126,125,119,288]. However, alternate coupling mechanisms have been suggested to dominate at different length or time scales. For instance, elastic wave propagation [139]; coupling across slip planes through cross slip [282,269,202,203,281,289] and dislocation–dislocation stress field interactions [282,270,290], have been suggested as mechanisms for coupling on the finer scale, though Hähner [270,165] and Hähner and Rizzi [263] take the view that dislocation–dislocation interactions can extend over much
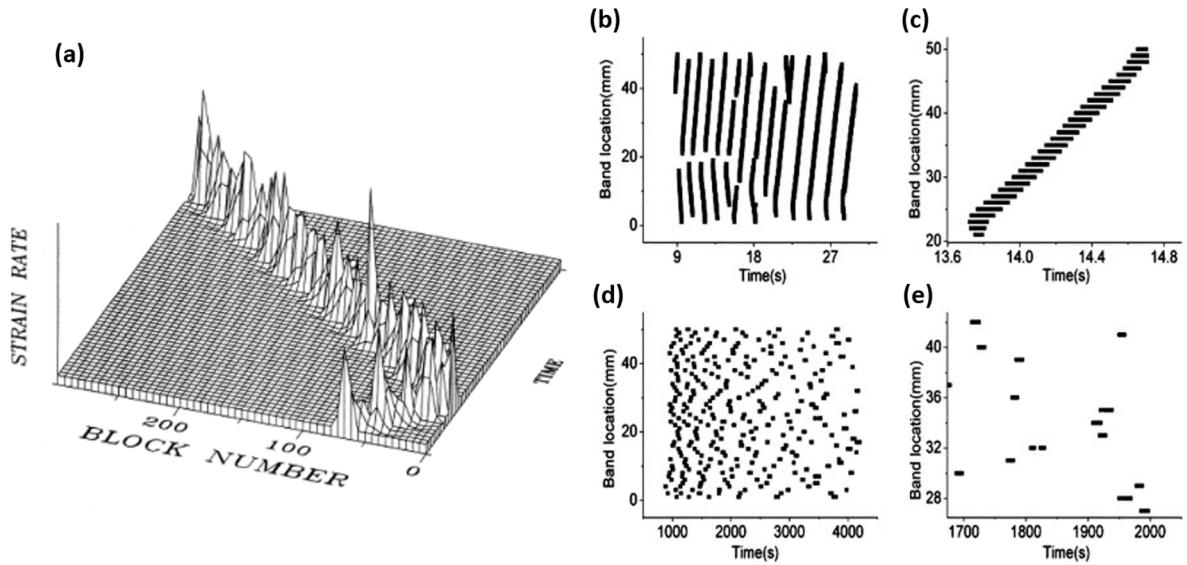
**Fig. 31.** (a) Time evolution of strain rate profile along gauge length for numerical solution to material constitutive equations, accounting for spatial coupling through incompatibility stresses between finite elements [126]. A continuously propagating localised band is observed. (b)(c) Correlated propagating bands or (d)(e) uncorrelated non-propagating bands are observed for different strengths of coupling between elements [292].

larger correlation distances in the limit of vanishing SRS. Implementation of spatial interactions into predictive DSA models has been largely limited, thus far, continuing to pre-impose local synchronicity of dislocations by defining mean waiting times of dislocations at obstacles [235]. Some success in modelling full spatiotemporal characteristics during serrated flow has been achieved by partial relaxation of this assumption to consider continuum scale models where properties are only locally homogeneous. Approaches have largely considered mechanical interactions between such mesoscopic elements based on Eshelby incompatibility stresses [291], as sketched schematically in Fig. 30(a), by adding an additional spatially dependent term, such that the back stress on the $i$ th element, $\sigma_{0,i}$, in Eq. (21) is modified to

$$\sigma_{0,i} = \sigma_0' - \frac{E}{l^2}((\varepsilon_{i+1} - \varepsilon_i) - (\varepsilon_i - \varepsilon_{i-1})),$$ (31)

for a constant $\sigma_0'$, where $\varepsilon_i$ denotes the plastic strain of the $i$ th element, of length $l$ and elastic constant $E$ [119,126]. Or correspondingly, in the continuum limit, the back stress at position $x$, denoted $\sigma_0(x)$, is modified to

$$\sigma_0(x) = \sigma_0' - E\nabla^2_{xx}\varepsilon(x),$$ (32)

where strain is treated as a function of $x$ [126,125,119,288]. It can be seen that upon a local increase in plastic strain, the stress on adjacent elements rises, thus increasing the probability of dislocations in the adjacent elements breaking free. While the approach as discussed above limits consideration to a 1D stress/strain state, Schwab and Ruff show a similar form of interaction is reached by considering yield criterion in the presence of incompatibility stresses between elements for a triaxial stress state [287].

However, Kubin suggests that long range elastic interactions cannot fully account for the coupling, since when a sample was interrupted part way through band propagation then aged for a long time so that dislocations were 'locked', a new band was initiated at the end of the specimen rather than continuing from ahead of the previous band, where the analysis presented would suggest the stress was raised [281], though one could suggest that such observations are explained by stress relaxation over the ageing time.

FE implementations (in 1D [119,126,292] or 3D [103,293,271,124]) or numerical integration procedures based on solving the system of Eqs. (7), (19), (20), (25) and (31), have had success in reproducing various characteristics of serrated flow. For instance, trends in critical strain [271,124] have been reproduced, with suitable implementations of the DSA equations (Section 3.2.2), and in the serration statistics [119,126]. Analytical travelling wave solutions were found in 1D when such a spatial dependence was added to an Arrhenius rate law: from this it was shown that the band speed increases with both crosshead velocity and work hardening coefficient [163,263,154].

The key success of such models is that spatiotemporal characteristics resembling Type A, B or C propagation can be predicted with appropriate parameter tuning [124,119,126], as shown in Fig. 31. In particular, Type C serrations tended to follow when the spatial coupling term, $E$, is small [119,126,292]. This result can be placed into theoretical context by the arguments of [19]. The tendency for spatial correlation is driven by the incompatibility stresses [291], resulting from the development of a localised band [126,125,119,263,154,288,282,165]. Their plastic relaxation is possible over the timescales of reloading following a Type B or C load drop, and would be more significant at higher temperatures or lower strain rates. Thus, Type C serrations tend to have the smallest coupling on a macroscale and thus show the least spatial correlation [126,293,135,187,19,292]. It is not clear that differences in the

**Table 4**

Summary of key features of several DSA models arranged chronologically. 'Drag', 'Breakaway' and 'Generation' refer to the processes for continued deformation considered once a solute atmosphere has formed, such that dislocations glide with their solute atmospheres, dislocations break free from their solute atmospheres, or new dislocations are generated to mediate plasticity, respectively. Models are classed as 'Dynamic' if they allow the solute concentration around a dislocation core to evolve with time rather than considering a time average; 'Spatially Coupled' if they account for interactions between dislocations as opposed to considering isolated dislocations and as considering a 'Dislocation Population' if they do not average properties such as the solute concentration over all dislocations. * Coupling used is non spatially dependent.

| Author | Deformation Processes | Spatially Coupled | Dynamic | Dislocation Population |
|---|---|---|---|---|
| Cottrell [209] | Drag | | | |
| McCormick [15] | None | | | |
| Van den Beukel [236] | Breakaway | | | |
| Ananthakrishna [259] | Breakaway Generation | | ✓ | |
| McCormick [17] | Breakaway | | ✓ | |
| Lebyodkin [119] | Breakaway | ✓ | | |
| Hahner [235] | Breakaway | | ✓ | ✓ |
| Rizzi [154] | Breakaway | ✓ | ✓ | |
| Fressengeas [266] | Breakaway Generation | | ✓ | |
| Ananthakrishna [269] | Breakaway Generation | ✓ | ✓ | |
| Zhang[261] | Breakaway Generation | ✓ | ✓ | ✓ |
| Carroll [62] | Breakaway | ✓* | ✓ | |

serration statistics can be accounted for by the same argument, since the time scales of development of a sharp load drop are presumably too fast for significant stress relaxation. However, FE models based on such methods tend to fail in capturing the shapes of the various experimentally observed serration Types accurately (Fig. 7(a)). In particular, the time variation in such models stems from the inclusion of a relaxation time, $t_0$, as in Eq. (25), describing the lifetime of transients in the baseline stress upon strain rate changes and commonly approximated by the mean waiting time to reactivate a given dislocation, such that it breaks free from its historic solute atmosphere [236,249,17]. As noted in Section 3.2.2, this may be distinct from the timescale over which correlated dislocation motion occurs and thus a localised band develops [247]. Thus, capturing the timescales of serrations accurately requires a greater understanding of the dislocation synchronisation processes responsible.

Other analytic models have neglected the spatial dependence of coupling by assuming mean field interactions between discrete elements rather than solely nearest neighbour interactions [62,294–298], of the form

$$\sigma_{0,i} = \sigma_0' - J\sum_j (\varepsilon_j - \varepsilon_i),$$ 
(33)

where $J$ is the mean field coupling constant and the summation is performed over all elements as opposed to just nearest neighbours. Larger and less frequent serrations resembling Type C serrations were found at higher temperatures on account of the greater stress required to be redistributed and the serration statistics at low temperatures resembled the power law statistics expected for Type A serrations [62].

### 3.2.4. Summary

Table 4 summarises the key features accounted for in several DSA models. It is not clear that any model fully captures the complexity of DSA. Thus, it is to an extent unclear whether the inability of current models to fully capture empirical features of serrated flow in FCC alloys, such as 'inverse' DSA and different band propagation characteristics (Section 2), is due to a deficiency in the models used, in the application of the theory of strain ageing, or a combination of both. The inability of current DSA models to fully account for experimental observations has led to the speculation of alternate theories (Section 3.3).

It is worth highlighting that the models discussed are mainly based on Cottrell-Bilby ageing kinetics (Eq. (8)), derived for the case of bulk diffusion of solute to a core based on long range hydrostatic interactions, or based on a generic ageing function $C(t)$ representing the build up of solute. There is not a clear picture of the possible solutes involved, nor of the diffusion pathways and nature of the interactions when applying strain ageing to FCC alloys. Limited experimental evidence has been obtained of the atomic scale processes responsible for serrated flow in superalloys, for instance based on chemical analysis to identify a solute atmosphere through APT or Energy Dispersive X-ray Spectroscopy (EDX), as discussed in Section 5.4. Equally, there has been little computational work assessing the thermodynamics (such as the binding energies of various solute–defect configurations) or kinetics (such as activation energies for various reaction pathways) of different ageing mechanisms in superalloys, for instance through Density Functional Theory (DFT) calculations (Section 7).

### 3.3. Alternate theories for serrated flow

The ideas advanced by Sleeswyck [14] and Penning [10] (Section 3.1) suggest that any mechanism which leads to a negative SRS could lead to strain localisation and serrated flow, and the mechanism need not be DSA. The negative SRS condition for serrated flow is the commonly used condition to account for possible Pseudo-PLC effects [299–301]. While clearly not applicable in the present case, it is interesting to note a comparison to stick–slip phenomena in composite fibre pull out, where serrations are believed to arise due to the difference between static and dynamic friction [302]: in other words, the strength decreases with an increase in strain rate, though in
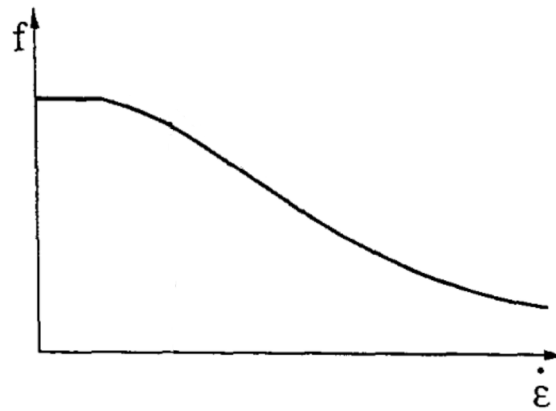
**Fig. 32.** Schematic proposed dynamic equilibrium precipitate fraction versus strain rate. The precipitate fraction is rate sensitive for an intermediate range of strain rates where rates of precipitate dissolution and re-precipitation are comparable [305].

this case the stress required is to dislodge a fibre rather than for dislocation motion.

### 3.3.1. Dynamic precipitation

Differences between the serrated flow behaviour of alloys in solution treated and precipitate hardened conditions led to speculation that precipitation may play a role in serrated flow, particularly in 'inverse' behaviour at high temperature since precipitates often delay the onset of serrations [102,303,304,278].

The shearing of fine precipitates is usually considered as a 'Type h' instability, reducing the work hardening as precipitate strengthening is lost when precipitates are fully cut, since no new precipitate matrix interface is created by further shearing on the same plane [305]. However, under specific conditions where concurrent shearing of precipitates and dynamic dissolution and re-precipitation is possible during testing, Brechet and Estrin envisaged a scenario where serrated flow may arise without the need for DSA, directly due to the formation of precipitates [305,306,299,307]. To summarise, the precipitate strengthening, $\sigma_{ppt}$, of cut precipitates could be modelled as

$$\sigma_{ppt} \propto fr^{1/2}, \tag{34}$$

for a volume fraction $f$ of precipitates of radius $r$. Suppose a dynamic equilibrium is reached between the rates of deformation induced precipitate dissolution and re-precipitation, such that the increased rate of precipitate cutting at faster strain rates leads to a reduction in the dynamic equilibrium precipitate fraction or size [305]. Thus the precipitate hardening due to cutting has a negative strain rate exponent (Fig. 32). This effect would be expected for an intermediate range of temperatures and strain rates, where the rates of precipitation and dissolution are comparable (where $\frac{df}{d\dot{\epsilon}}$ is largest, Fig. 32) [305]. Such a process has been considered to occur either through homogenous bulk nucleation of precipitates in the slip plane, or heterogeneous nucleation at dislocation cores due to a raised solute concentration via DSA [299]. However, it has been disputed whether this is observed [308]. Whether the fine precipitates required for such a mechanism contribute sufficiently to the strength to outweigh any positive contributions to the SRS is unclear. Experimentally, precipitates do not appear to be a requirement for serrated flow in several FCC alloys. While microstructural features such as precipitates are expected to influence serrated flow (Section 5.3), it is rarely suggested that they directly cause serrations in superalloys. Even if the shearing of precipitates does not directly cause serrations, if DSA does operate, any dynamic precipitation may be expected to significantly alter the behaviour, since dynamic precipitation may:

- Remove solute from the matrix responsible for DSA [278,299,102,303,309]
- Act as barriers to dislocation motion, allowing time for solute atmospheres to form [299,184,50]
- Inhibit dislocation avalanches [310].

Focusing mainly on the first effect, some consider dynamic precipitation concurrent to DSA as a possible origin of 'inverse' DSA [102], since a slower strain rate implies a greater dynamic equilibrium precipitate fraction, hence the critical strain is raised due to the reduced solute available in the matrix for DSA [299]. However, this has been disputed. For instance, in Al-Mg 'inverse' behaviour is still seen below the limit of solid solubility [311]. Such ideas are likely to suffer from the same doubts as DSA: namely, it is not clear if there is time for long range diffusion of solute to nucleate and grow precipitates under the conditions where serrated flow is observed [312]. It is typically felt that $\gamma'$ precipitates in superalloys are too stable to dissolve/slow to re-precipitate at 500 °C [78,9], though in some superalloys dynamic precipitation has been suggested to play a role [107].

### 3.3.2. Dynamic ordering

Analogous to the argument made for precipitates, a competition between thermodynamically driven formation of order and
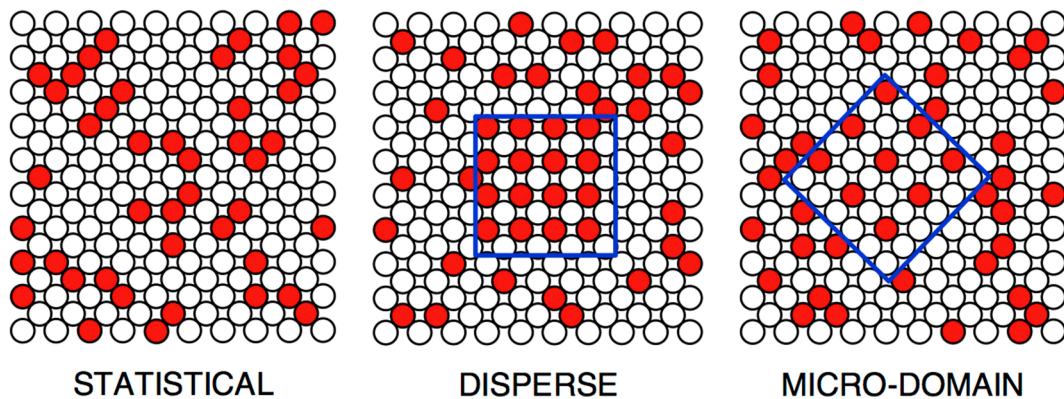
**Fig. 33.** Three models for short range order. Red and white circles represent two different atomic species. Statistical order is continuous throughout the matrix and represents a preference for like or unlike bonds. Conversely, disperse or micro-domain models contain heterogenous ordered regions, either with the same composition (micro-domain) or different composition (disperse) from the matrix [318].
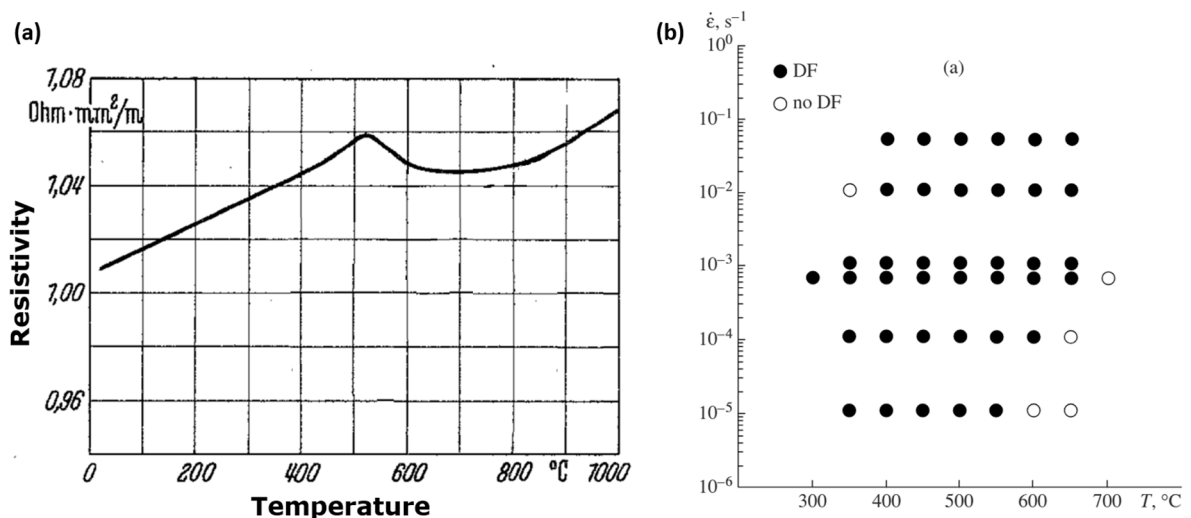


**Fig. 34.** (a) Resistivity-temperature plot for Ni-20Cr (wt.%). The anomaly is attributed to short range ordering [319]. (b) Temperature, $T$, vs strain rate, $\dot{\varepsilon}$ map showing domain of serrated flow (Discontinuous Flow; DF) in Ni-20Cr (wt.%) [76].

deformation induced disordering may lead to a domain where the extent of order hardening decreases with strain rate [300]. In the case of long range order, this competition may occur through the dissolution and re-precipitation of ordered precipitates and the argument is identical to that made for dynamic precipitation. In the case of short range order, three models are commonly identified: disperse, microdomain and statistical order, shown in Fig. 33 [313]. For microdomain or disperse ordering, deformation induced disordering may occur through similar cutting of ordered zones or in the case of statistical ordering, repeated shearing on different slip planes may tend to randomize the nearest neighbours [314,315,75,76]. The occurrence of the so-called 'K state' in nichrome is at similar temperatures to that for serrated flow (Fig. 34) [75]. Recent HRTEM work may indicate the formation of SRO domains with superlattice features along 111 planes in a NiCrCo alloy when heat treated at 1000 °C for 120 h [316], and a coinciding observation of load drops in Ti-6Al (wt.%) when aged at 420 °C to promote the formation of SRO, which were absent in a quenched sample [317].

### 3.3.3. Short range diffusion models

Mechanisms which do not rely on long range atomic diffusion have gained support, particular in TWIP steels [21] and Al-Mg alloys [20], where serrations are present at room temperature.

In BCC iron, Snoek locking [320–322,227,314] refers to the stress induced ordering of interstitial solutes into interstices lying in particular orientations (Fig. 35), such that the asymmetric stress fields of the solute and dislocation overlap, named after Snoek's attribution of a room temperature Internal Friction peak to this [323]. Similar to in the case of a Cottrell atmosphere, energy must be provided to break the ordered atmosphere but unlike in the case of Cottrell atmospheres, diffusion distances necessary may be a single atomic hop. It is sometimes suggested that Snoek locking dominates at short (1 s) ageing times in mild steel [321,324]. Such a mechanism requires an asymmetric distortion of the lattice by the solute in order to lead to preferred orientational order (Fig. 35).
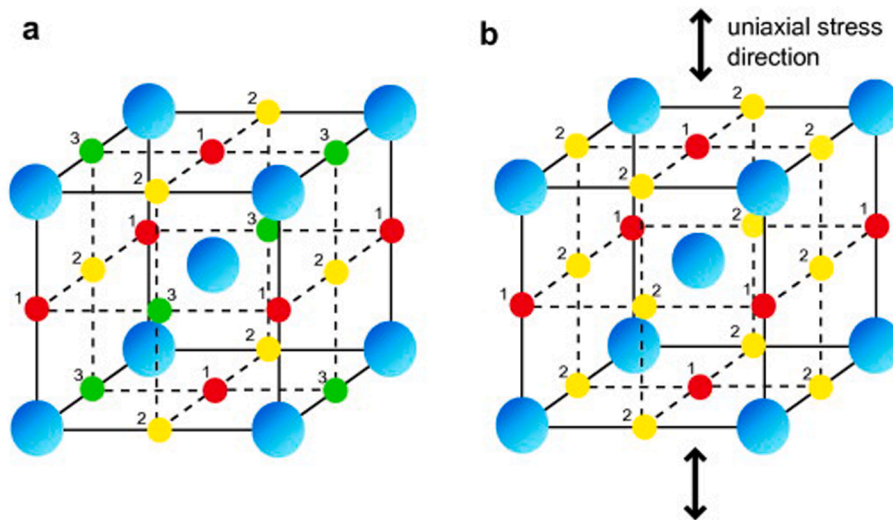
**Fig. 35.** Snoek locking in ferrite. (a) Distorted octahedral sites in ferrite. In the absence of a stress, sites 1 (red), 2 (yellow) and 3 (green) are equally energetically favourable. (b) Energetics of octahedral sites under the presence of a uniaxial stress. Sites 1 have their distorted axis parallel to the applied stress, thus are energetically favoured [326].
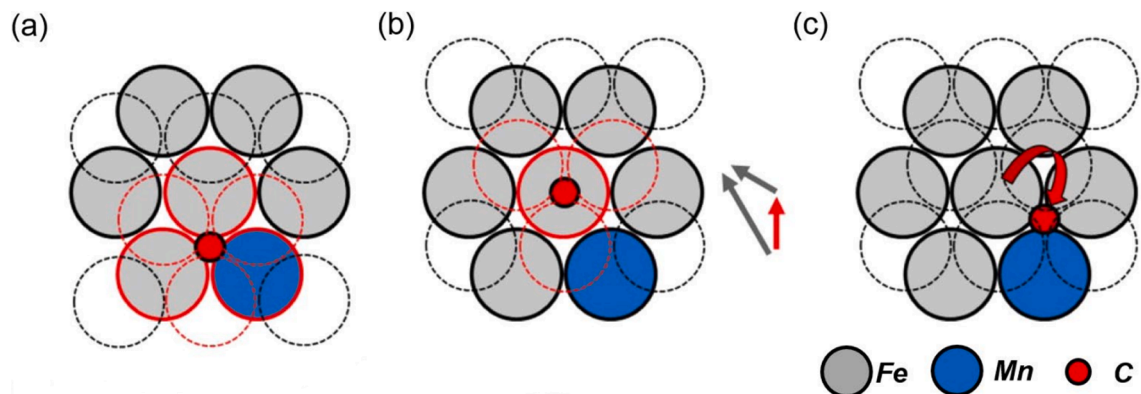


**Fig. 36.** Proposed mechanism of serrated yielding in TWIP steels. (a) Two {111} planes, where atoms in the top layer are indicated by dotted lines and C sits in an octahedral interstice between the two layers. (b) The passage of an a/6<112>{111} partial dislocation (red arrow) disrupts energetically favourable short range ordered Mn-C complexes and displaces the C into a high energy tetrahedral interstice. (c) C-Mn complexes relax by short range diffusion [21].

Conversely in FCC metals, the octahedral and tetrahedral sites are both regular. However, Rose and Glover proposed that a Snoek locking mechanism may still operate in FCC alloys, if there is a preference for short range ordered solute-interstitial or vacancy-interstitial pairs to form, for instance to offset the compressive strain field of the interstitial [320]. Then, this pair generates an asymmetric distortion hence may provide a locking force on dislocations [325,320,74]. Such an explanation for room temperature serrations in TWIP steels remains popular [24]. A second theory to explain room temperature serrations in TWIP steels [21,327] resembles the 'dynamic ordering' of short range ordered domains [300] discussed previously. It was proposed that C-Mn pairs which lie across the slip plane will be cut by a dislocation, leading to a disordering effect: this differs from the Snoek mechanism where pairs are reoriented rather than cut and need not lie in the slip plane. Then, the C-Mn pairs can reform through a single atomic jump (Fig. 36). One feature that this explanation does not immediately capture is that serrated flow in TWIP steels (and in superalloys [49]) is believed to depend on the SFE, with lower SFEs favouring serrated flow (Al [21,328,329] and Cu [330] raises the SFE in TWIP steels). It was further proposed that this mechanism will provide more resistance to the passage of partial dislocations, since a partial dislocation displaces the carbon atom from an octahedral to a tetrahedral interstice, leading to increased lattice distortion prior to reorientation (Fig. 36) [21]. Whereas conventional DSA requires the waiting time of a dislocation at an obstacle to be comparable to that for long range diffusion (Section 3.2), such mechanisms relating to Snoek locking and short range order cutting require only time for a single C atomic jump so may be expected at lower temperatures. As noted in several recent reviews, the short range order cutting mechanism is one of the most popular explanations for serrated flow in TWIP steels [331,229,332]. Neutron scattering in a TWIP steel may have indicated a reduction in nanodomain size in a sample taken after the passage of a localised band of deformation compared to
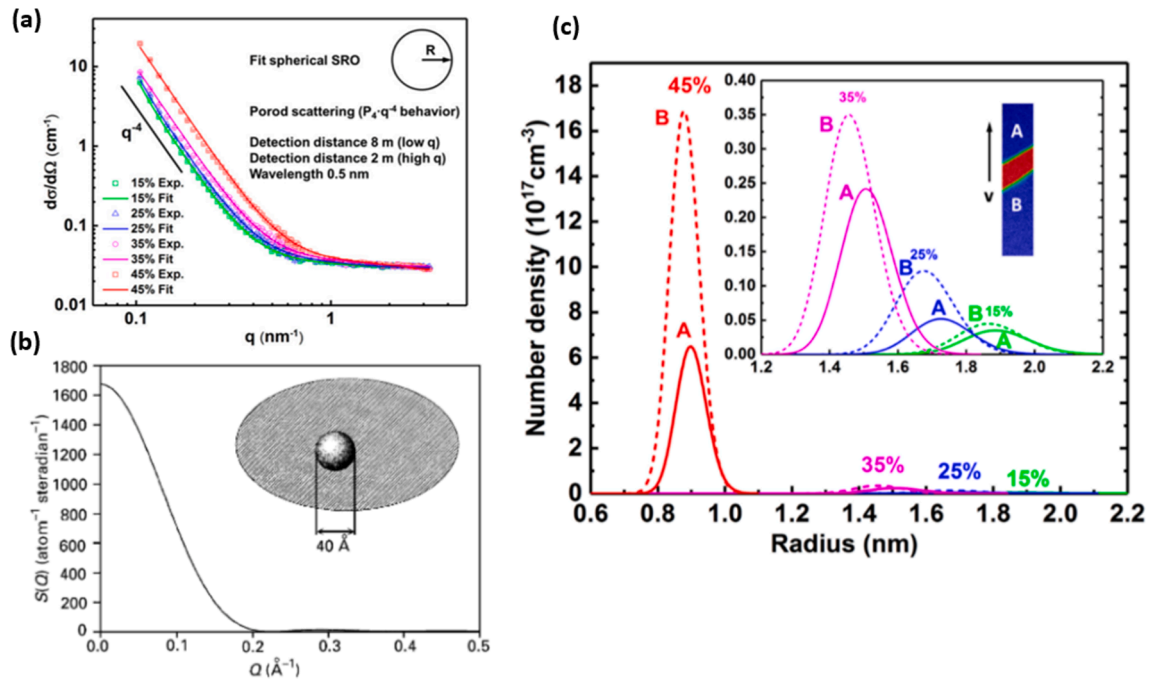
**Fig. 37.** (a) Differential cross section, $\frac{d\sigma}{d\Omega}$, versus magnitude of scattering vector, $q$, obtained through small angle neutron scattering of a TWIP steel specimen deformed at a strain rate of $10^{-3}$ s$^{-1}$ at room temperature, interrupted at indicated strains for diffraction measurements (duration 90 min) [173]. A disperse model for short range order [313] was assumed, thus the scattered signal was proposed to arise due to interference between scattered neutrons from disperse ordered Mn-C clusters with a different scattering length to the matrix. (b) Calculated structure factor S(Q) versus scattering vector length for a uniform density $5 \times 10^{-5}$ nm$^{-3}$ of spheres of radius 2 nm [335]. (c) Modelled distribution of disperse short range ordered zone radii based on fit to experimental data in (a) [173]. Measurements were made at two points, one ahead of a propagating localised band and the other behind the band, referred to as (A) and (B), respectively. It was suggested that smaller short range ordered zones develop over the course of a test as they are cut.

before, as illustrated in Fig. 37[6] [173,333]. However, some recent work on TWIP steels has taken an opposite view, that long range carbon diffusional locking is responsible for serrated flow. *Ab initio* calculations indicated that C-Mn complex reorientation was too slow in the bulk and too fast in a SF to cause serrations and APT taken from within a localised band appeared to indicate the presence of a carbon atmosphere, as shown in Fig. 38 [334].

A third model was proposed in Al-Mg alloys showing serrations at room temperature, representing a modification to the Cottrell mechanism [336,20,268]. It was proposed that a solute atmosphere develops at the dislocation core, due to the size difference between Al and Mg atoms, hence preference to lie in the tensile/compressive side of the dislocation core. However, rather than occurring through long range diffusion, it was proposed that the dislocation core strain field, neglected in the classic Cottrell mechanism, is significant in determining the solute-dislocation binding energies and activation energies for diffusion, thus the solute atmosphere predominantly develops through short range cross core diffusion. Further, based on transition rate theory it was shown that the concentration of solute above/below the core will evolve according to Eq. (10). It has been speculated that cross core diffusion operates in superalloys [9]. In Al-Mg, APT appeared to show Mg enrichment around a dislocation, but this was interpreted as developing through a short range cross core diffusion mechanism rather than the Cottrell mechanism [337].

### 3.3.4. Strain ageing and planar faults in order hardened alloys

Mechanisms resembling DSA and Cottrell atmosphere formation have been proposed in alloys which deform by the creation of an APB or SF, but where solute diffusion occurs to the planar fault rather than the dislocation core.

A simple theoretical framework to understand one possible mechanism for this in the case of APB shear was proposed [312]. Conventionally, APB shear occurs through the sweeping of a pair of coupled superpartial dislocations through the crystal. The lead superpartial generates an APB upon shearing, providing a hindering force to its motion, whereas the trailing partial cancels out the APB, providing an attractive force to its motion.

In steady state, the force balances on the lead and partial dislocations read [312] (see strong and weak coupling in [25])

---

[6] Though this result is perhaps surprising, given that measurements were performed *ex situ* and serrations are present at TWIP steels at room temperature, so it may be expected that the structure relaxes during handling. It is not clear that the approach taken would be able to identify all forms of short range order discussed in Section 3.3.2
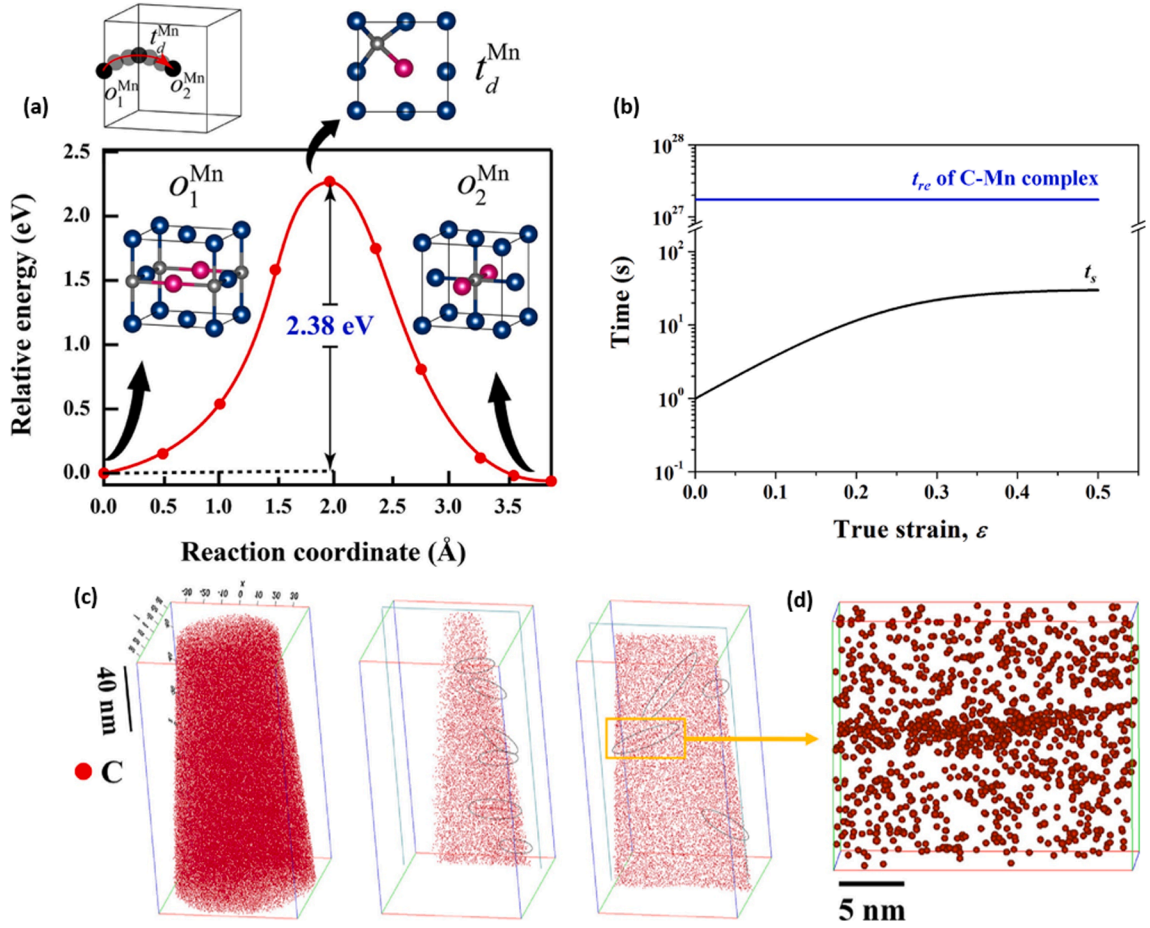
**Fig. 38.** (a) Density functional theory calculation of minimum energy path for C-Mn complex reorientation, based on the Nudged Elastic Band method. The initial, final and intermediate states are shown, with the carbon atom located in an octahedral, octahedral and tetrahedral site, respectively. Fe, Mn and C atoms are coloured blue, pink and gray, respectively [334]. (b) Time required for C-Mn reorientation, $t_{re}$, based on the activation energy calculated from (a) and corroborated against internal friction measurements, and time available for reorientation, $t_s$, between the passage of the lead and trailing partial dislocations, based on estimates of the SF width and dislocation velocity. It was suggested that reorientation is too slow to explain serrated flow [334]. Note the simulation does not include stresses from a dislocation. (c)(d) APT reconstruction of C atoms in an extracted needle from Fe-18Mn-0.55C (wt.%) steel specimen deformed at $10^{-4}$ s$^{-1}$ to 23.1 % strain, taken from within the localised deformation band. Linear features highlighted by black ellipses were proposed to show C segregation around dislocation cores, and were not present in the undeformed sample. Serrations were observed from $-20 \degree$ C – $50 \degree$ C [334].

$$\tau b l_1 + R l_1 - 2\gamma r_1 = 0 \tag{35}$$

and

$$\tau b l_2 - R l_2 + 2\gamma r_2 = 0, \tag{36}$$

where $\tau$ is the shear stress on the plane containing the lead and trailing dislocations, of line length $l_1$ and $l_2$, respectively. The lead and trailing dislocation pass through a length $r_1$ and $r_2$ of ordered precipitates, respectively, with APB energy $\gamma$, and exert a reaction force per unit length, $R$, on one another. Eliminating $R$ gives

$$\tau = \frac{\gamma}{b}\left(\frac{r_1}{l_1} - \frac{r_2}{l_2}\right). \tag{37}$$

If there were a mechanism for a time dependent reduction in the planar fault energy, which could operate in the time between a lead and trailing partial sweeping a point, then the attractive force on the trailing partial would be reduced, causing an increased stress necessary to move the pair [338–340,300], given by

$$\tau = \frac{1}{b}\left(\frac{\gamma r_1}{l_1} - \frac{\gamma' r_2}{l_2}\right), \tag{38}$$
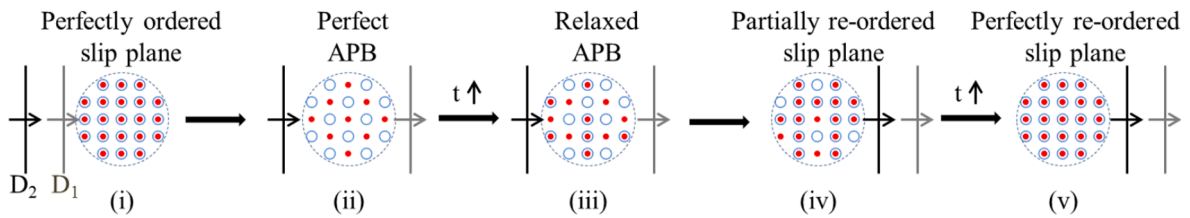
**Fig. 39.** Schematic locking mechanism in alloy with ordered precipitates. (i)(ii) The lead dislocation shears the ordered structure generating an APB. (iii) A lower energy configuration is reached prior to the sweeping of the trailing partial, in this case through short range atomic rearrangements. (iv) The trailing dislocation shears the relaxed APB, experiencing a raised stress as its passage no longer fully restores the ordered structure. (v) Subsequent short range diffusion fully restores the ordered structure [312].
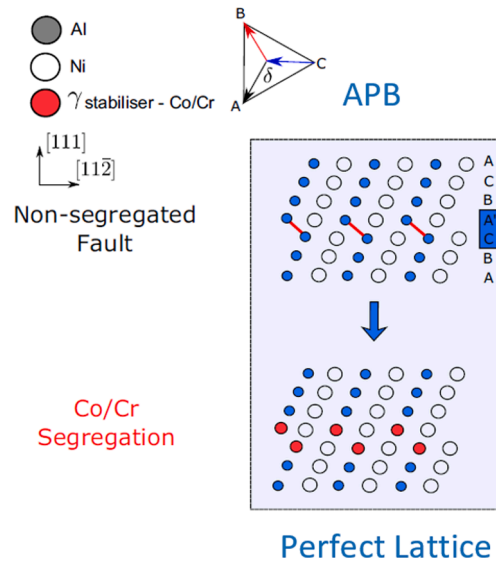


**Fig. 40.** Proposed mechanism for elemental segregation to the APB in single crystal superalloy MD-2 following creep testing at 800 °C [353].

where $\gamma' < \gamma$ is the new reduced APB energy just ahead of the trailing superpartial dislocation [312]. Slower strain rates would lead to more time between the sweeping of the lead and trailing partial for the relaxation of the planar fault, hence the possibility of a negative SRS [340,312].

Proposed mechanisms for the relaxation of the planar fault can be split in two categories: long range diffusion of solute to the fault or short range atomic shuffles [338,340,341]. Ovri proposed a short range diffusion mechanism where atomic swaps in the APB reduces the number of like bonds across the APB (Fig. 39) [312], though it is not clear that, in general, there will exist a pathway for this, at least when considering nearest neighbour interactions: for the example structure shown in Fig. 39, any single atomic swap to reduce the number of like bonds across the slip plane will create unlike bonds in other planes. In the case of SFs, Suzuki segregation, referring to the long range diffusion of solute atoms to lower the SFE [342], has been suggested to lead to a locking effect [314,343,344], and in the particular case of superalloys [345,95,51,184], as well as the conventional time independent effect on solution strengthening. Such mechanisms based on long range diffusion face the same issue as conventional DSA, in that it is not clear that substitutional elements have sufficient diffusivity at the temperatures where serrations occur. However, one difference is that the mechanisms above allow for a possible chemical element to the solute-planar fault interaction, potentially leading to stronger interactions and an increased drift velocity (Eq. 10). DSA to stabilise twin boundaries has also been suggested [346].

It is worth noting that long range diffusion to stabilise faults and short range shuffle mechanisms to produce a low energy fault plane are proposed to occur in the $\gamma'$ phase in superalloys during intermediate temperature creep. Transmission Electron Microscopy (TEM)- EDX demonstrated segregation of Co and Cr to the plane of a SESF and depletion of Ni and Al [347]. Similarly, isolated SISFs were found to be enriched in Co and W via APT [348,349] and EDX [350]. It was suggested that these observations relate to Suzuki segregation to the fault plane [349–352]. In the early stages of a dislocation ribbon (Section 2.1.1) mechanism in single crystal superalloys following creep, EDX [353] and APT [348] demonstrated an enrichment of Co and Cr in the APB plane. It was noted that these elements are $\gamma$ stabilisers, hence may segregate to reduce the APB energy (Fig. 40) [353]. However, in this context, this is usually proposed to be the mechanism controlling the rate of steady state deformation (which is strongly thermally activated in this range) rather than as a locking mechanism [3,354]. Care must be taken to understand the differences in role of segregation in creep and serrated yielding, if present at the slower strain rates and higher temperatures of creep deformation, the solute atmosphere is
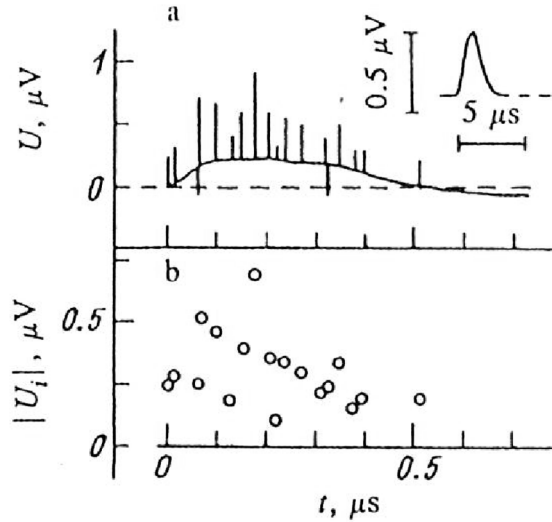
**Fig. 41.** Upper- EMF signal versus time spanning a single serration event in high purity Al single crystals loaded at 4.2 K. Lower- magnitude of EMF pulses with respect to time, plotted over the course of a serration event [69].

commonly believed to be dragged with the dislocation [347].

### 3.3.5. Thermomechanical instabilities

A separate class of instabilities has been proposed, due to positive feedback between localised heating from the conversion of mechanical work into heat and the resulting increased local deformation rate due to weakening if heat cannot be removed sufficiently quickly [68,301,203,355].

It was demonstrated that such an instability can similarly be considered as arising due to a negative SRS [301]. The heat conduction equation, assuming complete conversion of mechanical work to heat for a cylindrical test specimen of radius $r$ with little thermal gradient in the radial direction (on the basis that the Biot number is typically small [356,202]), heat capacity $C_v$, thermal conductivity $K_T$ and convective heat transfer coefficient $h_T$, reads

$$C_v \dot{T} = \frac{\partial}{\partial x}\left(K_T \frac{\partial T}{\partial x}\right) + \sigma \dot{\varepsilon} - \frac{2h_T}{r}(T - T_0), \tag{39}$$

when connected to a heat sink at temperature $T_0$, where $x$ is the axial direction. According to the negative SRS criterion, homogeneous flow is only stable until the SRS becomes negative [10]. Assuming stable flow (no temperature fluctuations in space or time), this has a steady state solution

$$T = T_0 + \frac{r}{2h_T}\sigma \dot{\varepsilon}. \tag{40}$$

Hence the increase in strain rate leads to a negative component to the SRS through the resulting temperature increase (Eq. (21)), until the limit of stability is reached.

Localised heating is typically considered important at cryogenic temperatures, since both the heat capacity and thermal conductivity tend to be lower, leading to larger temporal or spatial variations in the temperature [68,356]. Furthermore, a common feature in superalloys at the temperatures where serrated flow occurs is anomalous hardening: that is, the material becomes stronger with increasing temperature. Hence, it is not clear that such a feedback cycle would develop.

Whilst early models consider thermal fluctuations as trigger events for thermomechanical instabilities, experimental evidence confirms a role of cooperative dislocation phenomenon in triggering the instability [69]. Localised heating was observed in excess of 40 C during load drops in high purity Al single crystals loaded at 4.2 K, but an increased occurrence of correlated Electro Motive Force (EMF) pulses was also detected over a background due to thermoelectric effects from local heating, as shown in Fig. 41. These pulses were attributed to the drag of electrons during motion of isolated dislocation avalanches, with the statistics of individual slip events resembling self-organised criticality.

It was noted that a pulse precluded any localised heating response, though could only account for a fraction of the total strain accumulated during a load drop. Thus, it was supposed that the random thermal activation of a large dislocation avalanche would provide the trigger serrated flow, with thermal conduction and localised heating providing the spatial coupling for further plasticity [357,358].

### 3.3.6. Twinning

Deformation twinning refers to a cooperative shear mechanism for plasticity distinct from slip, such that the deformed region forms
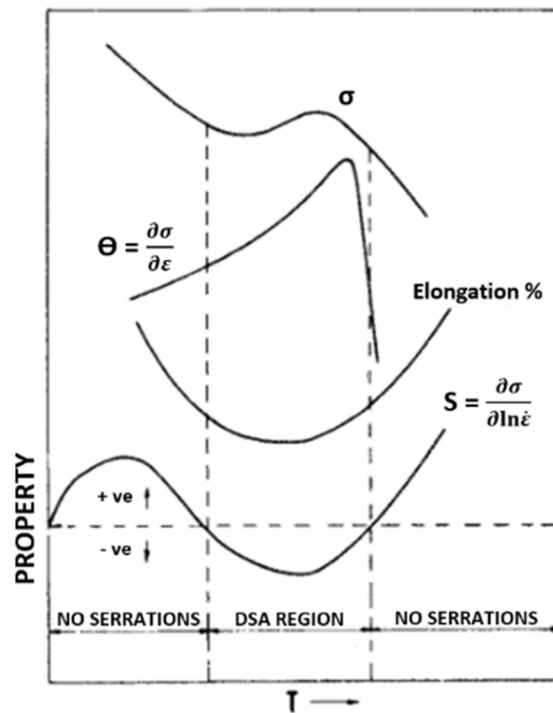
**Fig. 42.** Schematic plot of variation of various mechanical properties in the regime of serrated yielding [53]. $\sigma, \theta$ and $S$ refer to the yield stress, work hardening index, $\frac{\partial \sigma}{\partial \varepsilon}$, and SRS, respectively.
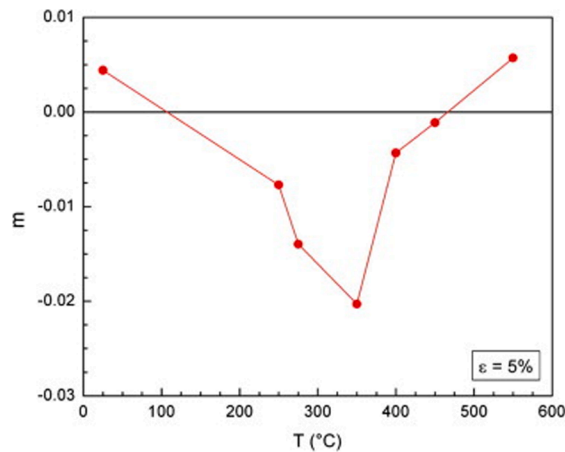


**Fig. 43.** Experimentally measured SRS, $m = \frac{\Delta \ln \sigma}{\Delta \ln \dot{\varepsilon}}$, for Udimet 720, based on comparison of flow stresses at 5 % strain for constant rate tensile tests at $10^{-4}$ s$^{-1}$ and $10^{-3}$ s$^{-1}$ [9].

an identical crystal structure, but in a different orientation, related by symmetry to the prior orientation [359,360]. Twinning is relatively uncommon in FCC metals except those with a low SFE and at low temperatures/high strain rates, and is often believed to start only after a strain has been reached due to work hardening [359].

Serrations have often been observed at cryogenic temperature and often in high purity single crystals [361–363], making DSA difficult to envisage, and attributed to deformation twinning [364,361–363]. However, there exist cases where twinning occurs without any serrations, for instance in the room temperature deformation of Cu-Zn, Co-Ni and Cu-Sn [365,359,366]. Some suggest that this can be rationalised because a load drop will only be observed if a lower stress is required for twin growth than for nucleation [367,368], thus serrations can be associated with sudden bursts of twinning. They suggest that the size of load drops associated with twinning increases with SFE, due to a greater nucleation stress (relative to the growth stress) [367,359]. Bolling considers twinning and martensitic transformations as leading to a negative SRS [369,370] but it is not clear that this is always the case during twinning:

**(a)**



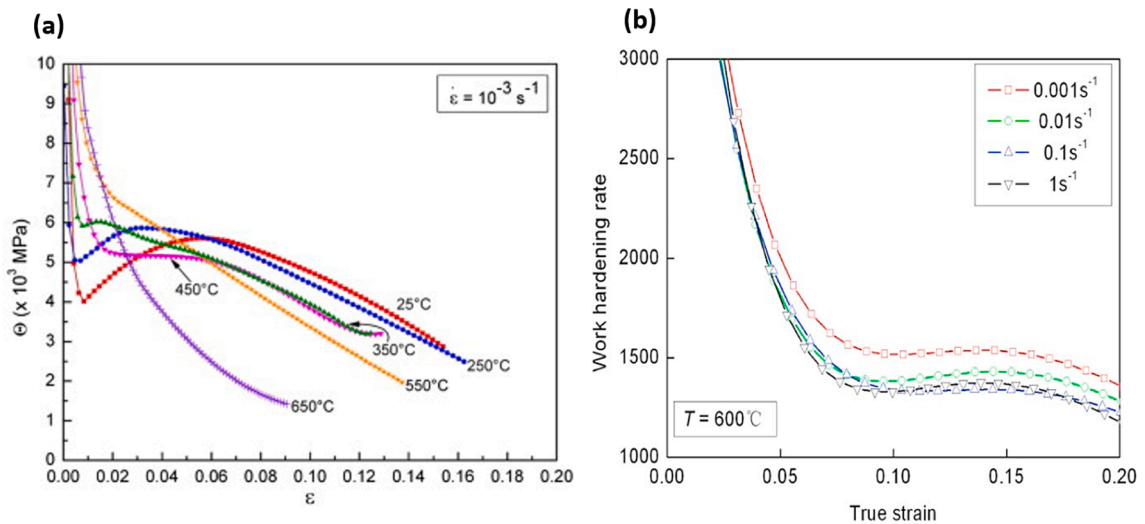**(b)**

Fig. 44. (a) Work hardening rate, $\Theta = \frac{\partial \sigma}{\partial \epsilon}$, versus strain and temperature for Udimet 720 LI tested at $10^{-3}$ s$^{-1}$ [9]. (b) Work hardening rate versus strain rate and strain for superalloy 800H deformed at 600 °C [251]. Note in both cases the stress–strain data was smoothed by fitting a low order polynomial prior to differentiation.

usually mechanical twinning is considered athermal.

As the relative contribution of conventional deformation twinning increases with decreasing temperature/strain rate [371], it is not clear what would cause a lower temperature bound for serrations caused by discontinuous twinning alone. In TWIP steels, DSA or short range solute mechanisms are typically believed to dominate room temperature serrations [21].

## 4. Effects on mechanical properties

Serrated flow has been associated with several effects on the mechanical properties (Fig. 42), namely: an increase in flow stress with temperature (anomalous hardening) and decreasing strain rate (negative SRS), a decrease in ductility and an increase in work hardening [53,18], consistent with current understanding of DSA [18,236]. However, conflicting results have been obtained in modern superalloys and it is not certain that DSA is solely responsible for serrated yielding. The following section reviews the effects of DSA on mechanical properties and corresponding observations in superalloys.

### 4.1. Strain rate softening and anomalous hardening

Regardless of the underlying mechanism, serrated flow is typically considered a consequence of strain rate softening [18,17,10,14] (Section 3.1). Extensive reports have demonstrated that the SRS shows a dip in the temperature and strain rate domain where serrated yielding occurs, usually to negative values, as shown in Fig. 43 [77,9,80,106,372,373] though in some cases remaining positive [250,92]. It is important to make a distinction between the experimentally measured and theoretical negative SRS: in theoretical calculations, the SRS represents the constitutive local material behaviour with strain rate, conversely in experiment, the SRS measured is based on measurements of the macroscopically averaged stress at different strain rates. It is expected that strain localisations accompany serrated flow (Section 2.4), thus the local and globally averaged strain rate differ.

While anomalous hardening (an increase or plateau in strength with temperature) is not a necessary feature for serrated flow, the two are commonly found to coincide [9,214,250,180,374]. This is predicted in the case of DSA since the negative SRS arises through a time dependent strengthening effect, where the time dependence derives from solute diffusion thus is also sensitive to temperature [236]. However, it is not clear that the anomalous yield strength in superalloys can be attributed solely to serrated flow [375]: typically this behaviour is attributed to Kear-Wilsdorf locking [26,376]. Sometimes a yield strength anomaly has been reported in solid solution superalloys, where Kear-Wilsdorf locking may not operate [372,377,214,378,379], but other explanations such as dynamic precipitation [375] may still account for this.

### 4.2. Work hardening

Serrated flow in mild steel is commonly linked to an increase in work hardening rate, as shown in Fig. 4 [60,380] and it is often assumed that this is a general feature which should accompany serrated flow in substitutional alloys such as superalloys [109,381,256,382–384].

It is worth noting that the DSA theory developed for substitutional alloys (Section 3.2) directly predicts an increase in work hardening, since higher strains imply a reduced mean dislocation velocity and an increased solute mobility through the vacancy

concentration, directly leading to a greater mean solute build-up around the dislocation cores with strain [236]. However, this is typically believed to be small [236].

The increase in work hardening rate accompanying DSA in mild steel is typically explained through an increased dislocation generation rate [14,380,236,9,60,385], on the basis that dislocations may become immobilised over time due to the formation of strong solute atmospheres, leading to the dislocation becoming effectively sessile [386,256]. A lower stress may be necessary to continue plastic deformation through the generation of new dislocations (with no solute atmosphere) than to propagate existing strongly locked dislocations [60,14,386,380,387,388][7].

It is less clear whether an increase in work hardening rate accompanies serrated flow in substitutional alloys [236]. Leslie noted an increase in work hardening associated with interstitial systems showing serrations only, and not substitutional systems [389]. The increased work hardening rate in TWIP steels is usually attributed to the TWIP effect [63]. Little influence on the work hardening was noted when DSA operated in some superalloys [9,91,381,81,384] and results in other superalloys are inconclusive [109], though some results do indicate an increase in the initial work hardening rate with temperature and decreasing strain rate over the regime of serrated flow, as shown in Fig. 44 [9,251]. Conversely, some have suggested that an increase in work hardening rate is only observed in the 'inverse' DSA regime in superalloys: it was suggested that 'inverse' DSA in superalloys relates to the Suzuki segregation of solute to SFs, thus leading to a reduced SFE, an increased fault width and hence reduced ease of cross slip [214]. As a final point, in some cases, the disappearance of serrated flow at high temperatures in superalloys appears to correlate with the point of geometric instability [214,22,91,390]. While this could suggest that serrated flow is associated with a mechanism of work hardening that is responsible for stabilising against necking, the opposite is considered equally likely. That is, the onset of geometric instability prevents further serrated flow since this marks the point where local geometric softening more than compensates for work hardening, so there is no longer a drive for strain localisation to propagate through the sample. Such band immobilisation during necking has been reported [158], as discussed in Section 4.3.

## 4.3. Ductility

In mild steels, the PLC effect appears to coincide with the occurrence of 'blue brittleness' (Fig. 46(a)) [8] and DSA is commonly suggested to be one mechanism of intermediate temperature embrittlement [53,18,8,391,63] (and in the specific case of superalloys [373,179,372,91]). However, it is important to note that several other effects may be responsible for any intermediate temperature embrittlement in superalloys [392], such as intergranular precipitation and grain boundary segregation.

At least two plausible effects of DSA on the ductility can be considered, with the most important effects depending on the failure mode. Firstly, due to the common reciprocal nature between yield stress and ductility: the additional strengthening reducing crack tip plasticity [393,227].

Secondly, in tensile specimens, a negative SRS may increase the tendency for necking, since resistance to necking is provided by local work hardening and strain rate hardening in the necked region [8,18]. Considère's criterion states that necking begins at the maximum load, $F$, such that

$$\mathrm{d}F = \sigma \mathrm{d}A + A\mathrm{d}\sigma = 0, \tag{41}$$

where $A$ is the specimen cross sectional area [200]. Applying a constitutive relation of the form

$$\mathrm{d}\sigma = h\mathrm{d}\varepsilon + s\mathrm{d}\dot{\varepsilon}, \tag{42}$$

where $s = \left(\frac{\partial \sigma}{\partial \dot{\varepsilon}}\right)_\varepsilon$ closely relates to the SRS and is negative during serrated flow, Hart showed that necking occurs when [7]

$$h + s\dot{\varepsilon} < \sigma. \tag{43}$$

In the absence of a rate sensitive term, this matches Considère's criterion [200]. It can be seen that a negative SRS leads to the criterion for necking being fulfilled sooner, since this implies a reduction in strength in the faster deforming neck region [8,394]. Experimental evidence may challenge this, with conflicting reports as to whether necking begins close to [158], or prior to [395], fulfillment of Considère's criterion in its classical form, even within the same alloy system. Such a mechanism for ductility decrease relies on necking being a cause of failure: thus there may be questions regarding how general the observance of a ductility dip associated with serrated flow is [396].

Nonetheless, a close relation has been observed between necking and localised band propagation in several alloys. Localised bands were observed to continue to propagate even past the Ultimate Tensile Stress (UTS) concurrent to the formation of a neck, retaining similar spatiotemporal propagation characteristics. However, necking proceeded through the progressive immobilisation of the final localised band into a progressively narrower region around the intensifying neck, demonstrated in Fig. 45 [158,160]. It has also been suggested that detrimental effects to the ductility [8] in the DSA regime may originate from accelerated localised damage and internal cracking, for instance through a resulting greater tendency for strain localisation on the micro-scale to accompany serrated flow, forming stress-concentrating planar slip bands [8,97,397], though developed mechanisms for this are less clear. It was suggested that a

---

[7] It is not clear that this argument is quantitatively captured in the framework for DSA present in Section 3.2. In this respect, incorporation of ideas from the Ananthakrishna [234,259] model, to describe how DSA alters the rates of generation of mobile/immobile dislocations, seems necessary.
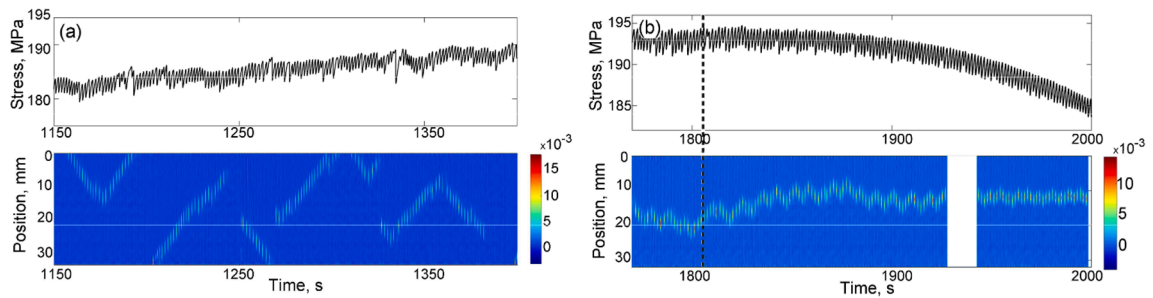
**Fig. 45.** DIC series plotting strain along a central line parallel to the tensile axis as a function of position along the line (ordinate) and time (abscissa), for a binary Al-3 Mg alloy tested at room temperature and $1.43 \times 10^{-4}$ s$^{-1}$, showing Type B band propagation. Corresponding stress–time plots are shown for a time increment a) far from necking b) close to the UTS, dotted line [158]. Continued Type B band propagation is observed past the UTS, progressively constrained to the position of neck formation.
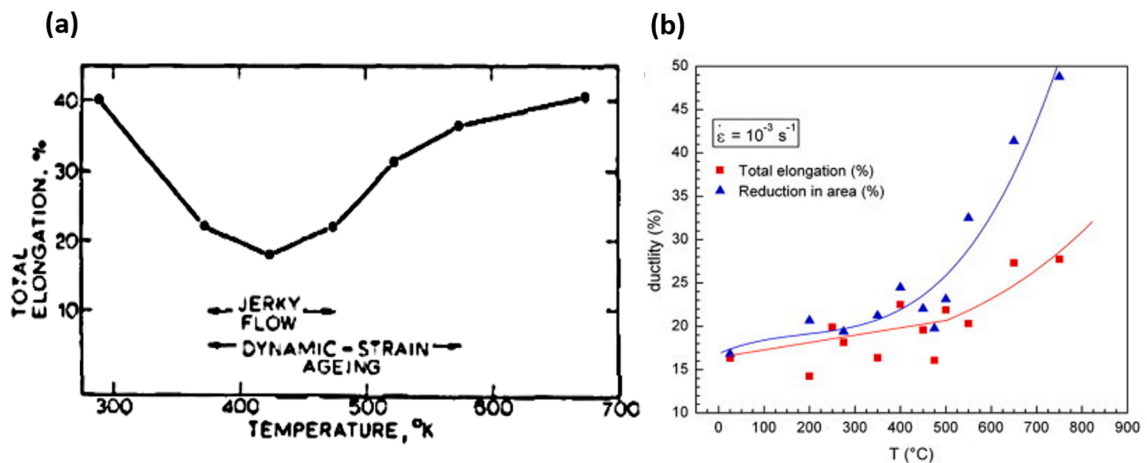


**Fig. 46.** (a) Elongation at failure versus test temperature for mild steel, deformed at $1.33 \times 10^{-4}$ s$^{-1}$ [8]. (b) Elongation to failure and reduction in area versus test temperature for superalloy Udimet 720 LI, deformed at $10^{-3}$ s$^{-1}$ [9].

change in toughness will arise due to a change in plastic dissipation associated with crack tip blunting during loading of notched specimens, since a high plastic strain rate is only possible at the crack tip when the localised band contains the crack [397,398], though this approach does not consider whether the change in stress state around a crack tip or neck may alter the strain localisation behaviour [399], as discussed above, nor the comparative time scales for a critical crack to develop and band propagation in un-notched specimens.

However, in other cases no clear effect on ductility (Fig. 46(b)) [180,393,376,9,117] has been noted in the DSA regime in superalloys. In some cases a ductility dip is observed at intermediate temperatures, though it is not clear that the temperatures match those where serrated flow is present [372,376,98,381]. These results are not necessarily contradictory, but rather may reflect the need for both a reduced SRS and deformation conditions favouring substantial necking before fracture to observe a ductility dip. An apparent beneficial effect of DSA on the fracture properties of IN718 was noted, where the disappearance of serrated yielding coincided with a transition from ductile to intergranular brittle fracture [67,94,179], possibly as solute segregation to dislocations prevented grain boundary sensitisation [67]. It is not clear that effects on the ductility in superalloys can be solely attributed to DSA.

## 4.4. Fatigue

Reviews of the effects of serrated flow in fatigue of superalloys and austenitic stainless steels from the 1990's can be found in Refs. [383,400]. Relatively little new advancements have been reported since. Perhaps analogous to the increase in work hardening in monotonic tension, the most apparent effect of serrated flow in cyclic loading is an increase in cyclic hardening rate [401,402,383,403–408], manifesting as a peak in the maximum stress amplitude versus temperature or strain rate when tested under strain control, or a dip in the plastic strain amplitude when tested under stress control [403], as shown in Fig. 47.

How the fatigue life is impacted is less clear. In several cases a dip in fatigue life under strain controlled loading has been reported around the temperatures where DSA operates [402,403], attributed in part to the increased stress amplitude [401,383,403,409,65]. Additionally, TEM investigations have demonstrated a reduced tendency for dislocation cell formation [405,402,383,403,409,410,65]
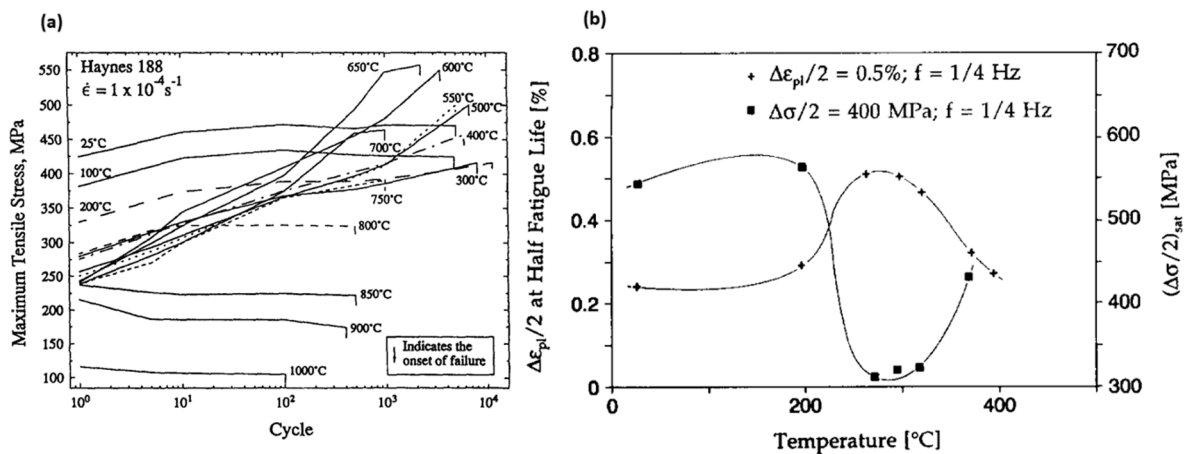
**Fig. 47.** (a) Maximum tensile stress attained in a cycle versus cycle number for superalloy Haynes 188, for a 0.8 % amplitude strain triangular waveform. Serrations were observed on the hysteresis loops from 400 °C – 650 °C [404]. (b) Plastic strain amplitude, $\Delta\varepsilon_{pl}$, at half-fatigue life and maximum stress amplitude, $\Delta\sigma_{sat}$ versus temperature for a low carbon steel loaded cyclically under stress control and strain control, respectively [403].

**Table 5**
Effects of increasing gauge length and specimen thickness on serrated flow.

| Parameter | Increase Gauge Length | Increase Diameter/Thickness |
|---|---|---|
| Strain between serrations, $\Delta\varepsilon_b$ | No effect [143,112] | No effect [143,163,164] |
| Band velocity, $c$ | No effect [141] | No effect [141,163] |
| Band width, $w$ | No effect [143,141] | Increases [141,144,103,163,145,164] |
| Strain rate in band, $\dot{\varepsilon}_b$ | | Decreases [141] |
| Serration amplitude, $\Delta\sigma$ | Increases [143] | Decreases [143,412,413,145] |
| Critical strain, $\varepsilon_c$ | No effect [143] | No effect [143] |

and possibly increased tendency for planar slip over the temperature range where serrated flow occurs, for instance forming localised planar slip bands [402,409,410,383,404,408,65,406,407]. This was suggested in part to arise through the suppression of cross slip due to reduction in SFE through a Suzuki segregation mechanism of locking [404]. Possible detrimental effects on fatigue life have also been attributed to easier fatigue crack initiation resulting from the impingement of localised slip bands, encouraged by DSA, on grain boundaries [401,383,410,97,65]. Similar increases in cyclic hardening and reduction in fatigue life are well known in mild steel [411]. Conversely under stress controlled loading, an increase in fatigue life has been found, attributed to the reduced plastic strain accumulation [403]. However, it is difficult to separate the effects of DSA from other temperature/rate dependent effects such as creep and oxidation and hence in some cases it is difficult to assess if a dip in fatigue life can be solely attributed to serrated flow [401,409,93,383,410,65,97,408]. Tests performed under vacuum on an austenitic stainless steel still exhibited a reduction in fatigue life around the temperatures where serrated flow occurs [405].

## 5. Factors affecting serrated flow

The focus up to now has largely been placed on the effect of temperature, strain rate and strain on features of serrated flow such as the critical strain and serration amplitude (Section 2). The following section reviews effects of composition, microstructure and testing procedures on serrated flow.

### 5.1. Specimen design

With limited models able to predict the PLC band characteristics, understanding effects of specimen geometry is largely empirical. The results for Type A serrations are summarised in Table 5 below, though there is no evidence that superalloys in particular follow these trends.

The greatest consensus is that with increasing aspect ratio, the strain becomes more localised (band covers a smaller fraction of the gauge length) and correspondingly the serration amplitude increases.

While not widely investigated, a sensitivity of serrated flow to surface condition has been observed [414,309,415,264,247], as shown in Fig. 48. Similar stress–strain behaviour was observed in different samples of Al-Mg but for the presence of additional smaller serrations in the case of a coarser surface finish [309,414,264,247], with a relatively temperature insensitive amplitude [415]. However, the small serrations, suppressed on mechanical polishing, reappeared following chemical polishing or annealing [264,247],
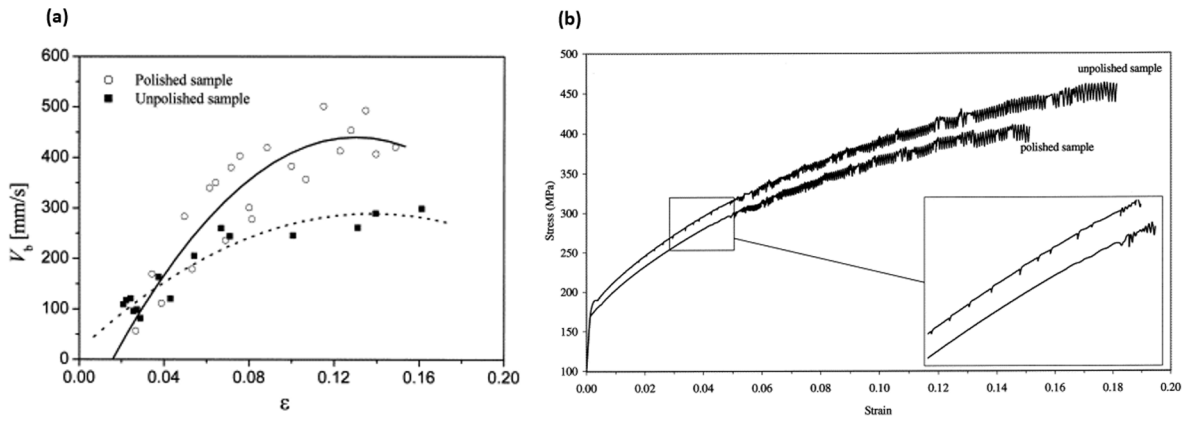
**Fig. 48.** (a) Band velocities versus strain for annealed Al-Mg alloy 5182, tested at 0 °C and 0.1 MPas$^{-1}$ [414]. The polished and unpolished samples had a surface roughness of approximately 30 $\mu$m and 100 $\mu$m, respectively. (b) Stress–strain curves for aged aluminium alloy 7475 obtained at room temperature [309].
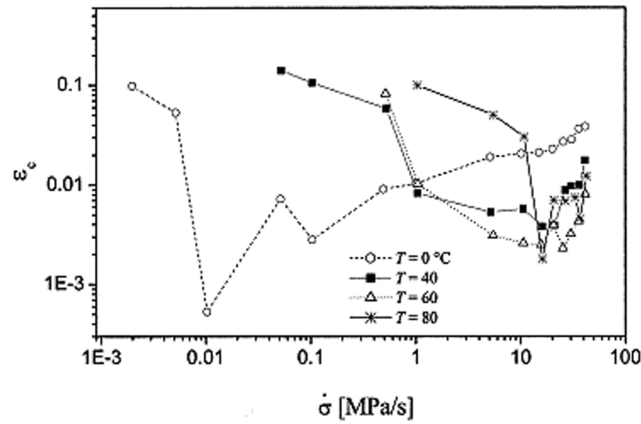


**Fig. 49.** Stress rate and temperature dependence of the critical strain for the onset of serrations in annealed Al-Mg alloy 5182 [414].

casting doubt over whether the effect can be explained solely by considering the surface roughness. A precise investigation of the role of the surface structure warrants further investigation in wider ranges of alloys, but it has been suggested that the small serrations observed relate to the possibility of weak synchronisation of avalanches in local stress inhomogeneities [247], for instance due to surface stress concentrators [414,309,415], before conditions allow for more widespread synchronisation. Thus, the atypical temperature insensitivity could be a consquence of a limitation of the scale of synchronised burst events to the scale of stress inhomogeneities. Faster band propagation was also reported in polished specimens [414].

### 5.2. Testing machine/procedure

The most apparent effect of the test machine is that due to the machine stiffness. Following Hall [314], consider a tensile test system intentionally softened through a spring of constant $K_L$ in series to the specimen of length $L$ under load $F$, such that the change in total extension, $x_{tot}$, between two instances in time, of the system is

$$\delta x_{tot} = \frac{\delta F}{K_L} + \delta L. \tag{44}$$

The change in specimen length can be split into two components. Serrations are associated with macroscopic bursts of plastic strain, such that the extension of the specimen increases approximately instantaneously by $\delta L_p$. Subsequent load redistribution will occur between the spring and specimen, leading to a further length change of the specimen, $\delta L_r$, given by

$$\delta L_r = \frac{dL}{dF} \delta F, \tag{45}$$

assumed to be well defined between strain bursts. Assuming both the strain burst and subsequent load redistribution occur rapidly and
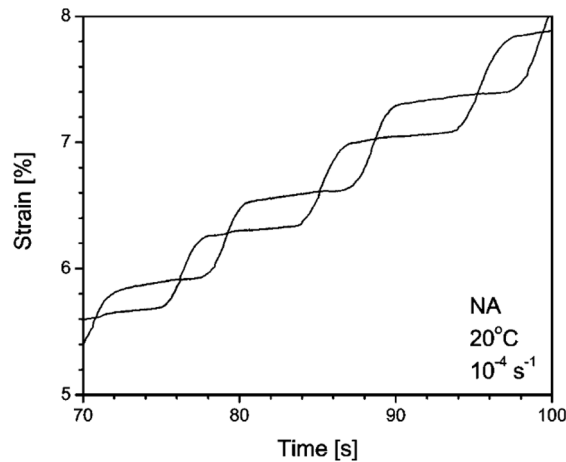
**Fig. 50.** Strain signal recorded by two extensometers in different positions along gauge length for Type A serrated flow in Al-Zn-Mg [415].
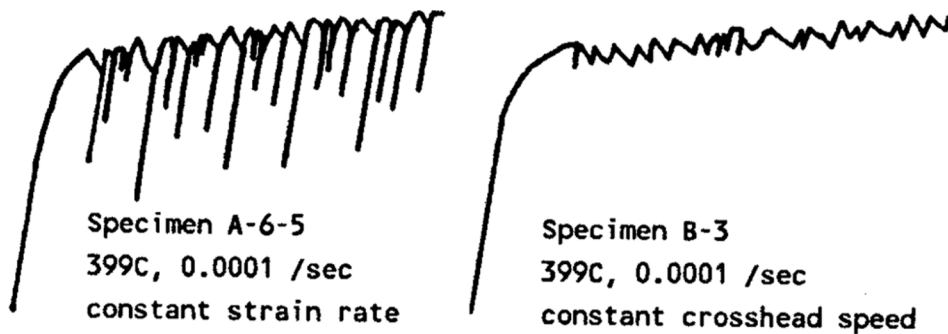


**Fig. 51.** Schematic stress (ordinate) - strain (abscissa) curves for superalloy René 88DT under crosshead displacement control and extensometer measured strain control. [93].

hence applying the condition

$$\delta x_{tot} = 0 \tag{46}$$

to Eq. (44) leads to a relationship between the resulting extension of the specimen and load change, $\delta F$, of the form

$$\delta F = -\frac{\delta L_p}{\frac{1}{K_L} + \frac{dL}{dF}}. \tag{47}$$

It is apparent that under load control ($K_L$ small), $\delta F$ is small and thus the plastic strain burst manifests as a sudden burst in extension [167,175], whereas under strain control ($K_L$ large) a larger load drop is observed [53]. For a finite machine stiffness, both a combination of a load drop and strain burst will be seen [279].

Similar 'normal' and 'inverse' trends in the critical stress for the onset of serrations were seen in an Al alloy in load control (Fig. 49) [414,416] to those in strain control (for example in Fig. 5). However, the serrations had a staircase appearance resembling Type D at all temperatures and stress rates, rather than showing Types A/B/C like in strain control [414,175,416,417]. Furthermore, localised bands formed under stress control demonstrated different propagation characteristics to those formed under strain control (for example in Fig. 12), propagating either partially or fully across the gauge length, but with a higher velocity compared to strain control [162,167,417,418] and with bands not observed during loading periods between strain bursts [417]. More significantly, propagating bands were still observed under conditions leading to Type B or C behaviour under strain control [167]. FE simulations have reproduced similar behaviour using methods discussed in Section 3.2.3, when the machine equation (Eq. (7)) is modified to account for the different control mode [419], following as propagation of the instability is not interrupted by unloading [162,417,419]. Limited studies have shown an increase in the accumulated strain increment on band propagation, $\Delta\varepsilon_b$, with strain, as reported under strain control in Section 2.4 [175,416], while differing trends have been observed on the effect on band velocity with loading rate: either increasing [141,419] or decreasing [420,419] with stress rate. Second, the extensometer measured strain differs in behaviour from the crosshead measured displacement [112,141], sensitive to the positioning [415,389] and length [421] of the extensometer. This should be expected since the strain measured from the crosshead displacement is averaged over the whole sample (and test fixtures) whereas
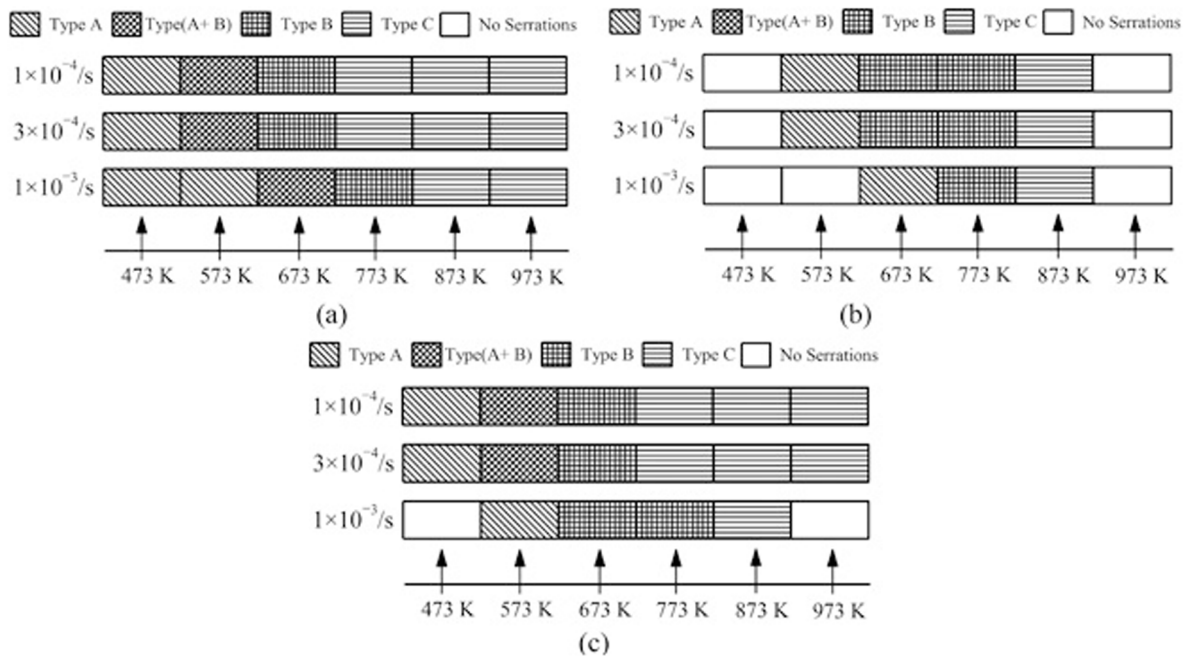
**Fig. 52.** Plots of the strain rate (ordinate)/temperature (abscissa) domain for different serration Types for superalloy IN718, when (a) solution treated at 1040 °C and air cooled (b)(c) subsequently aged at (b) 720 °C/8 h then 620 °C/8 h to form $\gamma'$ and $\gamma'\prime$ (c) 900 °C/24 h to form $\delta$. [80].

the extensometer measured strain is only averaged over the separation of the extensometer legs, typically less than the gauge length, hence more sensitive to strain localisation accompanying serrated flow. Fig. 50 shows the strain measured by two extensometers fixed to different positions along the gauge length during Type A serrations. Both accumulate the same average strain, presumably as a localised band of deformation passes through, but the band passes between each extensometer at different times. It has been noted, in cases, that stress–strain curves resembling Type A or Type D (staircase) behaviour can be generated by plotting the global or local strains, respectively [415,87,112], rather than based on a genuine difference in material properties. This does not account for the observation of rounded Type D (Type A2) serrations, for instance observed in [103–105]. Further differences have been reported in serration appearance depending on whether using crosshead displacement control or extensometer measured strain control, with larger serrations appearing in strain control and differing in appearance from the common Types A, B and C (Fig. 51) [93,250,422]. These were interpreted as an artefact of the machine's slower response to a sudden strain burst in strain control [93]. 'Serrations' were observed in several Al-alloys under strain control which disappeared following auto tuning of the strain Proportional-Integral-l–Differential (PID) channel, which were interpreted as due to DSA [423], though their appearance closely resembled limit cycles which may arise due to an instability in the strain control, rather than due to a material property [424]. The extent to which the machine control affects the appearance of serrations needs clarification.

### 5.3. Precipitate distribution

Studies comparing serrated flow in superalloys in various metallurgical conditions, such as aged for peak strength or solution treated and quenched, show a clear role of microstructure [80,425,79,82,110,426,427,180,428]. While comparison of commercial grades only permits a qualitative analysis, a couple of points arise. The general characteristics of serrated flow appear the same regardless of microstructure, for instance: serration Types A, B and C can be observed [80,425,79,426,180]; 'normal' and 'inverse' DSA can occur [80,82,426,180] and the calculated values of the parameters $Q$ and $m + \beta$ appear comparable [80,79,82,110,426,180,123]. Weaver and Hale observed no serrations in overaged IN718 [110], though others have[429]. However, differences are seen, for instance in the critical strains, serration Types (Fig. 52) and amplitudes for a given set of deformation conditions [80,79,82,110,426], and in the range of temperatures over which serrations occur: often the widest domain is observed in the solution treated condition, as shown in Fig. 52 [80,79,82,426]. Thus, the role of precipitates appears to be a secondary effect in superalloys, in the sense that they may alter the characteristics of serrations but do not appear to directly cause serrations. A systematic picture of the effects of precipitate distribution is less clear. The critical strain has been shown to decrease [243,90,430,80] or increase [110,50] in different cases when aged compared to in the solution treated condition. In $\delta$ forming alloys such as IN718, the effect on the critical strain appeared larger when aged for high strength (forming coherent $\gamma'$ and $\gamma'\prime$) compared to when aged to form $\delta$ [80]. Several note the possible conflicting effects of the precipitates on serrated flow: solute depletion and prevention of dislocation avalanches may diminish serrated yielding, but precipitates may also act as barriers to gliding dislocations, allowing time for solute to diffuse to temporarily arrested dislocations and enhancing serrated yielding [243,431].
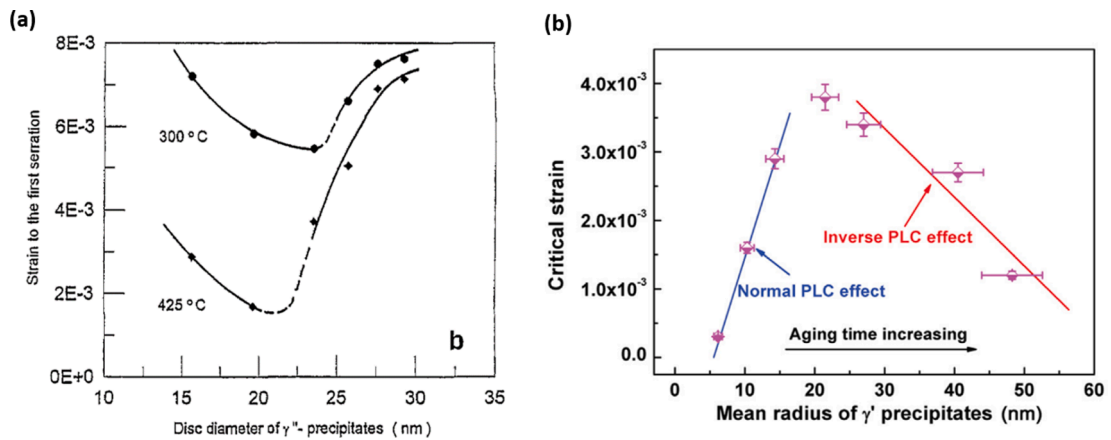
**Fig. 53.** (a) Critical strain versus $\gamma''$ precipitate radius (ageing time) for IN718, aged at 725 °C for up to 240 h and tested at $3 \times 10^{-3}$ s$^{-1}$ and the indicated temperatures [429]. (b) Critical strain versus $\gamma'$ precipitate radius for Nimonic 263, first aged at 800 °C for up to 500 h, then tested at 500 °C and $4 \times 10^{-4}$ s$^{-1}$ [108].
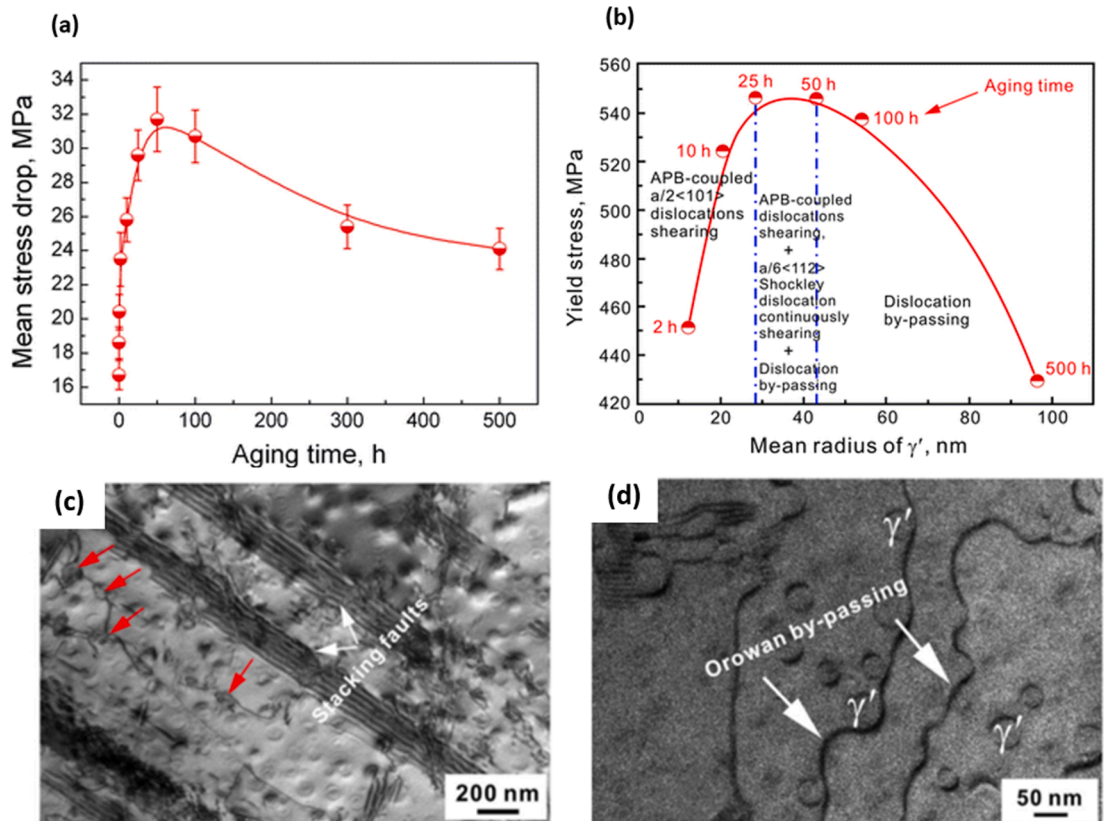


**Fig. 54.** (a) Stress drop magnitude versus precipitate ageing time for $\gamma'$ strengthened Nimonic 263 at 500 °C. (b) Yield stress versus ageing time. (c) (d) Example TEM micrographs taken subsequent to deformation for the specimen aged for 50 h [50].

Classical models for 'normal' DSA have been adapted to account for the latter effect of the precipitate distribution. The arrest time of dislocations at precipitates, assumed to be the main obstacle to dislocation motion, increases with increased precipitate spacing (Eq. (17)), allowing more time for solute diffusion [15] and hence in a limited domain, the critical strain decreased with increased ageing time [90,430] or reduced precipitate fraction [430].

However, more recent studies have found that this does not fully account for observations. A major assumption in the above analysis is that precipitates are the main obstacle, such that the time which dislocations spend not arrested at a precipitate is negligible
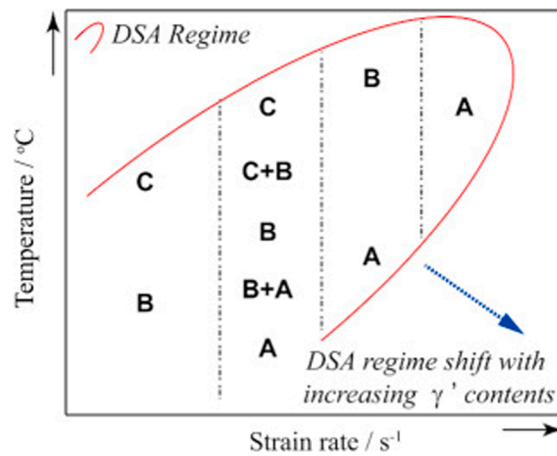
**Fig. 55.** Effect of $\gamma'$ fraction on the domain of serrated flow. [123].
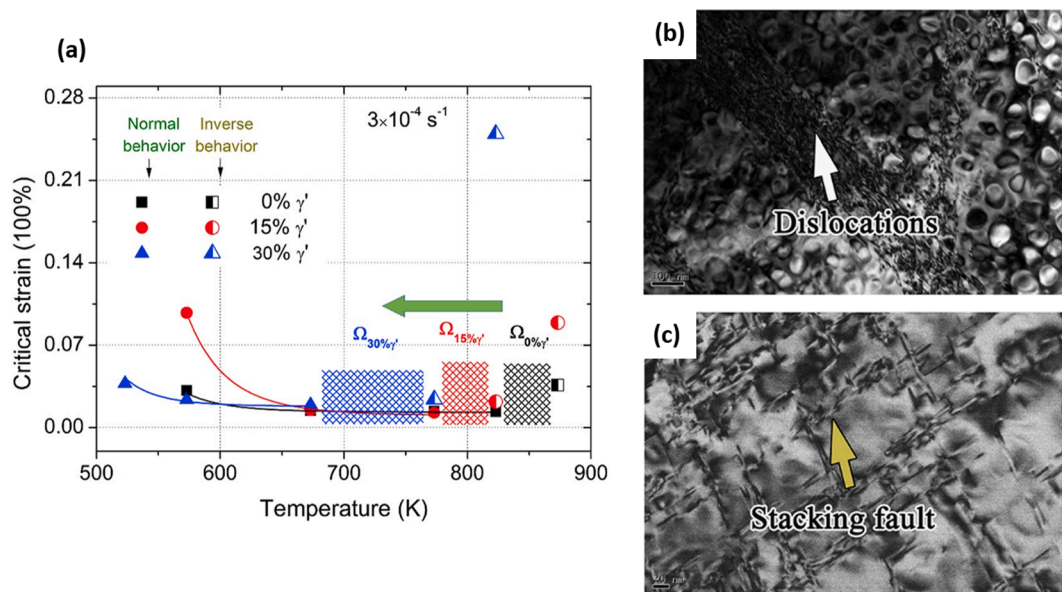


**Fig. 56.** (a) Critical strain versus temperature for several experimental nickel-base superalloys which lay on a tie line on the $\gamma$-$\gamma'$ phase field such that the indicated $\gamma'$ volume fractions are obtained, tested at $3 \times 10^{-4}$ s$^{-1}$ [184]. The hatched regions indicate the approximate 'normal'-'inverse' transition temperature for each alloy. (b)(c) TEM micrographs taken from 30 % volume fraction alloy subsequent to tensile testing at (b) 300 °C and $3 \times 10^{-4}$ s$^{-1}$ ('normal') (c) 500 ° C and $3 \times 10^{-4}$ s$^{-1}$ ('inverse') [184].

[15]. It may be expected that this becomes a better approximation as the proportion of strengthening arising from precipitate hardening increases [429]. In IN718, aged at 725 °C, a minimum critical strain was observed with precipitate ageing time at test temperatures of 300 °C and 425 °C, matching the proposed behaviour below a critical ageing time only (Fig. 53(a)) [429]. This minimum was found to occur close to the optimal precipitate ageing time for strength. It was proposed that the change in trend relates to the change in deformation mode to Orowan bowing: hence beyond the peak stress the arrest time of dislocations at the precipitates decreases. Similar conclusions were drawn in aged Nimonic 263, tested at 500 °C, with the stress drop magnitude showing a maximum close to the peak precipitate strengthening (Fig. 54), though in this case the critical strain showed a maximum with ageing time, rather than a minimum (Fig. 53(b)) [50,108]. The cause of this discrepancy is not clear[8].

It is not clear how to separate the effects of precipitate size and spacing, both of which increase during coarsening. To investigate

---

[8] One hypothesis might relate the difference to the chosen deformation conditions, and whether they lie in the 'normal' or 'inverse' domain. A single temperature/strain rate combination was used in both cases [429,108]. A reversal in the effects of ageing on the critical strain was noted in an aged Al-Mg alloy tested at different temperatures [432].

**Table 6**
Effects of increasing precipitate radius, fraction or spacing on serrated flow.

| Ref. | Varied Parameter | Fixed Parameter | Effects |
|------|------------------|-----------------|---------|
| [50,108] | Precipitate radius (heat treatment duration) | Precipitate fraction | Critical strain and serration amplitude increase to a maximum |
| [90,430] | Precipitate radius (heat treatment duration) | Precipitate fraction | Critical strain decreases |
| [429] | Precipitate radius (heat treatment duration) | Precipitate fraction | Critical strain decreases to a minimum |
| [430] | Precipitate fraction | Precipitate radius (fixed heat treatment) | Critical strain decreases |
| [123,184] | Precipitate fraction | None (fixed heat treatment) | Domain shifts to lower temperatures (critical strain increases in 'inverse') |
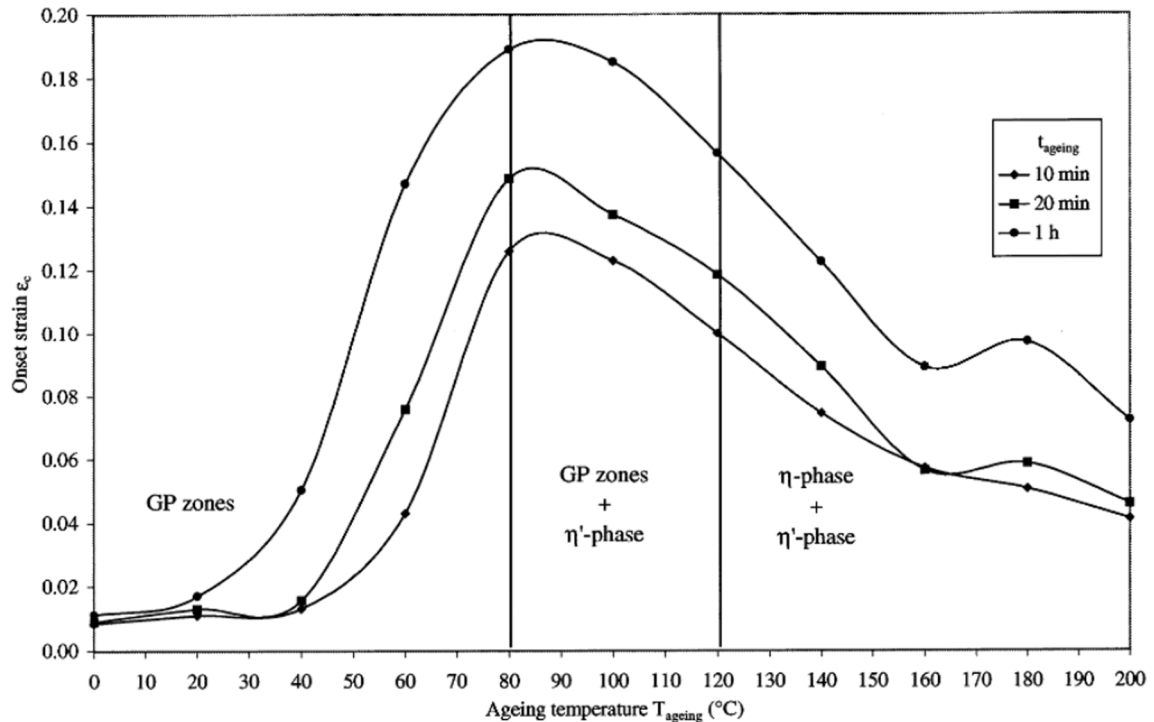


**Fig. 57.** Critical strain versus ageing time and temperature for type 7475 Al-Zn-Mg-Cu alloy, tested at room temperature and $10^{-3}$ s$^{-1}$ [309].

the effect of $\gamma'$ fraction, a series of alloys were designed which lay along a tie line between the $\gamma$ and $\gamma'$ phase fields, such that the compositions of the matrix and precipitate phases were constant but their relative proportions vary. With increasing precipitate fraction, the regime of serrated flow shifted to lower temperatures and higher strain rates (Fig. 55) [123]. The precipitate distribution has also been found to affect the transition from 'normal' to 'inverse' DSA, occurring at lower temperatures in higher fraction alloys (Fig. 56(a)) [123,184]. In addition, the transition temperature to 'inverse' DSA [429] and from serration Type B to Type C [108] reduced with increasing ageing time. In some superalloys TEM studies indicated that the transition to 'inverse' DSA with precipitate fraction was accompanied by a change in deformation mode from paired dislocation glide to SF shear (Fig. 56(b) and (c)) [123,184]: a greater precipitate fraction often favours SF shear over APB shear [42,45]. Some recent work in superalloys suggests that the transition from 'normal' to 'inverse' DSA is sensitive to the operative deformation mechanism, with SF shear a common signature of 'inverse' DSA in superalloys, thus by extension sensitive to the precipitate distribution [123,184]. It was further suggested that the critical strain is sensitive to the precipitate morphology, with cubic morphologies leading to 'inverse' behaviour at lower temperatures than spherical, believed to be related to their relative barrier strengths or ease of dislocation dissociation [433]. However, the heat treatments also led to a larger precipitate size for the cubic morphology.

In practice, the situation is complicated further in subsolvus heat treated superalloys by a multimodal precipitate distribution. It was proposed that the tertiary $\gamma'$ was likely to be the most important factor in DSA as it is the most frequently met obstacle [434]. Hence the increase in critical strain with tertiary $\gamma'$ fraction at 400 °C in TMW-2 superalloy was explained due to the finer barrier spacing, as expected classically, though the grain size and fraction of primary and secondary $\gamma'$ also varied substantially as a consequence of the necessary heat treatments.
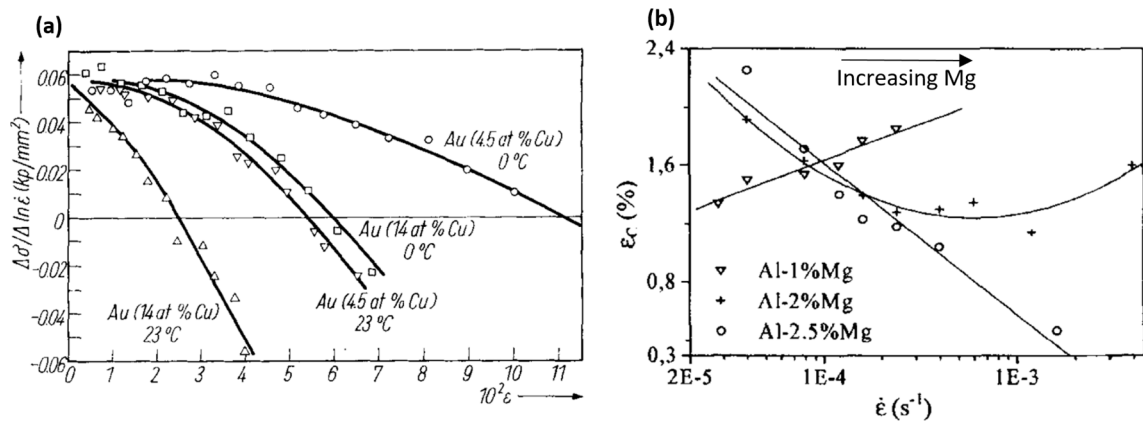
**Fig. 58.** (a) SRS, $\frac{\Delta\sigma}{\Delta\ln\dot{\varepsilon}}$, versus strain and Cu content for binary Au-Cu alloys, measured through strain rate jumps between $8.33 \times 10^{-5}$ s$^{-1}$ and $8.33 \times 10^{-4}$ s$^{-1}$ at the indicated temperatures [241]. (b) Critical strain versus strain rate and Mg content for Al-Mg tested at room temperature [84]. Note the upper and lower strain rate ranges of the effect were not within the tested range.

Table 6 summarises findings on the effect of precipitate parameters in various superalloys. Most observations are explained based on the effects on the time available for solute to build up, based on changes to the spacing between obstacles or degree of precipitate hardening. Further experimentation is necessary: in particular to separate the effects of precipitate size, spacing and fraction and clarify how the effects vary with temperature and strain rate.

With uncertainty remaining about the roles of precipitates, selected results from other FCC systems are given, of which Al-alloys most commonly show precipitation. In Al-Zn-Mg alloys showing a Guinier–Preston (GP) zone $> \eta' > \eta$ precipitate sequence, the critical strain increased and serration amplitude decreased with ageing time, with the most substantial increase in critical strain at ageing temperatures forming coherent GP zones (Fig. 57) [309,303,435]. The decreased tendency for serrated flow was interpreted partially due to reduced solute concentration in the matrix, though this does not explain the greater effect of the GP zones: it was suggested that the coherent precipitates also trap vacancies [309,303]. Similar trends of precipitation suppressing serrated flow were found in Al-Mg-Si [310,436] and under most conditions in Al-Zn [307], though at the lower end of ageing temperatures, the serration amplitude increased with precipitation. This should be contrasted with the enhancing effect of precipitation on serrated flow in superalloys discussed in several cases above. In Al-Mg the critical strain increased following precipitation when tested in the 'normal' regime but decreased in the 'inverse' regime [432]. Hence, it is not clear that experiments under a single set of temperature/strain rate conditions can fully characterise the effect of precipitation. Further, the precipitate distribution may affect band propagation characteristics, though this is not systematically understood. It was found in an Al-Zn-Mg (in stress control [437]) and Al-Mg alloy [145] that the localised band velocity decreased with precipitate ageing time. Moreover, as shown in Fig. 13, an increased tendency for continuous band propagation has been suggested to be present in precipitate hardened alloys, even in cases where Type C serrations are observed [438,158]. As the transition to non-propagating bands is commonly explained through the breakdown of spatial coupling (Section 3.2.3) due to stress relaxation, the continued occurrence of propagating bands may result from an inability to undergo stress relaxation in the presence of strong obstacles, such as precipitates [439].

To summarise, in most cases precipitates do not appear to be a necessity for serrated flow. The largest effect of precipitation may occur for coherent precipitates or when aged for maximum strength. In some cases, precipitates inhibit serrated flow, raising the critical strain to a maximum and serration amplitude to a minimum around the age treatment for maximum strength. However, in other cases, precipitates encourage serrated flow and the critical strain shows a minimum/ serration amplitude shows a maximum around peak strength. The most common explanation considers precipitates to be barriers to dislocation motion, increasing the waiting time for strain ageing, thus greater precipitate strengthening has comparable effects to increasing the temperature or reducing strain rate [438,158]. However, this explanation may omit to explain several effects, such as the effects on the domain of occurrence of serrations [79], or unusual band propagation characteristics [158], with the latter possibly relating to changes in the spatial coupling. More work is needed to fully understand the roles of precipitate distribution under different deformation conditions.

### 5.4. Chemical composition

In DSA interpretations of serrated flow, it is expected that the extent of serrations should be a strong function of the concentration of the locking solute: for instance, the suppression of serrated flow in interstitial free ferritic steels is well known [440]. In several binary FCC alloys such as interstitial Ni-C [72] and substitutional Au-Cu [241], Cu-Sn [111] and Al-Mg [168,84,441–444], a trend of increasing severity of serrated flow with increasing concentration of solute has been noted, through a more negative SRS (Fig. 58(a)) [241]; a reduced critical strain, mostly during 'normal' DSA [241,72,111] and an increased amplitude of serrations [168,84,441,442,444] under a given set of deformation conditions. Increased C in Ni-C [72] and Mg in Al-Mg [84,443,444] have also been found to shift the regime of serrated flow and transition from 'normal' to 'inverse' DSA to lower temperatures/higher strain rates, as shown in Fig. 58(b) [84]. In some cases it has been found that there may exist a critical solute concentration below which serrations
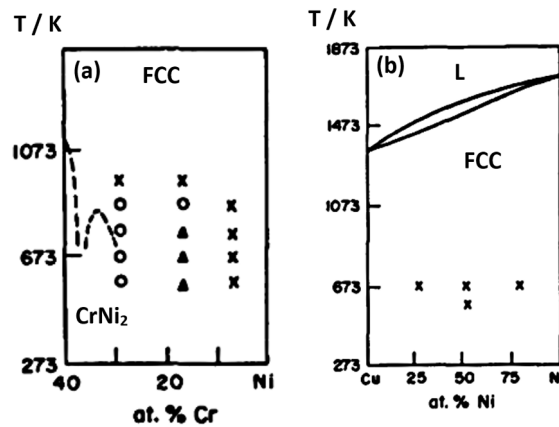
**Fig. 59.** Phase diagrams for the (a) Ni-Cr (b) Ni-Cu binary systems. Dotted lines delimit the single solid solution phase region in Ni-Cr, represented as such due to uncertainty in the precise boundary location. Experimental data points for the occurrence of serrations tested at a strain rate of $10^{-4}$ s$^{-1}$ and the indicated temperatures are shown. Open circle: serrations present, triangle: limited serrations, cross: serrations absent [445]. Note the absence of serrations in the Ni-Cu system with complete solid solubility.
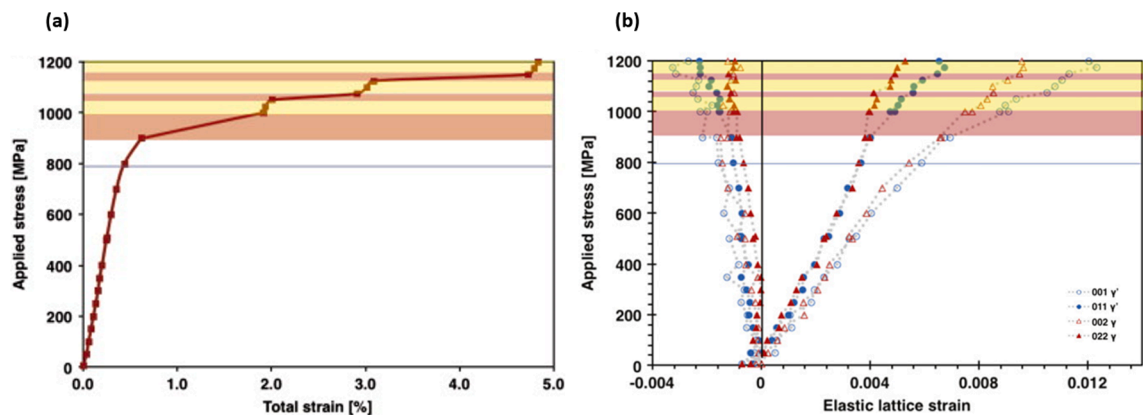


**Fig. 60.** (a) Stress strain curve for RR1000 loaded under tension at 500 °C and $10^{-4}$ s$^{-1}$. Loading was interrupted for 20 min every 50–100 MPa increase in stress at loads indicated by markers for in situ neutron diffraction. Intermittent large increases in strain between loading steps, highlighted in red, were interpreted as indicating the occurrence of a strain burst [448]. (b) Corresponding elastic strain on select lattice planes, measured from Bragg diffraction peak positions, using superlattice reflections for gamma prime. The partitioning of elastic strain between gamma and gamma prime after a strain burst, highlighted in red, was interpreted as arising due to an increased amount of plastic strain in the matrix, where the strain burst may have originated [448].

are absent [241,77,442]: some have interpreted this as the need to pass through the limit of solid solubility, if precipitation or short range order causes serrated flow (Fig. 59) [445,446]. Note that in general such links between short range/long range ordering and serrated flow are purely speculative for most binary alloys. Understanding the role of solute concentration in superalloys on serrated flow is comparatively obscured by the range of alloying elements and phases present. Appendix A lists compositions of the commercial superalloys referred to. The role of an alloying element may be secondary due to its effect on the precipitate distribution through changes to the precipitate equilibrium fractions, solvi and misfit strains, or on the melting point and diffusivity. Further, it is not clear to what extent machine effects (Section 5.2) obscure comparison between different studies. Systematic studies on the effects of small changes in solute concentration are few: increased carbon content raised the serration amplitude in a single phase FCC Ni-Co-Cr alloy [447] and lowered the upper temperature limit of serrations in IN718 [94].

Large amounts of work have been performed to attempt to identify a locking solute species in superalloys. Under the assumption that DSA operates in superalloys [78,9,67], at least in the 'normal' domain, it is widely suggested that the locking species can be inferred by comparing activation energies for atomic diffusion to that for serrated flow, determined from measurements through mechanical testing of the (i) critical strain (Eq. (16)), ii) serration amplitude (Eq. (20)) or (iii) temperature-strain rate boundary between the domains of serrated yielding and smooth flow (Equation (13)) [66,67]. Each method is believed to give comparable activation energies [66,67] and these are often found to be insensitive to composition [49,393] within a given regime. The strain exponent, $m + \beta$, is commonly taken as an indicator of whether interstitial or substitutional diffusion occurs, due to the greater sensitivity of substitutional solute diffusion to vacancy generation: typical suggested values are around 0.5 for interstitial and 2 – 3 for

**Table 7**
Activation energies for bulk diffusion of solute atoms in Ni. Activation energies for pipe diffusion
are typically in the range $0.4 – 0.65 \times$ bulk activation energy [66].

| Element | Activation Energy (kj mol$^{-1}$) | Ref |
|---|---|---|
| C | 137 | [450] |
| Mo | 288 | [450] |
| Nb | 257 | [451] |
| Cr | 260 | [450] |
| Co | 267 | [450] |
| Fe | 277 | [450] |
| Al | 268 | [450] |
| Ti | 275 | [452] |

**Table 8**
Measured activation energies, $Q$, and critical strain exponents, $m + \beta$, for serrated yielding in various superalloys. Chemical compositions of the
superalloys referred to by commercial names are listed in Appendix A. Where aged, the expected main strengthening precipitate is indicated. ST:
Solution treated and quenched. Sub.: Substitutional solute.

| Alloy | Heat | $Q$ (kj mol$^{-1}$) | | $m + \beta$ | | Locking species | | Ref. |
|---|---|---|---|---|---|---|---|---|
| | Treatment | Normal | Inverse | Normal | Inverse | Normal | Inverse | |
| Ni-C | ST | 63 | | 0.63 | | C | | [72] |
| C-276 | ST | 55 | | 2.6 | | Mo | | [91] |
| | ST | 132 | | 4 | | Mo | | [372] |
| GH3535 | ST | 190 | | 5 | | Mo/Cr | | [92] |
| Hastelloy X | ST | 106 | | 2.2 | | Mo | | [107] |
| IN600 | ST | 58 | | | | C | | [278] |
| | ST | 159 | | | | C | | [393] |
| IN617 | ST | 65 | 110 | 0.99 | | C | Sub. | [381] |
| | ST | 110 | 265 | | | C | Cr | [390] |
| IN625 | ST | 98 | | 2.3 | | Mo | | [109] |
| | ST | 101 | | | | Mo/Nb | | [117] |
| | ST | 138 | | 2.1 | | Sub. | | [121] |
| | Aged ($\gamma'$) | 98 | 181 | 1.07 | −2.62 | C | Mo | [180] |
| IN690 | ST | 159 | | | | C | | [393] |
| IN718 | ST | 68 | 132 | | | C | Sub. | [80,425] |
| | ST | 130 | 225 | 2.4 | −1.7 | C | Cr | [66,110] |
| | Aged ($\gamma'$) | 90 | 240 | 4 | −3.5 | C | Mo/Nb | [67] |
| | Aged ($\gamma'$) | 53 | 210 | 1.3 | −2 | C | Nb | [79,82] |
| | Aged ($\gamma'$) | 79 | 141 | | | C | Sub. | [80,425] |
| | Aged ($\delta$) | 67 | 175 | | | C | Sub. | [80,425] |
| IN738LC | Aged ($\gamma'$) | 72 | | 1.22 | | C | | [89] |
| IN X750 | ST | 69 | | | | C | Sub. | [426] |
| | Aged ($\gamma'$) | 57 | | | | C | Sub. | [426] |
| IN800H | ST | 194 | 413 | | | Sub. | Sub. | [251] |
| Nimonic PE16 | ST | 258 | | 1.71 | | Sub. | | [97] |
| | Aged ($\gamma'$) | 240 | | 1.2 | | Sub. | | [382] |
| Nimonic 263 | ST | 68 | 36 | 2.3 | | Cr/Mo | Cr/Mo | [77,6] |
| | Aged ($\gamma'$) | 72 | | 1.4 | | Cr/Mo | | [384] |
| René 88 DT | Aged ($\gamma'$) | | 70 | | −2.15 | | C | [93] |
| TMW A | Aged ($\gamma'$) | 46 | 143 | 2.87 | | Sub. | Sub. | [81] |
| TMW B | ST | 40 | 100 | | | C | Sub. | [49] |
| U720Li | Aged ($\gamma'$) | | 80 | 2.15 | | | Sub. | [9] |
| Waspalloy | ST | 56 | 133 | 0.9 | −2 | C | C | [278] |
| XH55 | Aged ($\gamma'$) | - | 116 | | | C | C | [453] |

substitutional solute diffusion [16,6,82,9,381].

In the 'inverse' DSA domain, many note that classical models of DSA are unlikely to be valid [109,9,382,106]. Some authors have
nonetheless determined an activation energy for solute diffusion in the 'inverse' domain [67,66,110,81,80,180].
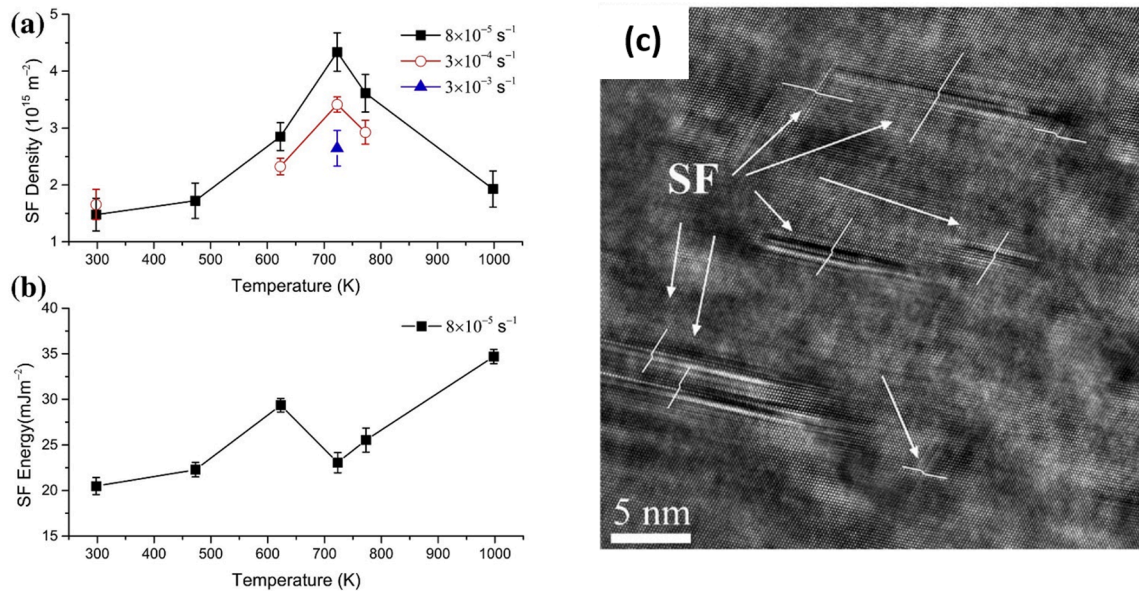
**Fig. 61.** Plots of (a) SF density and (b) SFE calculated from fault width observed following deformation of a TMW series superalloy at the indicated temperatures and strain rates. (c) High Resolution TEM image of specimens following deformation of the TMW series superalloy at 450 °C and 8 × $10^{-5}$ s$^{-1}$ to 3 % strain [51].

In most cases, it is believed that locking processes originate in the $\gamma$ phase. Some observations may support this. First, many studies have noted serrated yielding in solution treated superalloys with nominally zero [123,184] or low equilibrium precipitate volume fractions. Further, neutron diffraction in situ to stepped loading tensile tests in RR1000 at 500 °C may have demonstrated that during a strain burst, elastic strain, as calculated from the lattice/superlattice Bragg diffraction peak positions, was partitioned into the $\gamma'$ phase (Fig. 60), possibly as the matrix underwent a burst of plasticity [448]. However, this effect was less noticeable for finer precipitates and the complex loading scheme with intermittent interruptions makes comparison to serrated flow in monotonic tension difficult. Hence calculated activation energies are commonly compared to that for diffusion in the matrix. Others suggest processes in the ordered $\gamma'$ precipitates may be responsible for serrations [449]. Table 7 lists activation energies for diffusion of several solute species present [66]. Some mechanisms propose that solute segregates to the mobile dislocation core through pipe diffusion from immobile forest dislocations, rather than bulk diffusion [230]. While it is common to attempt to identify a segregating solute based on activation energy calculations, several solutes present have similar activation energies for diffusion.

Table 8 shows the activation energies, critical strain exponents and suggested locking species in a range of superalloys as determined by the methods discussed prior. In most cases, the magnitudes of $Q$ and $m+\beta$ are higher in the 'inverse' domain. This result, coupled with the wide temperature range of serrated yielding in superalloys, is often proposed to arise due to the different mobilities of interstitial and substitutional solute atoms, responsible for locking at low and high temperatures, respectively [96]. However, the activation energies for pipe diffusion of substitutional solutes in Ni and bulk diffusion of interstitial C are comparable [110], as shown in Table 7.

No clear consensus exists as to the identity of the locking solute. Nb and Mo are commonly suggested to lock through large elastic solute-dislocation interactions [117,67,109]. It was noted that the 'inverse' domain was reduced through precipitation of Nb rich precipitates (Fig. 52), and hence suggested that Nb is responsible for 'inverse' DSA [79] though microstructural changes may be significant (Section 5.3). In response, Nb-free modified IN718 was tested and found to still demonstrate serrated yielding [67,454]. It is not clear that serrated yielding in superalloys can be attributed to the segregation of a single solute species. Serrated yielding was found to occur in both Ni-Cr (Fig. 34) and Ni-Mo binary alloys across a similar temperature range to in Nimonic 263, albeit with smaller serration amplitude [77,6].

Direct evidence of solute locking around a dislocation core in superalloys is comparatively lacking. At the time of writing, no studies directly relating the presence of a solute atmosphere around a dislocation core to serrated flow in superalloys, for instance through TEM-EDX or APT, have been reported in the open literature.

One difficulty in superalloys is the range of intermediate temperature deformation mechanisms observed (Section 1.1): serrated yielding has been observed in cases where the main mechanism of overcoming precipitates is APB shear [449,425], precipitate bowing (Fig. 54(d)) [50], SF shear [78,455] and twinning or microtwinning [427,456–458]. Hence, it is not clear if serrated flow is linked to a particular operative slip system or dislocation structure. However, this warrants further attention: in particular, as most investigations select a region of interest for TEM along the gauge length at random, it is unclear if there are differences in the dislocation structure inside/outside of the rapidly deforming localised bands. There is evidence that 'inverse' DSA may be correlated to the formation of a high SF density, particularly in high Co alloys (Fig. 56) [95,78,49,92,455,251], though in Haynes 282 and IN617, slip
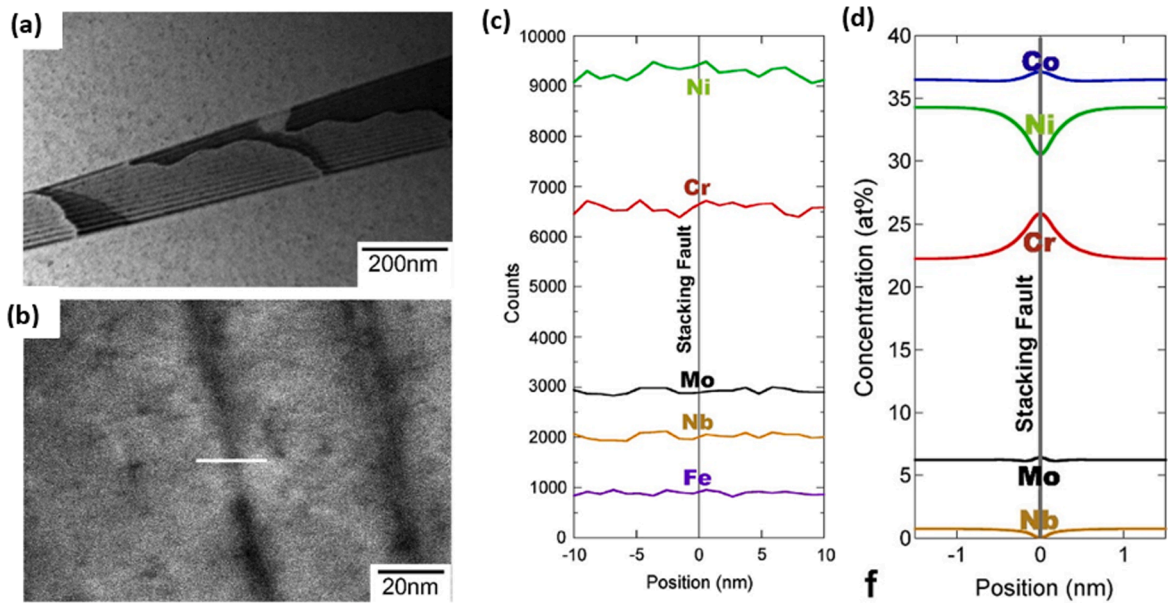
**Fig. 62.** (a)(b) TEM images of a SF formed after static ageing of superalloy SPRON 510 at 700 °C for 1 h subsequent to room temperature deformation to 2 % strain. (a) TEM bright field (b) Scanning Transmission Electron Microscopy (STEM) bright field image. (c) EDX linescan over SF. The linescan direction is indicated by the white line in (b). (d) Phase field modelling simulations of segregation to a SF in $\gamma$ [459].

bands were observed at all temperatures, and no SFs [373,381,378]. A recent review discusses in detail experimental observations of the relation between 'inverse' DSA and SF shear [23].

From this observation, several studies have attributed serrated yielding in superalloys to the presence of SFs, either through locking of partial dislocations by solute (Section 3.3) due to 'dynamic Suzuki segregation' [214,345,95,51], or localised strengthening due to short range order or precipitation resulting from segregation [81,459].

Indirect evidence may support the presence of Suzuki segregation in the matrix. The dissociation width of partial dislocations and SF density showed a maximum following tensile testing in the 'inverse' DSA regime (Fig. 61) [95,51], despite the SFE being expected to increase with temperature due to the increased stability of the FCC phase compared to the Hexagonal Close-Packed (HCP) phase with temperature[365], leading to partial constriction. This was attributed to a reduction in SFE through solute segregation [95]. Based on the idea that serrated flow in superalloys relates to SF shear, the effects of substituting Co for Ni to lower the SFE were investigated: the domain of serrated flow was found to shift to higher temperatures with increased Co content [49]. Further, it was noted that pre-straining through creep at 725 °C/625 MPa led to larger amplitude serrations upon subsequent tensile testing in the serrated flow domain: the authors proposed that this was a consequence of the large resulting SF density [460]. Conversely, others suggested that the effect of Co in Ni alloys is likely due to a decreased C diffusivity with increasing Co content, rather than due to changes to the SFE [73]. However, direct evidence is less clear. Phase field simulations, where the concentration and stacking sequence of {111} planes were relaxed based on thermodynamic phase stability data, demonstrated a driving force for Co, Cr and Mo segregation to a SF in $\gamma$ (Fig. 62)). TEM-EDX showed no evidence of segregation, with the authors suggesting that one of the main difficulties is due to the similar $K_\alpha$ X-ray energies of Ni, Co and Cr [459], though a recent TEM-EDX study may have observed such segregation to SFs following deformation at 500 °C [461]. In a separate study, TEM-EDX may have shown segregation of Mo and Ti to the SF interface and of Mo and Nb within slip bands, though peaks were hard to resolve over noise and not all partials showed segregation [95]. No evidence of segregation was found to SFs in IN718 formed at 425 °C [462].

## 5.5. Grain size and texture

The effect of grain size on serrated yielding is relatively unexplored in superalloys, likely owing to the difficulty of its control independently of the precipitate distribution [25]. An increasing critical strain with grain size has been observed in Cu-30Zn (wt.%) [463] and Al-Mg [464], though the trend was only tested in the regime of 'normal' DSA and other cases have found little effect of grain size in Al-Mg-Si [465]. The most classical understanding notes that finer grain sizes lead to greater dislocation densities [466], hence a lower strain is required to build up sufficient dislocation density to observe serrations [463], or that the waiting time of dislocations at obstacles is increased [244]. Thus, DSA is expected to be more prominent in fine-grained materials. The amplitude of serrations has also been found to increase for finer grain sizes [275,465,467,104], rationalised in a similar way [114]. The critical strain in Al-3 Mg increased with grain size during 'normal' DSA, but the trend was reversed for 'inverse' DSA (Fig. 63) [468], and an increased tendency for Type B/C serrations has been observed in fine-grained Al-Mg alloys [158]. Investigations in TWIP steels have also found 'inverse' trends of decreasing critical strain with grain size [469,470]. A detailed understanding of effects on the band propagation
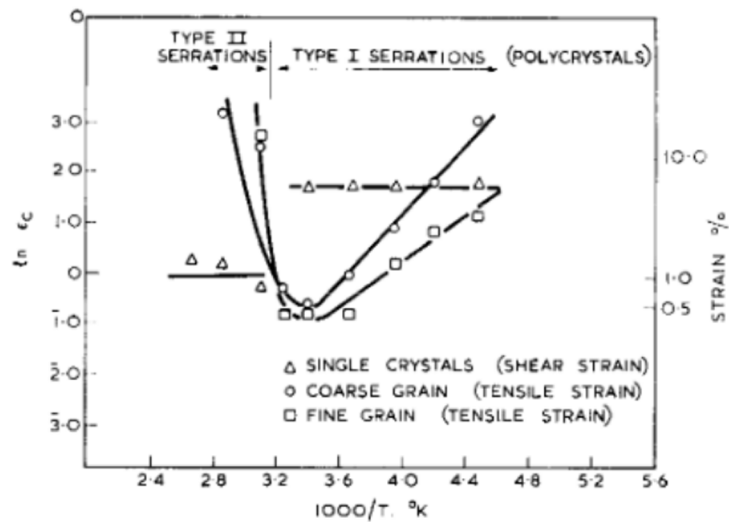
**Fig. 63.** Effect of grain size on critical strain to onset of serrated flow at different test temperatures for Al-3 Mg [468].
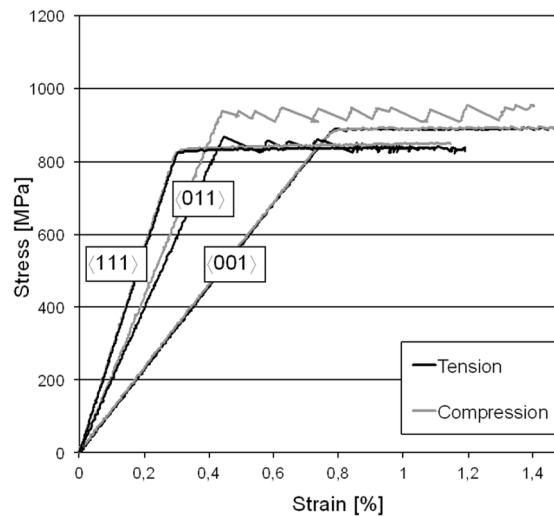


**Fig. 64.** Stress–strain curves for single crystal superalloy MD2, loaded at 500 °C and $10^{-5}$ s$^{-1}$ in different orientations [215].

characteristics is lacking. No effect of grain size on the strain increment between serrations or bandwidth was noted during Type A serrations for three different grain sizes in Cu-Al [163], while a TWIP steel demonstrated an increased strain increment in finer grained samples [471]. An increase in band propagation velocity was noted in finer grained specimens of Al-Mg [174], with the opposite trend reported in a TWIP steel [471].

Conversely, in the limit of extreme grain refinement to sub-micron scale, suppression of serrated flow has been observed in Al-Mg alloys [158,439], despite exhibiting propagating weakly localised bands [158] (Section 2.4). Such observations have been interpreted through the suppression of large scale correlated dislocation motion [439], but with the inhibition of stress relaxation due to strong barriers leading to a continued strong spatial coupling [439] for continuous band propagation across all conditions, similar to in precipitate hardened alloys (Section 5.3). Conflicting results on the corresponding SRS in ultrafine grained materials have been reported, in some cases continuing to show negative SRS [244]. In other cases, a vanishing but non-negative SRS was observed [158] which may suggest that dislocation synchronisation influences the SRS, as hypothesised elsewhere [270] but not incorporated into classical DSA models for serrated flow (Section 3.2).

Effects of grain size in superalloys are not verified. Serrations in a Ni-Co superalloy were more prominent at 400 °C when subsolvus heat treated (fine grained) compared to when supersolvus treated (coarse grained), perhaps as expected classically [434]. However, 'inverse' trends in the critical strain with grain size have been observed in IN718 when tested at 200 °C, following grain growth heat treatments above the $\delta$ solvus at 1020 °C. The amplitude of serrations at this test temperature was very small for all grain sizes as testing was close to the edge of the temperature domain of serrated flow [458]. Another Ni-Co superalloy, tested at 450 °C in the
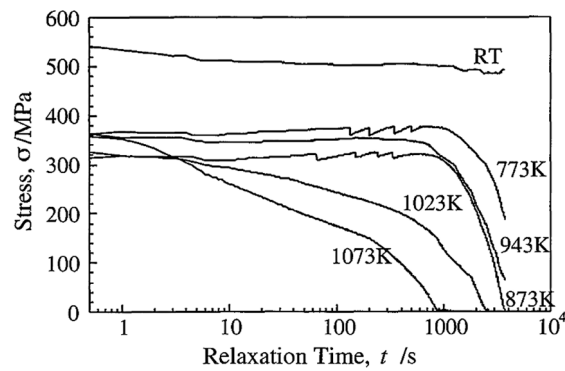
**Fig. 65.** Stress relaxation curves for superalloy SPRON 510 at indicated temperatures, with the crosshead position fixed following deformation at $5.2 \times 10^{-4}$ s$^{-1}$ to 12 % strain [345].
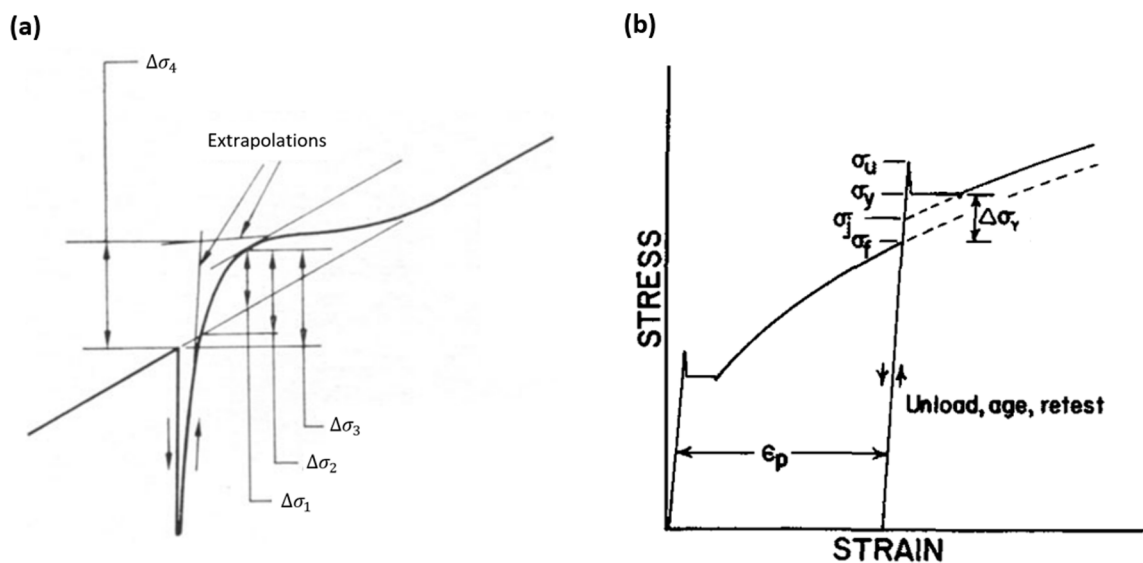


**Fig. 66.** Schematic illustration of methods of measuring the magnitude of the yield effect (a) for a poorly defined Lüders extension [484] (b) for a well defined yield point [479], the effect may be measured through the permanent increase in strength, $\sigma_j - \sigma_f$, the upper yield strength increment, $\sigma_u - \sigma_f$ or the lower yield strength increment, $\sigma_y - \sigma_f$ [479].

'inverse' DSA domain, showed a lower critical strain when supersolvus treated than subsolvus, contrary to classical explanations, and smaller mean stress drop amplitude [472]. It was noted that the effect of grain size may be negligible compared to changes in precipitate distribution [434].

Recent work has shown a possible orientation dependence of serrations in single crystal superalloys [215,473], which is not accounted for in classical models. A loading axis parallel to <110> was found to lead to more prominent serrations than <100> or <111> slip (Fig. 64). This was attributed to the activation of a single slip system in <110> loading, leading to the formation of more localised slip bands [215,473]. Little work directly relating texture and serrated yielding has been reported in polycrystalline alloys. It was suggested that high <100> orientation with the loading direction, developed during additive manufacturing of IN625, led to the suppression of DSA. However, they also note that the high cooling rates led to the formation of many fine secondary precipitates [474].

## 6. Static ageing

As noted in Section 2.2, an upper and lower yield point have rarely been observed in FCC alloys in as processed conditions [475]. Methods to induce a yield drop involve an initial prestrain followed by subsequent deformation, differing based on the initial/final strain rates and temperature, degree of prestrain and the stress during ageing. Some studies age close to peak stress, either by holding the load fixed [66,476] or crosshead fixed [477,280,476,478]. However, in both cases some plastic deformation will occur, leading to stress relaxation under fixed displacement [345,477] and making it difficult to assess the time available for solute diffusion. Stress relaxation tests on a Co-Ni superalloy demonstrated that, at temperatures where serrated flow occurred, sudden load drops were occasionally observed during relaxation, as shown in Fig. 65 [345]. Hence in other cases, the load is removed fully [479] or partially
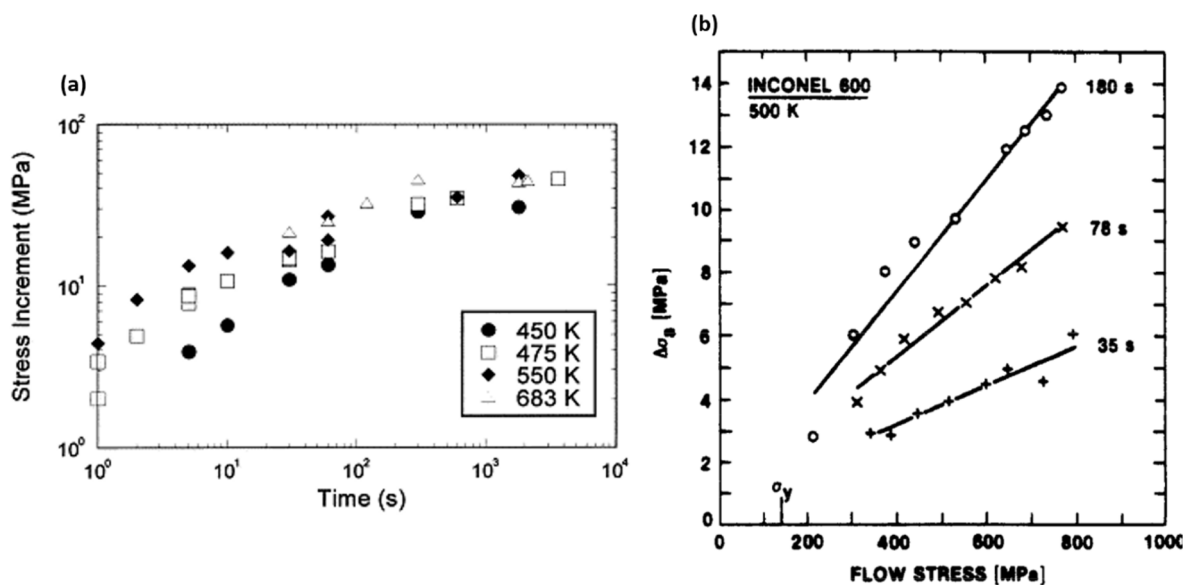
**Fig. 67.** (a) Magnitude of the upper yield strength increment versus ageing time and temperature for IN718, deformed at $1.3 \times 10^{-4}$ s$^{-1}$. Ageing was performed after 16 % prestrain and at the same temperature to during deformation, with the specimens held at constant stress during ageing [66]. (b) Prestrain (flow stress just prior to ageing) and ageing time dependence of the upper yield strength increment for IN600, deformed at 500 K and $1.7 \times 10^{-4}$ s$^{-1}$. Ageing was performed at the same temperature under a constant load of approximately 30 % of the flow stress just prior to ageing [274].

[274] prior to ageing. It is worth noting that a yield point upon unloading may be present even in pure FCC metals [480], referred to as the Haasen Kelly effect [480–482]. This is usually interpreted in terms of dislocation–dislocation locking interactions upon unloading, for instance through the formation of jogs, sessile dislocations or dislocation arrays. Several features of the yield point in pure FCC metals are reviewed in [314]: in particular, the magnitude of the drop often increases with prestrain [480], extent of unloading [483] and decreasing temperature [480], and appears insensitive to ageing time [483]. Whether the Haasen Kelly effect is accompanied by Lüders phenomena is unclear. In several FCC alloys such as Al-Cu [242] and Cu-Zn [478], ageing peaks have been observed both with the load removed or maintained, though it is clear that care is necessary to interpret the yield point as arising solely due to strain ageing. For instance, a time independent component to the ageing peak in Hadfield steel was attributed to the Haasen Kelly effect [74].

Further, a source of ambiguity arises in the definition of the size of the yield drop in FCC alloys, since a developed Lüders strain is often not seen, thus there is not a clear consensus on how to extract the drop over a background of work hardening (Fig. 66). Strain ageing peaks have been observed in Ni-C [274,325,479,477], Fe-Mn-C steels [74], Cu-Zn [478], Al-Mg [280], IN718 [66] and Inconel 600 [274] with largely similar characteristics. The upper yield strength increment (Fig. 66) increased with time [478,274,66], though reaching saturation at long times [274,66]; with prestrain, to a maximum [478,274]; with temperature [478,66] and with subsequent strain rate [274], with select results shown in Fig. 67. Similar trends were found in the lower yield stress increment [477,74,479], with the exception that in Ni-C, it was found that the lower yield stress increment fell for long ageing times, rather than saturating [479]. Conversely, it was found in a series of stainless steels that yield points only developed if ferritic phases were present when aged at 170 °C [485]. Classical theories of strain ageing in mild steel do not predict a strain dependence of the stress drop for interstitial solutes (assumed proportional to the solute concentration, Eq. (8)), since the diffusivity is not dependent on vacancies [486,487]. While in some models, the prestrain dependence arises through its effect on vacancy generation and solute mobility [210], Kocks argue that the prestrain dependence cannot just arise from the enhanced solute mobility in Ni-C, since interstitial carbon diffusivity should be insensitive to vacancy concentration and the strain dependence continues even when the ageing time dependence saturates [274]. Empirical results discussed in Section 3.2.2 may suggest that the saturation locking strength of strain ageing is also an increasing function of strain[124,271,272,247], though without clear theoretical justification.

The effect of subsequent strain rate was mostly attributed to the rate sensitivity of the steady state deformation [274,210]. Varying the strain rate during prestrain from that during reloading, the peak height was found mostly insensitive to strain rate: rather, the change in stress drop came from the change in steady state stress (Fig. 68) [274]. It was suggested that the size of the yield drop is given by

$$\Delta\sigma = \sigma(t) - \sigma(\frac{\rho_m b d}{\dot{\varepsilon}}), \tag{48}$$

where the first term denotes the stress increase due to SSA during a hold time, *t*, for instance assumed proportional to the solute concentration, Eq. (8), and the second term denotes the steady state effect of DSA on the mean stress, also proportional to Eq. (8) but with the time available for solute diffusion prescribed by the strain rate (Eq. (17)) [274,210]. As for slower strain rates, more solute
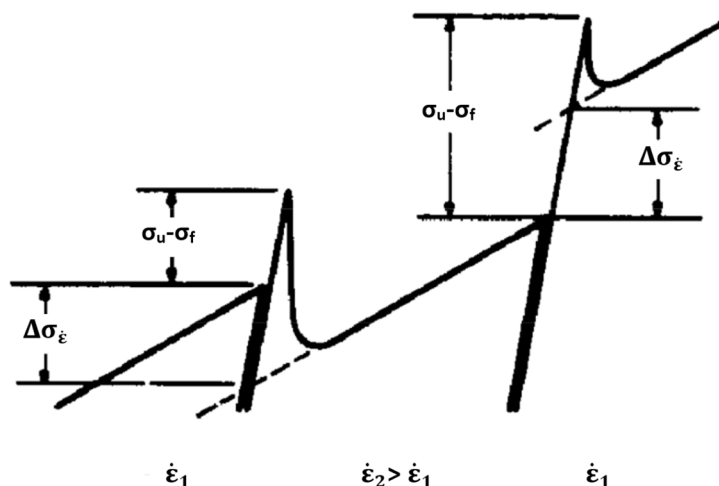
**Fig. 68.** Schematic measurements of the yield drop magnitude, $\sigma_u - \sigma_f$ in Ni-C for strain rates $\dot{\varepsilon}_1$ and $\dot{\varepsilon}_2 > \dot{\varepsilon}_1$. The difference in yield drop magnitudes is approximately equal to the rate sensitive change in flow stress, $\Delta\sigma_{\dot{\varepsilon}}$ [274].

remains around the dislocation cores due to DSA, there is less of a yield drop [274]. Kubin suggests that this also explains the decrease in stress drop magnitude with prestrain at higher temperatures/strains, since the dominant effect of strain is to raise the baseline stress [210]. However, Schwab and Ruff argue that the 'true' constitutive yield drop magnitude, such as that in Eq. (48), is not observed experimentally [287]. This follows since, firstly, stress concentrations will lead to the yield criterion locally being achieved early, for instance due to test specimen bending. Secondly, the stress at the lower yield point reflects that to continue breaking dislocations ahead of the Lüders band from their atmospheres, reduced from the initial value at the upper yield point due to incompatibility stresses (Section 3.2.3). Under a simple model where equal and opposite incompatibility stresses arise on elements of the test specimen just ahead of/behind the Lüders band front, due to an assumed step change in strain at the interface, continuity between elements in series implies that the stress at the lower yield point lies halfway between the 'true' upper and lower yield points[9].

## 7. Summary and outlook

A great deal of work has been devoted to understanding serrated flow over the last century. It is now well accepted that the origins of such serrations can in most cases be traced to the occurrence of a negative SRS, leading to a tendency for strain localisation and concurrent drops in stress [10], and that DSA is one possible mechanism to account for this [236], though the limitations of current models for DSA in accounting for empirical observations across different length scales and possible alternative origins of serrated flow (Section 3.3) were discussed. The macroscopic features of serrations have generally been well characterised empirically, especially their variation with temperature and strain rate, such as the temperature/strain rate/strain boundaries of occurrence (Section 2.1) and to a lesser extent the distribution of serration amplitudes (Section 2.3) and the characteristics of band propagation (Section 2.4). However, less attention has been paid to the effects of other microstructural, compositional and testing parameters on serrated flow, as discussed in Section 5, and to the static strain ageing behaviour of superalloys.

Approaching 125 years since Portevin and Le Chatelier's observance of serrations in aluminium alloys [55] and 75 years since the proposal of strain ageing [13], several questions remain. The main areas for development comprise four inter-related stages: determining the atomic scale mechanisms for serrated flow in FCC alloys; the incorporation of these mechanisms into multiscale physical models; the application of such models to the variability with composition, microstructure and temperature; and the prediction of the effects of serrated flow in complex loading situations such as fatigue.

While Cottrell atmosphere formation is almost universally accepted as the mechanism for serrated flow in ferritic steels containing interstitial solutes, it remains an open question whether this mechanism can be extended to FCC alloys as is often implicitly assumed. Several causes for doubt exist: such as the weaker solute locking effect in the FCC lattice, the occurrence of serrated flow in supposedly interstitial-free cases and the uncertainty about whether long range substitutional diffusion has sufficient mobility to account for the observed phenomena (Section 3.2). This is compounded by a general lack of knowledge of experimental deformation-enhanced diffusion coefficients at the temperatures where serrations are present.

Furthermore, recent advances in understanding the origins of instabilities [10] have allowed the development of alternate theories for time-dependent locking: for instance, related to the short range cross-core diffusion in Al-Mg [20], or the cutting of Mn-C pairs in TWIP steels [21]. It remains to be seen whether there exists a common mechanism for the intermediate temperature instability in multiple FCC alloys, or the mechanism varies from case to case. This is in the context where there are many common features between

---

[9] Numerically different values follow based on consideration of the band angle and triaxial stress state, discussed in further detail in [287].

different alloys, for example, the occurrence of a 'normal' and 'inverse' critical strain, and similar serration Types A, B and C and with propagation characteristics. In the case of superalloys, the popularity of mechanisms relating 'inverse' DSA to SF shear is attested to in a recent review [23], although one could argue that the largest barrier to the acceptance of this idea is the ubiquity of systems in which 'inverse' DSA is observed, and whether this is matched by a ubiquity of SF shear deformation modes. A point worth highlighting is the observation of serrated flow in binary Ni-Cr and Ni-Mo [77,75] with features largely comparable to superalloys, suggesting that microstructural and compositional complexity is not a necessary feature for serrated flow.

While a mechanism based on solute diffusion in the vicinity of defects is probable, it is not believed that there is yet sufficient experimental evidence to take a firm stance as to the nature of the solute atoms (interstitial or substitutional), defects (dislocations or planar faults) or diffusion paths (long or short range) involved. Binding energy and activation energy calculations based on computational techniques such as DFT [20,334] or Molecular Dynamics (MD) may assist the ruling out interactions: for instance those which do not interact strongly, or develop in appropriate timescales. The complexity of such simulations may, however, be prohibitive, due to the non-periodic nature of the structure around a dislocation core, range of possible reaction pathways and possible lack of well calibrated potentials for MD.

In particular, the occurrence of an 'inverse' critical strain lacks an accepted mechanism, despite various explanations proposed in Section 3.2.2, arguably as does the cause of the disappearance of serrations at high temperature/low strain rates. Suggested explanations for the latter relate to the point where thermal fluctuations exceed the solute–defect binding energy (Eq. (9)), though, for a binding energy of the order 1 eV [231], the condition $W = kT$ is not met until approximately $10^4$ K. Conventional wisdom is that the disappearance of serrations occurs when solutes are sufficiently mobile to move with the dislocation core [227] though it is not clear whether this is compatible with the observation that, in some cases, the serration amplitude continuously increases up to the abrupt disappearance. In some cases it has been suggested that serrations disappear as solute gets 'locked up' by another mechanism [278,73] or result from the loss of negative SRS, as the mean solute concentration around a dislocation becomes insensitive to strain rate when saturation is reached [237]. Furthermore, the processes by which continued deformation occurs if dislocations are locked by a solute atmosphere need clarification: is the majority of deformation mediated by the generation of new solute-free dislocations [259,15], the breakaway of existing dislocations from their solute atmospheres [236,235] or the viscous drag of existing solute atmospheres [209]?

The experimentalist plays an important role in identifying which mechanisms can be detected. Characterisation techniques such as TEM or APT (in Al-Mg [337] and TWIP steels [334]) have been applied to detect solute atmospheres, or *ex situ* neutron scattering to detect short range Mn-C order in TWIP steels [173]. Two points arise: first, it is important to bear in mind that, in most cases, serrated flow is believed to be accompanied by macroscopic bands of localised deformation, with very different behaviour inside and outside the bands. Thus, significant information is lost about dislocation arrangements unless a multiscale approach is taken, to locate deformation bands and use this information to guide selection of regions for characterisation [173,334]. Second, in some cases yield points have been observed after short (20 s) holds following a prestrain (Section 6). It is likely that the structures viewed following an elevated temperature tensile test may have time to form during cooldown, thus a greater understanding of the static ageing properties is vital. This may be of particular concern in interpreting data in TWIP steels and Al-Mg alloys, where serrated flow occurs even at room temperature: in this respect, superalloys perhaps offer an 'easier' system to investigate, due to the absence of serrations under 200 °C.

A second area is in the development of multiscale models able to apply the atomic scale mechanisms for serrated flow to predict macroscopic properties in addition to the critical strain or mean stress. For instance, the ability of current models to rationalise the occurrence of macroscopic strain bursts and the localisation of deformation in space is still incomplete [269]. These effects are usually accounted for through spatially-dependent coupling at the mesoscale, such that any local slip triggers further local slip. Models including such an interaction have reproduced propagating or non-propagating localised deformation bands, though the precise details of the coupling across a range of length scales remain unclear [269,19] and further understanding is lacking as to how changes in the coupling lead to different dislocation dynamics. Further, the widely accepted link between Type C serrations and 'inverse' DSA (Section 2.2) remains empirical. In particular, an experimental picture of how localised deformation bands nucleate and propagate at the dislocation scale and grain-to-grain scale remains unclear, requiring experimental techniques with both high spatial and temporal resolution. AE may offer sufficient temporal resolution to detect finer scale slip events comprising a serration *in situ* [488,139], though AE and conventional spray paint based DIC techniques both lack the ability to spatially resolve finer scale spatial internal structure within a deformation band.

Thirdly, the effects of temperature and strain rate on the macroscopic manifestations of serrated flow in established alloys are largely well characterised (Section 2), but predicting the effects of other microstructural and compositional parameters in more complex alloys, such as superalloys, is still difficult, either empirically or through an understanding of the mechanisms of serrated flow across a range of length scales and would benefit greatly from the application of improved modelling.

Finally, the most impactful effect of an improved understanding of serrated flow in superalloys would be to elucidate the factors controlling complex mechanical properties such as fatigue life. It is widely believed the mechanism leading to serrated flow also manifests through the following [53]: a negative SRS of the yield stress and ultimate tensile strength, anomalous hardening, a decrease in ductility and an increase in work hardening. All of these potentially play a role in determining fatigue life, but, as discussed in Section 5, several observations in superalloys [9] throw into question the generality of these observations, particularly the last two. Understanding the fundamental mechanisms governing serrated flow and implementing this into improved modelling will play a crucial role in unravelling this technologically important behaviour.

**Declaration of Competing Interest**

The authors declare that they have no known competing financial interests or personal relationships that could have appeared to

**Table 9**
Nominal compositions of superalloys referred to by commercial name (in wt.%).

| Alloy | Ni | C | Cr | Co | Al | Ti | Ta | Mo | Nb | Fe | W | Zr |
|---|---|---|---|---|---|---|---|---|---|---|---|---|
| C-276 | Bal. | 0.01 | 16.0 | 2.5 | - | - | - | 16.0 | - | 5.0 | 4.0 | - |
| GH3535 | Bal. | 0.05 | 7 | - | - | - | - | 16.0 | - | 4.0 | - | - |
| Hastelloy X | Bal. | 0.10 | 22.0 | 1.5 | 0.25 | - | - | 9.0 | - | 18.5 | 0.6 | 0.06 |
| IN600 | Bal. | 0.08 | 15.5 | - | - | - | - | - | - | 8.0 | - | 0.06 |
| IN617 | Bal. | 0.07 | 22.0 | 12.5 | 1.0 | 0.3 | - | 9.0 | - | - | - | - |
| IN625 | Bal. | 0.05 | 21.5 | - | 0.2 | 0.2 | 3.6 | 9.0 | - | 2.5 | - | - |
| IN690 | Bal. | 0.025 | 29.0 | - | - | - | - | - | - | 9.0 | - | - |
| IN718 | Bal. | 0.04 | 19.0 | - | 0.5 | 0.9 | - | 3.0 | 5.1 | 18.5 | - | - |
| IN738LC | Bal. | 0.11 | 16.0 | 8.5 | 3.5 | 3.5 | 1.7 | - | 0.8 | 0.35 | - | 0.04 |
| INX750 | Bal. | 0.04 | 15.5 | - | 0.7 | 2.5 | - | - | 1.0 | 7.0 | - | - |
| IN783 | 28.0 | 0.03 | 3.0 | Bal. | 5.5 | 0.3 | - | - | 3.0 | 26.0 | - | - |
| IN800H | Bal. | 0.08 | 21.0 | - | 0.4 | 0.4 | - | - | - | 39.5 | - | - |
| Nimonic PE16 | Bal. | 0.05 | 16.5 | 1.0 | 1.2 | 1.2 | - | 1.1 | - | 33.0 | - | - |
| Nimonic 263 | Bal. | 0.06 | 20.0 | 20.0 | 0.5 | 2.1 | - | 5.9 | - | - | - | 0.02 |
| René 88 DT | Bal. | 0.027 | 15.0 | 18.5 | 3.0 | 3.6 | 2.0 | 5.0 | 1.1 | - | - | 0.06 |
| RR1000 | Bal. | 0.03 | 16.0 | 13.0 | 2.1 | 3.7 | - | 4.0 | 0.7 | - | 4.0 | 0.03 |
| TMW A | Bal. | 0.02 | 14.0 | 23.0 | 2.3 | 5.6 | - | 2.8 | - | - | 1.2 | 0.03 |
| TMW B | Bal. | 0.02 | 14.0 | 15.0 | 2.3 | 5.6 | - | 2.8 | - | - | 1.2 | 0.03 |
| U720LI | Bal. | 0.025 | 16.0 | 15.0 | 2.5 | 5.0 | - | 3.0 | - | - | 1.25 | 0.05 |
| Waspalloy | Bal. | 0.03 | 19.5 | 13.5 | 1.3 | 3.0 | - | 4.3 | - | - | - | - |
| XH55 | Bal. | 0.04 | 17.0 | - | 1.8 | - | - | 9.0 | 2.0 | 12.0 | - | - |

influence the work reported in this paper.

## Acknowledgements

## Appendix A. Compositions of Superalloys

The chemical compositions of superalloys referred to in this review are listed in Table 9.

## References

[1] European Aviation Safety Agency. European aviation environmental report 2019. EASA Publications; 2019.
[2] Segersäll M, et al. Thermal-mechanical fatigue behaviour of a new single crystal superalloy: effects of Si and Re alloying. Acta Mater 2015;95:456–67.
[3] Kovarik L, et al. Microtwinning and other shearing mechanisms at intermediate temperatures in Ni-based superalloys. Prog Mater Sci 2009;54(6):839–73.
[4] Pepelnjak T, Barisic B. Analysis and elimination of the stretcher strains on TH415 tinplate rings in the stamping process. J Mater Process Technol 2007;186(1):111–9.
[5] Davis J. Nickel, cobalt and their alloys. ASM International, 1 edition; 2000.
[6] Han G, et al. Activation energy calculations for the Portevin–Le Chatelier effect in Nimonic 263 superalloy. Metall Mater Trans A 2015;46(10):4629–35.
[7] Hart E. Theory of the tensile test. Acta Metall 1967;15(2):351–5.
[8] Brindley B. The effect of dynamic strain-ageing on the ductile fracture process in mild steel. Acta Metall 1970;18(3):325–9.
[9] Gopinath K, et al. Dynamic strain ageing in Ni-base superalloy 720Li. Acta Mater 2009;57(4):1243–53.
[10] Penning P. Mathematics of the Portevin-Le Chatelier effect. Acta Metall 1972;20:37–44.
[11] Gallar L. Gas turbine shaft over-speed/failure performance modelling. PhD Thesis, Cranfield University; 2010.
[12] European Aviation Safety Agency. Certification specifications for engines CS-E - amendment 3. Technical report. EASA Publications; 2010.
[13] Cottrell A, Bilby B. Dislocation theory of yielding and strain ageing of iron. Proc Phys Soc A, 1949;62(1): 49–62.
[14] Sleeswijk A. Slow strain hardening of ingot iron. Acta Metall 1958;6:598–603.
[15] McCormick P. A model for the Portevin–Le Chatelier effect in substitutional alloys. Acta Metall 1972;20(3):351–4.
[16] Van Den Beukel A. On the mechanism of serrated yielding and dynamic strain ageing. Acta Metall 1980;28(7):965–9.
[17] McCormick P. Theory of flow localisation due to dynamic strain ageing. Acta Metall 1988;36(12):3061–7.
[18] Kubin L, Estrin Y. Dynamic strain ageing and the mechanical response of alloys. J de Physique 1991;1(6):929–43.
[19] Lebyodkin M, et al. The Portevin-Le Chatelier effect and Beyond. Springer; 2021.
[20] Curtin W, et al. A predictive mechanism for dynamic strain ageing in aluminium–magnesium alloys. Nat Mater 2006;5(11):875–80.
[21] Lee S, et al. On the origin of dynamic strain aging in twinning-induced plasticity steels. Acta Mater 2011;59(17):6809–19.
[22] Singh R, Doherty R. Strengthening in MULTIPHASE (MP35N) alloy: part II. Elevated temperature tensile and creep deformation. Metallurgical transactions A 1992;23:321–34.
[23] Cui C, et al. Portevin-Le Chatelier effect in wrought Ni-based superalloys: Experiments and mechanisms. J. Mater. Sci. Technol. 2020:16–31.
[24] Kim J, et al. On the tensile behavior of high-manganese twinning-induced plasticity steel. Metallurgical and Materials Transactions A 2009;40(13):3147.
[25] Reed R. The superalloys: Fundamentals and applications. 1 edition,. Cambridge University Press; 2006.
[26] Kear B, Wilsdorf H. Dislocation configurations in plastically deformed Cu3Au alloys. Transactions of the Metallurgical Society AIME 1962;224:382–6.
[27] Williams J, Starke E. Progress in structural materials for aerospace systems. Acta Mater 2003;51:5775–99.

[28] Kahlweit M. Ostwald ripening of precipitates. Adv. Colloid Interface Sci. 1975;5(1):1–35.

[29] E.M. Knoche. Influence of the precipitate size on the deformation mechanisms in two nickel-base superalloys. PhD Thesis, University of Manchester, 2011.

[30] Papadaki C, et al. On the dependence of γ′precipitate size in a nickel-based superalloy on the cooling rate from super-solvus temperature heat treatment. Materials 2018;11(1528):1–10.

[31] Galindo-Nava E, et al. On the prediction of the yield stress of unimodal and multimodal γ′nickel-base superalloys. Acta Mater 2015;98:377–90.

[32] Brooks J, Bridges P. Metallurgical stability of Inconel alloy 718. Superalloys 1988;1988:33–42.

[33] Lu Z, et al. Spin-polarization-induced structural selectivity in Pd3X and Pt3X (X=3d) compounds. Phys. Rev. Lett. 1995;75(7):1320–3.

[34] Jackson M, Reed R. Heat treatment of Udimet 720Li: the effect of microstructure on properties. Materials Science and Engineering: A 1999;259(1):85–97.

[35] Reed R, et al. Characterisation and modelling of the precipitation of sigma phase in Udimet 720 and Udimet 720Li. Metallurgical and Materials Transactions A 1999;30:521–33.

[36] Rae C, Reed R. The precipitation of topologically close-packed phases in rhenium-containing superalloys. Acta Mater 2001;49:4113–25.

[37] C. Rae et al. Topologically close packed phases in an experimental rhenium-containing single crystal superalloy. Superalloys 2000, TMS, pages 767–776, 2000.

[38] Chen Q, Knowles D. The microstructures of base/modified RR2072 SX superalloys and their effects on creep properties at elevated temperatures. Acta Mater 2002;50:1095–112.

[39] Rae C, Reed R. Physical metallurgy of the nickel-based superalloys, chapter 22. 5 edition,. Elsevier; 2015. p. 2215–90.

[40] Smith T, et al. Creep deformation mechanism mapping in nickel base disk superalloys. Mater. High Temp. 2016;33(4–5):372–83.

[41] Chu Z, et al. Tensile Property and Deformation Behaviour of a Directionally Solidified Ni-Base Superalloy. Materials Science and Engineering: A 2010;527(12): 3010–4.

[42] Unocic R, et al. Deformation mechanisms in Ni-base disk superalloys at higher temperatures. Superalloys 2008;2008:377–85.

[43] Tian C, et al. Effects of Co content on tensile properties and deformation behaviors of Ni-based disk superalloys at different temperatures. Mater. Des. 2015;88 (1):121–31.

[44] Qi D, et al. Temperature effects on the transition from Lomer-Cottrell locks to deformation twinning in a Ni-Co-based superalloy. Scripta Mater. 2016;125(1): 24–8.

[45] Viswanathan G, et al. Investigation of creep deformation mechanisms at intermediate temperatures in René 88 DT. Acta Mater 2005;53:3041–57.

[46] Rae C, Reed R. Primary creep in single crystal superalloys: origins, mechanisms and effects. Acta Mater 2007;55(3):1067–81.

[47] Knowles D, Chen Q. Superlattice stacking fault formation and twinning during creep in γ/γ′single crystal superalloy CMSX-4. Materials 2003;50:1095–112.

[48] Decamps B, et al. On the shearing mechanism of gamma prime precipitates by a single (a/6)<112> shockley partial in Ni-based superalloys. Phil Mag 2004;84 (1):91.

[49] Cui C, et al. Dynamic strain aging in Ni base alloys with different stacking fault energy. Superallloys 2012;2012:715–22.

[50] Wang X, et al. The dependence of Portevin-Le Chatelier effect on the γ′precipitates in a wrought Ni-Base superalloy. Metallurgical and Materials Transactions A 2016;47(12):5994–6003.

[51] Xu J, et al. Stacking fault effects on dynamic strain aging in a Ni–Co-based superalloy. Scripta Mater. 2014;87(1):37–40.

[52] Yilmaz A. The Portevin–Le Chatelier effect: a review of experimental findings. Sci. Technol. Adv. Mater. 2011;12(6):063001.

[53] Rodriguez P. Serrated plastic flow. Bull. Mater. Sci. 1984;6(4):653–63.

[54] Cottrell A. A note on the Portevin-Le Chatelier effect. The London, Edinburgh, and Dublin Philosophical Magazine and Journal of Science 1953;44(355): 829–32.

[55] Le Chatelier A. Influence du temps et de la température sur les essais au choc. La Revue de Metallurgie Paris 1909;6(8):914–7.

[56] Le Chatelier A, Portevin F. Sur un phénomène observé lors de l'essai de traction d'alliages en cours de transformation. Comptes Rendus de l'Academie des Sciences Paris 1923;176:507–10.

[57] Savart F. Recherches sur les vibrations longitudinales. Ann. Chim. 1837;65:337–402.

[58] Mason A. Sur l'elasticite des corps solides. Annales de Chimie et de Physique 1841;3:451–62.

[59] A. Shibkov et al. Plastic deformation macrolocalization during serrated creep of an aluminum-magnesium Al-6 wt % Mg alloy. Technical Physics, 59(4), 508–514, 12014.

[60] Brindley B, Barnby J. Dynamic strain ageing in mild steel. Acta Metall 1966;14(12):1765–80.

[61] Fu S, et al. Two mechanisms for the normal and inverse behaviors of the critical strain for the Portevin-Le Chatelier effect. Acta Mater 2012;60(19):6650–6.

[62] Carrol R, et al. Experiments and model for serration statistics in low-entropy, medium-entropy and high-entropy alloys. Nature Scientific Reports 2015;5: 16997.

[63] Koyama M, et al. TWIP effect and plastic instability condition in an Fe-Mn-C austenitic steel. ISIJ Int. 2013;53(2):323–9.

[64] Samuel K, et al. Serrated yielding in AISI 316 stainless steel. Acta Metall 1988;36(8):2323–7.

[65] Hong S, et al. Mechanism of dynamic strain aging and characterization of its effect on the low-cycle fatigue behavior in type 316L stainless steel. J. Nucl. Mater. 2005;340(2):307–14.

[66] Hale C, Weaver M. Activation energy calculations for discontinuous yielding in Inconel 718SPF. Materials Science and Engineering: A 2001;300(1–2):153–64.

[67] Max B, et al. A re-examination of the Portevin-Le Chatelier effect in alloy 718 in connection with oxidation assisted intergranular cracking. Metallurgical and Materials Transactions A 2014;45(12). 5431–5411.

[68] Z. Basinski. The instability of plastic flow of metals at very low temperatures. Proceedings of the Royal Society of London. Series A. Mathematical and Physical Sciences, 240(1221), 229–242, 1957.

[69] Lebyodkin M, Bobrov V. Role of dynamical processes at discontinuous deformation of aluminium. Solid State Phenom. 1993;35:411–6.

[70] Brindley B, Barnby J. The effect of nitrogen content on dynamic strain-ageing in mild steel. Acta Metall 1968;16(1):41–4.

[71] Pink E, Kumar S. Patterns of serrated flow in a low-carbon steel. Materials Science and Engineering: A 1995;201(1):58–64.

[72] Nakada Y, Keh A. Serrated flow in Ni-C alloys. Acta Metall 1970;18(4):437–43.

[73] Blakemore J. The Portevin-le Chatelier effect in carburized nickel alloys. Metallurgical and Materials Transactions B 1970;1(5):1281–5.

[74] Dastur Y, Leslie W. Mechanism of work hardening in Hadfield manganese steel. Metall. Trans. A 1980;12:749–59.

[75] Dudova N, et al. Short-range order and mechanical properties of nichrome. Dokl. Phys. 2009;54(2):77–9.

[76] Dudova N, et al. Manifestation of the Portevin-Le Chatelier effect in the Kh20N80 alloy. Zeitschrift für Physik 2008;105(1):98–104.

[77] Han G, et al. Portevin–Le Chatelier effect in Nimonic 263 superalloy. Acta Metall Sin 2015;28(5):542–9.

[78] Cui C, et al. Dynamic strain aging in a new Ni–Co base superalloy. Scripta Mater. 2011;64(6):502–5.

[79] Nalawade S, et al. The influence of aging on the serrated yielding phenomena in a nickel-base superalloy. Scripta Mater. 2008;59(9):991–4.

[80] Lin Y, et al. Influences of initial microstructures on Portevin-Le Chatelier effect and mechanical properties of a Ni–Fe–Cr–Base Superalloy. Adv. Eng. Mater. 2018;20:1800234.

[81] Tian C, et al. Dynamic strain aging in a newly developed Ni Co-base superalloy with low stacking fault energy. Journal of Materials Science & Technology 2013;29(9):873–8.

[82] S. Nalawade et al. Serrated yielding in alloy 718. In: 7th International Symposium of Superalloy 718 and Derivatives, TMS, pages 809–823, 2010.

[83] Fu S, et al. The mechanism of critical strain of serrated yielding in strain rate domain. Chin. Phys. Lett. 2016;33(2):026201.

[84] Chihab K, et al. Serrated yielding due to Portevin-Le Chatelier effect in commercial Al-Mg alloys. Annales de Chimie Science des Materiaux 2002;27(1):69–75.

[85] Wen W, et al. The effect of Mg precipitation on the mechanical properties of 5xxx aluminum alloys. Materials Science and Engineering: A 2005;392(1–1): 136–44.

[86] Meng L, et al. Serrated flow behavior in AL6XN austenitic stainless steel. J. Nucl. Mater. 2009;394(1):34–8.

[87] Meng J, et al. Dynamic strain ageing in a twin-induced plasticity steel. Mater. Sci. Forum 2013;750:88–91.

[88] Fernandez-Zelaia P, et al. The Portevin-Le Chatelier effect in the Ni-based superalloy IN100. Metallurgical and Materials Transactions A 2015;46(12): 5596–609.
[89] Sharghi-Moshtaghin R, Asgari S. The characteristics of serrated flow in superalloy IN738LC. Materials Science and Engineering: A 2008;486(1–2):376–80.
[90] Lloyd D, et al. Serrated yielding in a super alloy (40Co-38Ni-17Cr-5Ti). Acta Metall 1975;23(1):93–100.
[91] Roy A, et al. Dynamic strain ageing of an austenitic superalloy- temperature and strain rate effects. Materials Science and Engineering: A 2008;474(1–2): 363–70.
[92] Han F, et al. The tensile behavior of GH3535 superalloy at elevated temperature. Mater. Chem. Phys. 2016;182:22–31.
[93] Huron E. Serrated yielding in a nickel-base superalloy. Superalloys 1992;1992:675–84.
[94] Ter-Ovanessian B, et al. Influence of interstitials content on the sensitivity of alloy 718 to oxidation assisted intergranular fracture. Mater. Sci. Forum 2008; 595–598:951–8.
[95] Han G, et al. Direct evidence for Suzuki segregation and Cottrell pinning in MP159 superalloy obtained by FEG(S)TEM/EDX. Acta Mater 2004;51(10):2731–42.
[96] Jensen R, Tien J. Temperature and strain rate dependence of the stress-strain behaviour in a nickel-base superalloy. Metall. Trans. A 1985;16:1049–68.
[97] Valsan M, et al. Effect of strain rate on the high-temperature low-cycle fatigue properties of a Nimonic PE16 superalloy. Metall. Trans. A 1994;25(1):159–71.
[98] Rezende M, et al. Oxidation assisted intergranular cracking under loading at dynamic strain aging temperatures in Inconel 718 superalloy. J. Alloy. Compd. 2015;643(1):256–9.
[99] Worthington P, Brindley B. Serrated yielding in substitutional alloys. The Philosophical Magazine: A Journal of Theoretical Experimental and Applied Physics 1969;19(162):1175–8.
[100] C. Schwink and A. Nortmann. The present experimental knowledge of dynamic strain ageing in binary f.c.c. solid solutions. Materials Science and Engineering: A, 234-236:1–7, 1997.
[101] Pink E, Grinberg A. Stress drops in serrated flow curves of Al5Mg. Acta Metall 1982;30(12):2153–60.
[102] Pink E, Webernig W. Precipitation during serrated flow in AlZn5Mg1. Acta Metall 1987;35(1):127–32.
[103] Zhang S, et al. The morphology of Portevin–Le Chatelier bands: finite element simulation for Al–Mg–Si. Acta Mater 2001;49(6):1087–94.
[104] Mogucheva A, et al. Effect of Grain Refinement on Jerky Flow in an Al-Mg-Sc Alloy. Metallurgical and Materials Transactions A 2016;47:2093–106.
[105] Yuzbekova D, et al. Effect of microstructure on continuous propagation of the Portevine Le Chatelier deformation band. Int. J. Plast 2017;96:210–26.
[106] Nageesha A, et al. Dynamic strain ageing in Inconel alloy 783 under tension and low cycle fatigue. Mater. Sci. Eng., A 2012;546:34–9.
[107] Sakthivel T, et al. Effect of temperature and strain rate on serrated flow behaviour of Hastelloy X. Mater. Sci. Eng., A 2012;534:580–7.
[108] Wang X, et al. On the γ′ precipitates of the normal and inverse Portevin-Le Chatelier effect in a wrought Ni-base superalloy. J. Mater. Sci. Technol. 2019;35(1): 84–7.
[109] Shankar V, et al. Effects of temperature and strain rate on tensile properties and activation energy for dynamic strain aging in Alloy 625. Metallurgical and Materials Transactions A 2004;35(10):3129–39.
[110] Weaver M, Hale C. Effects of precipitation on serrated yielding in Inconel 718. Superalloys 2001;2001:421–32.
[111] Russell B. Repeated yielding in tin bronze alloys. The Philosophical Magazine: A Journal of Theoretical Experimental and Applied Physics 1963;8(88):615–30.
[112] McCormick P. The Portevin-Le Chatelier effect in an Al-Mg-Si alloy. Acta Metall 1971;19(5):463–71.
[113] Saha G, et al. Portevin-Le Chatelier effect in an Al-Mn alloy I: serration characteristics. Materials Science and Engineering 1984;62(2):187–96.
[114] Chen M, et al. Analysis on the amplitude of serrated flow associated with the Portevin-Le Chatelier effect of substitutional fcc alloys. Metallurgical and Materials Transactions A 1996;27(6):1691–4.
[115] Kim I, Chaturvedi C. Serrated flow in Al-5 wt.% Mg alloy. Materials Science and Engineering 1979;37:165–72.
[116] Klose F, et al. Analysis of Portevin-Le Chatelier serrations of type B in Al–Mg. Materials Science and Engineering: A 2004;369(1):76–81.
[117] Kim I, Chaturvedi C. Serrated flow in Inconel 625. Transactions of the Japan Institute of Metals 1987;28(3):205–12.
[118] Chihab K, et al. The kinetics of the Portevin-Le Chatelier bands in an Al-5at%Mg alloy. Scr. Metall. 1987;21(2):203–8.
[119] Lebyodkin M, et al. Statistical behaviour and strain localization patterns in the Portevin-Le Chatelier effect. Acta Mater 1996;44(11). 4531-4531.
[120] Maj P, et al. Statistical analysis of the Portevin–Le Chatelier effect in Inconel 718 at high temperature. Materials Science and Engineering: A 2014;619:158–64.
[121] Maj P, et al. Microstructure and stress-strain analysis of the dynamic strain aging in Inconel 625 at high temperature. Met. Mater. Int. 2017;23(1):54–67.
[122] Lebedkina T, Lebyodkin M. Effect of deformation geometry on the intermittent plastic flow associated with the Portevin–Le Chatelier effect. Acta Mater 2008; 56(19):5567–74.
[123] Cai Y, et al. Influence of γ′ precipitates on Portevin–Le Chatelier effect of Ni-based superalloys. Mater. Sci. Eng., A 2015;638:314–21.
[124] Böhlke T, et al. Geometrically non-linear modeling of the Portevin–Le Chatelier effect. Comput. Mater. Sci. 2009;44:1076–88.
[125] Lebyodkin M, et al. Statistics of the catastrophic slip events in the Portevin-Le Chatelier effect. Phys. Rev. Lett. 1995;74(23):4758–61.
[126] Lebyodkin M, et al. Spatio-temporal dynamics of the Portevin–Le Chatelier effect: experiment and modelling. Acta Mater 2000;48(10):2529–41.
[127] Ananthakrishna G, et al. Crossover from chaotic to self-organized critical dynamics in jerky flow of single crystals. Phys. Rev. E 1999;60(5):5455–61.
[128] Bharathi M, et al. The hidden order behind jerky flow. Acta Mater 2002;50(11):2813–24.
[129] Bharathi M, Ananthakrishna G. Chaotic and power law states in the Portevin-Le Chatelier effect. Europhys. Lett. 2002;60(2):234–40.
[130] Bak P, et al. Self-organized criticality. Phys. Rev. A 1988;38(1):364–74.
[131] Ananthakrishna G, et al. On the existence of chaos in jerky flow. Scripta Metallurgica et Materialia. 1995;32(11):1731–7.
[132] Ananthakrishna G, et al. Chaos and the jerky flow in Al-Mg polycrystals. Mater. Sci. Eng., A 1997;234:314–7.
[133] Noronha S, et al. Chaos in the Portevin-Le Chatelier Effect. International Journal of Bifurcation and Chaos 1997;7(11):2577–86.
[134] Weiss J, Grasso J. Acoustic Emission in Single Crystals of Ice. J. Phys. Chem. B 1997;101:6113–7.
[135] Shashkov I, et al. Multiscale study of acoustic emission during smooth and jerky flow in an AlMg alloy. Acta Mater 2012;60(19):6842–50.
[136] Bougherira Y, et al. The intermittency of plasticity in an Al3%Mg alloy. J. Phys: Conf. Ser. 2010;240:012009.
[137] Dimiduk D, et al. Scale-Free Intermittent Flow in Crystal Plasticity. Science 2006;312(5777):1188–90.
[138] Zaiser M. Scale invariance in plastic flow of crystalline solids. Adv. Phys. 2006;55:185–245.
[139] Lebyodkin M, et al. On the similarity of plastic flow processes during smooth and jerky flow: statistical analysis. Acta Mater 2012;60(9):3729–40.
[140] Lebyodkin M, et al. Role of superposition of dislocation avalanches in the statistics of acoustic emission during plastic deformation. Phys. Rev. E 2013;88: 042402.
[141] McCormick P, et al. Propagative instabilities: an experimental view. Scr. Metall. Mater. 1993;29(9):1159–64.
[142] Lüders W. Über die äusserund der elasticität an stahlartigen eisenstäben unter sthalstäben. und über eine beim biegen solcher stäbe beobachtete molecularbewegung. Dingler's Polytechnic Journal 1860;155:18–22.
[143] Brink S, et al. The influence of specimen dimensions and machine stiffness on the Portevin-Le Chatelier effect in an Al–Cu alloy. Phys. Status Solidi A 1977;41 (2):513–21.
[144] Jiang Z, et al. Spatial characteristics of the Portevin-Le Chatelier deformation bands in Al-4at%Cu polycrystals. Materials Science and Engineering: A 2005;403 (1):154–64.
[145] Shabadi R, et al. Characterisation of PLC band parameters using laser speckle technique. Materials Science and Engineering: A 2004;364(1):140–50.
[146] Ait-Amokhtar H, et al. Kinematics fields and spatial activity of Portevin–Le Chatelier bands using the digital image correlation method. Acta Mater 2006;54 (16):4365–71.
[147] Ranc N, Wagner D. Some aspects of Portevin-Le Chatelier plastic instabilities investigated by infrared pyrometry. Materials Science and Engineering: A 2005; 394(1):87–95.
[148] Ranc N, Wagner D. Experimental study by pyrometry of Portevin-Le Chatelier plastic instabilities-Type A to Type B transition. Materials Science and Engineering: A 2008;474(1):188–96.

[149] Zielke R, et al. Thermographic study of nucleation and propagation of Portevin-Le Chatelier bands. Quantitative InfraRed Thermography Journal 2008;5(2):231–48.
[150] Fu X, et al. Deformation measurements of three types of Portevin–Le Chatelier bands. Chin. Phys. 2006;15(10):2378–84.
[151] T. Makinen. Portevin–Le Chatelier effect in an aluminum alloy. PhD Thesis, Aalto University, 2016.
[152] Cai Y, et al. The influence of specimen thickness on the Lüders effect of a 5456 Al-Based alloy: experimental observations. Metals 2016;6(120):1–12.
[153] Weidner A. Plastic deformation and strain localizations. Cham: Springer International Publishing; 2020. p. 7–45.
[154] Rizzi E, Hähner P. On the Portevin–Le Chatelier effect: theoretical modeling and numerical results. Int. J. Plast 2004;20(1):121–65.
[155] Tong W, et al. Time-resolved strain mapping measurements of individual Portevin–Le Chatelier deformation bands. Scripta Mater. 2005;53:87–92.
[156] McCormick P, Ling P. Numerical Modelling of The Portevin Le Chatelier Effect. Acta Metall Mater 1995;43(5):1967–77.
[157] Xiang G, et al. Time-resolved deformation measurements of the Portevin–Le Chatelier bands. Scripta Mater. 2007;56:721–4.
[158] Zhemchuzhnikova D, et al. Interrelation between the Portevin Le-Chatelier effect and necking in AlMg alloys. Int. J. Plast 2018;110:95–109.
[159] Ait-Amokhtar H, Fressengeas C. Crossover from continuous to discontinuous propagation in the Portevin-Le Chatelier effect. Acta Mater 2010;58:1342–9.
[160] Louche H, et al. Thermal observations associated with the Portevin–Le Chatelier effect in an Al–Mg alloy. Materials Science and Engineering: A 2005;404:188–96.
[161] Min J, et al. Effect of strain rate on spatio-temporal behavior of Portevin–Le Chatelier bands in a twinning induced plasticity steel. Mech. Mater. 2014;68:164–75.
[162] Klose F, et al. Investigation of the Portevin-Le Chatelier effect in Al-3wt.%Mg alloys by strain-rate and stress-rate controlled tensile tests. Materials Science and Engineering: A 2004;387:93–7.
[163] Hähner P, et al. Spatiotemporal analysis of Portevin-Le Chatelier deformation bands: theory, simulation, and experiment. Phys. Rev. B 2002;65(13):134109.
[164] Ziegenbein A, et al. Correlation of temporal instabilities and spatial localization during Portevin-Le Chatelier deformation of Cu-10 at.% Al and Cu-15 at.% Al. Comput. Mater. Sci. 2000;19(1):27–34.
[165] Hähner P, et al. Observation and modelling of propagating Portevin-Le Chatelier deformation bands in Cu-15 at.% Al polycrystals. Philos. Mag. A 2001;81(6):1633–49.
[166] Westrum S, Wijler A. Determination of the characteristics of Portevin-Le Chatelier bands in Au(14at.%Cu). Acta Metall 1973;21:1079–86.
[167] Klose F, et al. Portevin-Le Chatelier effect in strain and stress controlled tensile tests. Comput. Mater. Sci. 2003;26:80–6.
[168] Kang J, et al. Effect of Mg content on Portevin-Le Chatelier band strain in Al-Mg sheet alloys. Philos. Mag. Lett. 2012;92(11):647–55.
[169] Lan P, Zhang J. Serrated flow and dynamic strain aging in Fe-Mn-C TWIP steel. Metallurgical and Materials Transactions A 2017;49:147–61.
[170] Renard K, et al. Characterisation of the Portevin-Le Chatelier effect affecting an austenitic TWIP steel based on digital image correlation. Mater. Sci. Eng., A 2010;527:2969–77.
[171] Zavattieri P, et al. Spatio-temporal characteristics of the Portevin–Le Chatelier effect in austenitic steel with twinning induced plasticity. Int. J. Plast 2009;25(12):2298–330.
[172] Jiang H, et al. Experimental investigations on kinetics of Portevin-Le Chatelier effect in Al-4wt.%Cu alloys. J. Alloy. Compd. 2007;428(1):151–6.
[173] W. Song and J. Housten. Local deformation and Mn-C short-range ordering in a high-Mn Fe-18Mn-0.6C steel. Metals, 8(5):292, 2018.
[174] T. Sasaki et al. Observation of grain-size effect in serration of aluminum alloy. Advancement of Optical Methods in Experimental Mechanics, Volume 3: Proceedings of the 2014 Annual Conference on Experimental and Applied Mechanics, pages 109–115, 2014.
[175] Fellner M, et al. A comparison of the Portevin-Le Chatelier effect in constant-strain-rate and constant-stress-rate tests. Materials Science and Engineering: A 1991;137(1):157–61.
[176] Hong K, Nam S. Kinetics of serrated flow in terms of dislocation interaction. Acta Metall 1989;37(1):31–4.
[177] Casarotto L, et al. Propagation of deformation bands investigated by laser scanning extensometry. Comput. Mater. Sci. 2003;26:210–8.
[178] Lebyodkin M, et al. Kinematics of formation and cessation of type B deformation bands during the Portevin-Le Chatelier effect in an AlMg alloy. Results in Physics 2019;12:867–9.
[179] Fournier L, et al. Oxidation induced intergranular cracking and Portevi-Le Chatelier effect in nickel base superalloy 718. Materials Science and Engineering: A 2001;316(1–2):166–73.
[180] Chatterjee A, et al. Investigation of the dynamic strain aging and mechanical properties in alloy-625 with different microstructures. Metallurgical and Materials Transactions A 2014;46(3):1097–107.
[181] Prasad K, et al. Tensile deformation behaviour of forged disc of IN718 superalloy at 650°C. Materials and design 2010;31:4502–7.
[182] Swaminanthan B, et al. Investigation using digital image correlation of Portevin-Le Chatelier effect in Hastelloy X under thermo-mechanical loading. Int. J. Plast 2015;64:177–92.
[183] B. Swaminathan. Thermo-mechanical response and plastic deformation behaviour of Hastelloy x at elevated temperatures- role of dynamic strain ageing. Master's Thesis, University of Illinois, 2012.
[184] Cai Y, et al. Influence of γ′ precipitates on the critical strain and localized deformation of serrated flow in Ni-based superalloys. J. Alloy. Compd. 2017;690:707–15.
[185] H. Jones and C. Feng. Deformation band velocities and local strain rates in a Ni-Cr-Fe alloy (Inconel). MRS Proceedings, 683, 2001.
[186] Liu Y, et al. Experimental investigation of a Portevin-Le Chatelier band in Ni-Co-based superalloys in relation to γ′ precipitates at 500°C. Journal of Materials Science & Technology 2020;49:35–41.
[187] Lebyodkin M, et al. Scaling in the Local Strain-Rate Field during Jerky Flow in an Al-3%Mg Alloy. Metals 2020;10:134.
[188] Weiss J, et al. Evidence for universal intermittent crystal plasticity from acoustic emission and high-resolution extensometry experiments. Physical Review B 2007;76:224110.
[189] Coër J, et al. Piobert-Lüders plateau and Portevin–Le Chatelier effect in an Al–Mg alloy in simple shear. Mech. Res. Commun. 2013;48:1–7.
[190] Manach P, et al. Kinematics of Portevin–Le Chatelier bands in simple shear. Int. J. Plast 2014;58:66–83.
[191] Bernard C, et al. Influence of Portevin-Le Chatelier Effect on Shear Strain Path Reversal in an Al-Mg Alloy at Room and High Temperatures. Exp. Mech. 2017;57:405–15.
[192] Mansouri L, et al. Investigation of Portevin-Le Chatelier effect during Erichsen test. Int.J. Mater. Form. 2020;13:687–97.
[193] Min J, et al. Spatio-temporal characteristics of plastic instability in AA5182-O during biaxial deformation. Mater. Des. 2015;83:786–94.
[194] Cieslar M, et al. Portevin–Le Chatelier effect in biaxially strained Al–Fe–Si foils. Scripta Mater. 2003;48:1105–10.
[195] Hou Y, et al. Plastic instabilities in AA5754-O under various stress states. IOP Conference Series: Materials Science and Engineering 2018;418:012050.
[196] Berk Aytuna O, Efe M. Investigation of Portevin-LeChatelier Bands in 5754 Aluminum Alloy under Various Strain Paths. Proc Struct Integ 2019;21:120–9.
[197] Le Cam J, et al. Calorimetric analysis of Portevin-Le Chatelier bands under equibiaxial loading conditions in Al–Mg alloys: Kinematics and mechanical dissipation. Mech. Mater. 2017;105:80–8.
[198] Sene N, et al. Experimental study of Portevin–Le Chatelier bands on tensile and plane strain tensile tests. Archives of Civil and Mechanical Engineering 2018;18:94–102.
[199] Seymen Y, et al. Large Strain and Small-Scale Biaxial Testing of Sheet Metals. Exp. Mech. 2016;56:1519–30.
[200] Considere A. L'emploi du fer et l'acier dan les constructions. Annales des Ponts et Chaussées 1885;1(9):574–775.
[201] Kubin L, Estrin Y. Strain nonuniformities and plastic instabilities. Rev. Phys. Appl. 1988;23(4):573–83.
[202] Estrin Y. Classification of plastic instabilities by linear stability analysis. Solid State Phenom. 1988;3:417–28.
[203] Estrin Y. Plastic instabilities: phenomenology and theory. Mater. Sci. Eng., A 1991;137:125–34.
[204] Mesarovic S. Dynamic strain aging and plastic instabilities. Journal of Mechanical Physics of Solids 1995;43(5):671–700.
[205] Kubin L, Estrin Y. The Portevin-Le Chatelier Effect in Deformation with Constant Stress Rate. Acta Metall 1985;33(3):397–407.
[206] Frost H, Ashby M. Deformation mechanism maps. Pergamon Press; 1982.

[207] Alexander H, Haasen P. Dislocations in nonmetals. Annu. Rev. Mater. Sci. 1972;2(1):291–312.
[208] Boas W, Schmid B. Über die dehnung von cadmiumkristallen. Zeitschrift für Physik 1929;54(1–2):16–45.
[209] Cottrell A. Distribution of solute atoms round a slow dislocation. Proceedings of the Royal Society of London. Series A. Mathematical and Physical Sciences 1949;199(1056):104–14.
[210] Kubin L, et al. On static strain ageing. Acta Metall Mater 1992;40(5):1037–44.
[211] Wilde J, et al. Three-dimensional atomic-scale mapping of a Cottrell atmosphere around a dislocation in iron. Scripta Mater. 2000;43:39–48.
[212] Birnbaum H, et al. The effect of diffusivity gradients on diffusion to dislocations. Phil Mag 1970;23(184):847–57.
[213] Cochardt A, et al. Interaction between dislocation and interstitial atoms in body-centred cubic metals. Acta Metall 1955;3:533–7.
[214] Chiba A, et al. High work-hardening rate and deformation twinning of Co-Ni-based superalloy at elevated temperatures. Philos. Mag. A 1999;79(7):1533–54.
[215] Segersäll M, Moverare J. Crystallographic orientation influence on the serrated yielding behaviour of a single crystal superalloy. Materials 2013;6(2):437–44.
[216] Siegel R. Vacancy concentration in metals. J. Nucl. Mater. 1978;69:117–46.
[217] Bellini S, et al. Thermodynamic aspects in non-ideal metal membranes for hydrogen purification. Membranes 2018;8(3):82.
[218] Cottrell A. Theory of dislocations. Progress in Metal Physics 1953;4:205–64.
[219] Friedel J. Les dislocations. Gauthier-Villars; 1956.
[220] Harper S. Precipitation of carbon and nitrogen in cold-worked alpha-iron. Phys. Rev. 1951;83(4):709–12.
[221] Pitsch W. Zur ausscheidung von kohlenstoff aus übersattigter lösung in $\alpha$-eisen während der auslagerung. Archiv für das Eisenhüttenwesen 1956;27:45–54.
[222] Bullough R, Newman R. The kinetics of migration of point defects to dislocations. Rep. Prog. Phys. 1970;33:101–47.
[223] Mura T, et al. Segregation of solute atoms during strain aging. Acta Metall 1961;9:453–8.
[224] Louat N. On the theory of the Portevin-Le Chatelier effect. Scr. Metall. 1981;15(11):1167–70.
[225] Schlipf J. On the kinetics of static and dynamic strain ageing. Scr. Metall. Mater. 1994;31(7):909–14.
[226] Yoshinga H, Morozumi S. A Portevin-Le Chatelier effect expected from solute atmosphere dragging. The Philosophical Magazine: A Journal of Theoretical Experimental and Applied Physics 1971;23(186):1351–66.
[227] F. Nabarro. Mechanical effects of carbon in iron: report of a conference on the strength of solids. The Physical Society, London, 75, 1948.
[228] Cottrell A. Dislocations and plastic flow in crystals. Am. J. Phys. 1954;22(4):242–3.
[229] De Cooman B, et al. Twinning-induced plasticity (TWIP) steels. Acta Mater 2018;142:283–362.
[230] Mulford R, Kocks U. New observations on the mechanisms of dynamic strain aging and of jerky flow. Acta Metall 1979;27(7):1125–34.
[231] Clouet E, et al. Dislocation interaction with C in $\alpha$-Fe: a comparison between atomic simulations and elasticity theory. Acta Mater 2008;56(14):3450–60.
[232] Lander J, et al. Solubility and diffusion coefficient of carbon in nickel: reaction rates of nickel-carbon alloys with barium oxide. J. Appl. Phys. 1952;23(12):1305–9.
[233] Jeong H, Kim W. Strain hardening behavior and strengthening mechanism in Mg-rich Al–Mg binary alloys subjected to aging treatment. Materials Science and Engineering: A 2020;794:139862.
[234] Ananthakrishna G, Sahoo D. A model based on nonlinear oscillations to explain jumps on creep curves. Journal of Physics D: Applied Physics. 1981;14:2081–90.
[235] Hähner P. On the physics of the Portevin-Le Chatelier effect part 1: the statistics of dynamic strain ageing. Materials Science and Engineering: A 1996;207(2):208–15.
[236] Van den Beukel A. Theory of the effect of dynamic strain aging on mechanical properties. Phys. Status Solidi A 1975;30(1):197–206.
[237] Kubin L, Estrin Y. Evolution of dislocation densities and the critical conditions for the Portevin-Le Chatelier effect. Acta Metall Mater 1990;38(5):697–708.
[238] Ray S, et al. Dynamic strain ageing in type 316 stainless steel at 300 K. Scr. Metall. Mater. 1992;27(3):271–6.
[239] Venkadesan S, et al. Flow transients during strain rate jump tests in a titanium-modified austenitic stainless steel. Materials Science and Engineering: A 1992;154(1):69–74.
[240] Larsson R, Nilsson L. On the modelling of strain ageing in a metastable austenitic stainless steel. J. Mater. Process. Technol. 2012;212(1):46–58.
[241] Brink S, et al. Strain rate sensitivity and the Portevin-Le Chatelier effect in Au–Cu alloys. Phys. Status Solidi A 1975;30(2):469–77.
[242] Ren S, et al. Portevin-Le Chatelier effect triggered by complex loading paths in an Al–Cu aluminium alloy. Phil Mag 2019;99(6):659–78.
[243] Mulford R. The effect of precipitation hardening on dynamic strain aging and jerky flow. Metall. Trans. A 1979;10(7):1527–32.
[244] Zhao S, et al. Influence of severe plastic deformation on dynamic strain aging of ultrafine grained Al–Mg alloys. Acta Mater 2014;76:54–67.
[245] MacEwen S, Ramaswami B. Strain rate change transients in Al-Mg single crystals. Metallurgical Transactions 1971;2(7):1851–5.
[246] Ling C, McCormick P. Strain rate sensitivity and transient behaviour in an Al-Mg-Si alloy. Acta Metall Mater 1990;38(12):2631–5.
[247] Kobelev N, et al. Role of self-organization of dislocations in the onset and kinetics of macroscopic plastic instability. Metallurgical and Materials Transactions A 2017;48(3):965–74.
[248] McCormick P, Estrin Y. Transient flow behaviour associated with dynamic strain ageing. Scr. Metall. 1989;23:1231–4.
[249] Kocks U, Mecking H. Dislocation kinetics at not so constant structure. In: Dislocation Modelling of Physical Systems: Proceedings of the International Conference; 1981. p. 173–92.
[250] Cornet C, et al. Effects of temperature and hold time on dynamic strain aging in a nickel based superalloy. Mater. High Temp. 2014;31(3):226–32.
[251] Cao Y, et al. Influence of dynamic strain aging on the mechanical properties and microstructural evolution for alloy 800H during hot deformation. Materials Science and Engineering: A 2018;724:37–44.
[252] Stüwe H, Les P. Strain rate sensitivity of flow stress at large strains. Acta Mater 1998;46(18):6375–80.
[253] Basinski Z, et al. Transients in steady-state plastic deformation produced by changes of strain rate. The Philosophical Magazine: A Journal of Theoretical Experimental and Applied Physics 1977;36(2):255–63.
[254] Tanner A, McDowell D. Deformation, temperature and strain rate sequence experiments on OFHC Cu. Int. J. Plast 1999;15(4):375–99.
[255] Jackson M, et al. Effect of initial microstructure on plastic flow behaviour during isothermal forging of Ti–10V–2Fe–3Al. Materials Science and Engineering: A 2009;501(1):248–54.
[256] van Liempt P, Sietsma J. A revised criterion for the Portevin–Le Chatelier effect based on the strain-rate sensitivity of the work-hardening rate. Metallurgical and Materials Transactions A 2011;42(13):4008–14.
[257] Louchet F. A classification of flow-stress anomalies, and the specific role of strain rate sensitivity. J. Phys. IV 1996;6:189.
[258] Wielke B. Dislocation dynamics during rate changes. Acta Metall 1978;26(1):103–13.
[259] Ananthakrishna G, Valsakumar M. Repeated yield drop phenomenon: a temporal dissipative structure. Journal of Physics D: Applied Physics. 1982;15:171–5.
[260] Nortmann A, Schwink C. On the superposition of the effects of dynamic strain ageing and a varying mobile dislocation density- strain rate change experiments on CuMn single crystals. Scr. Metall. Mater. 1995;33(3):369–75.
[261] Zhang F, et al. Finite element implementation of a kinetic model of dynamic strain aging in aluminum–magnesium alloys. Int. J. Numer. Meth. Eng. 2010;86(1):70–92.
[262] Cai M, et al. Strain rate and temperature effects on the critical strain for Portevin–Le Chatelier effect. Materials Science and Engineering: A 2010;527(20):5175–80.
[263] Hähner P, Rizzi E. On the kinematics of Portevin-Le Chatelier bands: theoretical and numerical modelling. Acta Mater 2003;51(12):3385–97.
[264] Lebedkina T, et al. Onset of the Portevin-Le Chatelier effect: role of synchronization of dislocations. Mater. Sci. Forum 2014;783:198–203.
[265] Hähner P. On the critical conditions of the Portevin-Le Chatelier effect. Acta Mater 1997;45(9):3695–707.
[266] Fressengeas C, et al. Dynamic strain aging: a coupled dislocation-solute dynamic model. Mater. Sci. Eng., A 2005;400:226–30.
[267] Soare M, Curtin W. Single-mechanism rate theory for dynamic strain aging in fcc metals. Acta Mater 2008;56(15):4091–101.
[268] Soare M, Curtin W. Solute strengthening of both mobile and forest dislocations: the origin of dynamic strain aging in fcc metals. Acta Mater 2008;56(15):4046–61.

[269] Ananthakrishna G. Current theoretical approaches to collective behaviour of dislocations. Physical Reports 2007;440:113–259.

[270] Hähner P. On the physics of the Portevin-Le Chatelier effect part 2: from microscopic to macroscopic behaviour. Materials Science and Engineering: A 1996; 207(2):216–23.

[271] Mazière M, Dierke H. Investigations on the Portevin–Le Chatelier critical strain in an aluminum alloy. Comput. Mater. Sci. 2012;52:68–72.

[272] Xu J, et al. Dynamic strain ageing in an AlMg alloy at different strain rates and temperatures: Experiments and constitutive modelling. Int. J. Plast 2022;151: 103215.

[273] Van Den Beukel A, Kocks U. The strain dependence of static and dynamic strain-aging. Acta Metall 1982;30(5):1027–34.

[274] Kocks U, et al. Strain aging and strain hardening in Ni-C alloys. Acta Metall 1985;33(4):623–38.

[275] Charnock W. The initiation of serrated yielding at elevated temperatures. The Philosophical Magazine: A Journal of Theoretical Experimental and Applied Physics 1969;20(164):427–32.

[276] Zhou P, et al. Using novel strain aging kinetics models to determine the effect of solution temperature on critical strain of Al-Zn-Mg-Cu alloy. J. Alloy. Compd. 2020;838:155647.

[277] Wang W, et al. The mechanism of critical strain and serration type of the serrated flow in Mg-Nd-Zn alloy. Mater. Sci. Eng., A 2016;649:214–21.

[278] Hayes R, Hayes W. On the mechanism of delayed discontinuous plastic flow in an age-hardened nickel alloy. Acta Metall 1982;30(7):1295–301.

[279] Estrin Y, Kubin L. Collective dislocation behaviour in dilute alloys and the Portevin-Le Chatelier effect. Journal of the Mechanical Behavior of Materials 1989;2 (3–4):255–92.

[280] Chen M, et al. Vacancy concentration in strain ageing of substitutional f c c alloys. J. Mater. Sci. 1993;28(12):3329–34.

[281] Kubin L. Strain and strain rate softening instabilities: length scales and spatial couplings. Key Eng. Mater. 1995;97:219–34.

[282] Kubin L, et al. Collective behaviour of dislocations in plasticity. Dislocations in Solids 2002;11:101–92.

[283] Csikor F, et al. Dislocation avalanches, strain bursts and the problem of plastic forming at the micrometer scale. Science 2007;318:251–4.

[284] Lebedkina T, et al. Correlation versus randomization of jerky flow in an AlMgScZr alloy using acoustic emission. Phys. Rev. E 2018;97:013001.

[285] Lebedkina T, et al. Crossover in the scale-free statistics of acoustic emission associated with the Portevin–Le Chatelier instability. Scripta Mater. 2018;148: 47–50.

[286] Perez C, et al. On Self-Organized Criticality and Synchronization in Lattice Models of Coupled Dynamical Systems. Int. J. Mod. Phys. B 1996;10(10):1111–51.

[287] Schwab R, Ruff V. On the nature of the yield point phenomenon. Acta Mater 2009;61(1798–1808).

[288] Hähner P. Modelling the spatiotemporal aspects of the Portevin-Le Chatelier effect. Materials Science and Engineering: A 1993;164(1):23–34.

[289] Bharathi M, et al. A dynamical model for the Portevin-Le Chatelier bands. Scripta Mater. 2003;48:1355–60.

[290] Zaiser M, Hähner P. Oscillatory modes of plastic deformation: theoretical concepts. Physics Status Solidi B 1997;199:267.

[291] Eshelby J. Elastic inclusions and inhomogeneities. Progress in Solid Mechanics 1961;9(1):67.

[292] Jiang H, et al. Three types of Portevin-Le Chatelier Effects: Experiment and Modelling. Acta Mater 2007;55:2219–28.

[293] Kok S, et al. Spatial coupling in jerky flow using polycrystal plasticity. Acta Mater 2003;51:3651–62.

[294] Dahmen K, et al. Micromechanical model for deformation in solids with universal predictions for stress-strain curves. Phys. Rev. Lett. 2009;102(175501).

[295] Dahmen K, et al. A simple analytic theory for the statistics of avalanches in sheared materials. Nat. Phys. 2011;7:554–7.

[296] Antonaglia J, et al. Temperature effects on deformation and serration behaviour of High-Entropy Alloys (HEAs). The London, Edinburgh, and Dublin Philosophical Magazine and Journal of Science 2014;66(10):2002–8.

[297] McFaul L, et al. Force oscillations distort avalanche shapes. Materials Research Letters 2019;7(12):496–502.

[298] L. McFaul et al. Temporal properties of avalanche dynamics. PhD Thesis, University of Illinois, 2019.

[299] Brechet Y, Estrin Y. On the influence of precipitation on the Portevin-Le Chatelier effect. Acta Metall Mater 1995;43(3):955–63.

[300] Brechet Y, Estrin Y. Pseudo-Portevin-Le Chatelier effect in ordered alloys. Scripta Mater. 1996;35(2):217–23.

[301] Zaiser M, Hähner P. A unified description of strain-rate softening instabilities. Materials Science and Engineering: A 1997;238(2):399–406.

[302] Cook R, et al. Stick-slip during fibre pull-out. Scr. Metall. 1989;23.

[303] Pink E. The effect of precipitates on characteristics of serrated flow in AlZn5Mg1. Acta Metall 1989;37(7):1773–81.

[304] Zambo S, Wert J. Effect of Li concentration and a Mg addition on serrated flow in Al-Li alloys. Scr. Metall. Mater. 1993;29(1):1523–8.

[305] Brechet Y, Estrin Y. On a pseudo Portevin-Le Chatelier effect. Scr. Metall. Mater. 1994;31(2):185–90.

[306] Brechet Y, Estrin Y. On the relations between Portevin-Le Chatelier plastic instabilities and precipitation. Key Eng. Mater. 1995;97:235–50.

[307] Pink E, Krol J. Precipitation and serrated flow in AlZn10. Acta Metall Mater 1995;43(6):2351–7.

[308] Chmelik F, et al. Mechanisms of serrated flow in aluminium alloys with precipitates investigated by acoustic emission. Acta Mater 1998;46(12):4435–42.

[309] Thevenet D, et al. The effect of precipitation on the Portevin-Le Chatelier effect in an Al–Zn–Mg–Cu alloy. Materials Science and Engineering: A 1999;266(1): 175–82.

[310] Riley D, McCormick P. The effect of precipitation hardening on the portevin-le chatelier effect in an al-mg-si alloy. Acta Metall 1976;25:181–5.

[311] Kumar S. Inverse behaviour of the onset strain of serrated flow. Scr. Metall. Mater. 1994;33(1):81–6.

[312] Ovri H, Lilleodden E. New insights into plastic instability in precipitation strengthened Al–Li alloys. Acta Mater 2015;89(1):88–97.

[313] L. Owen. The analysis of local structural effects in alloys using total scattering and reverse Monte Carlo techniques. PhD Thesis, University of Cambridge, 2018.

[314] Hall E. Yield point phenomena in metals and alloys. 1 edition. US: Springer; 1970.

[315] Kang J, et al. Impact of short-range ordering on yield strength of high manganese austenitic steels. Materials Science and Engineering: A 2014;614:122–8.

[316] Zhang R, et al. Short-range Order and its Impact on the CrCoNi medium-entropy Alloy. Nature 2020;581:283–7.

[317] Zhang R, et al. Direct Imaging of Short-range Order and its Impact on Deformation in Ti-6Al. Science Advances 2019;5:2799.

[318] Owen L, et al. A new approach to the analysis of short-range order in alloys using total scattering. Acta Mater 2016;115:155–66.

[319] Thomas H. Über widerstandslegierungen. The Physics of Metals and Metallography 1951;129:219–32.

[320] Rose K, Glover S. A study of strain ageing in austenite. Acta Metall 1966;14:1505–16.

[321] Nakada Y, Keh A. Kinetics of Snoek ordering and Cottrell atmosphere formation in Fe-N single crystals. Acta Metall 1967;15(5):879–83.

[322] Schoeck G, Seeger A. The flow stress of iron and its dependence on impurities. Acta Metall 1959;7(7):469–77.

[323] Snoek J. Effect of small quantities of carbon and nitrogen on the elastic and plastic properties of iron. Physica 1941;8(7):711–3.

[324] Wilson D, Russell B. Stress induced ordering and strain-ageing in low carbon steels. Acta Metall 1959;7(1):628–31.

[325] Cribb W, Reed-Hill R. The initial development of a yield point due to carbon in nickel 200 during static strain aging. Metall. Trans. A 1978;9(7):887–90.

[326] Garruchet S, Perez M. Modelling the carbon Snoek peak in ferrite: coupling molecular dynamics and kinetic Monte-Carlo simulations. Comput. Mater. Sci. 2008;43(2):6286–92.

[327] Owen W, Grujicic M. Strain aging of austenitic Hadfield manganese steel. Acta Mater 1998;47(1):111–26.

[328] Jin J, Lee Y. Effects of Al on microstructure and tensile properties of C-bearing high Mn TWIP steel. Acta Mater 2012;60(4):1680–8.

[329] Lee S, et al. Effect of nitrogen on the critical strain for dynamic strain aging in high-manganese twinning-induced plasticity steel. Scripta Mater. 2011;65(6): 528–31.

[330] Peng X, et al. Stacking fault energy and tensile deformation behavior of high-carbon twinning-induced plasticity steels: effect of Cu addition. Mater. Des. 2013; 43:518–23.

[331] Koyama M, et al. Overview of dynamic strain aging and associated phenomena in Fe-Mn-C austenitic steels. ISIJ Int. 2018;58(8):1383–95.

[332] Kozlowska A, et al. Explanation of the PLC effect in advanced high-strength medium-Mn steels. A review. Materials (Basel) 2019;12(24):4175.

[333] Song W, et al. On the Mn–C short-range ordering in a high-strength high-ductility steel: small angle neutron scattering and ab initio investigation. Metals 2018; 8(1):44.

[334] Oh S, et al. The mechanism of dynamic strain aging for Type A serrations in tensile flow curves of F-18Mn-0.55C (wt.%) twinning-induced plasticity steel. Acta Mater 2020;188:366–75.

[335] A. Hannon. Neutron diffraction, theory. 2017.
[336] Behnood N, Evans J. Plastic deformation and the flow stress of aluminium-lithium alloys. Acta Metall 1989;37(2):687–95.
[337] Aboulfadl H, et al. Dynamic strain aging studied at the atomic scale. Acta Mater 2015;86:34–42.
[338] Popov L, et al. Configuration of antiphase boundaries in ordered AuCu3-type solid solutions. Phys. Status Solidi B 1966;13(2):569–75.
[339] Morris D, et al. Discontinuous yielding and dislocation locking in Cu3Au. Acta Metall 1974;22(7):801–11.
[340] Cuniberti A, Niewczas M. Effect of temperature on superdislocation dissociation in Cu–Zn–Al 18R single crystals. Scripta Mater. 2001;45(7):853–8.
[341] Besag F, Smallman R. Discontinuous yielding in ordering alloys. Acta Metall 1970;18(4):429–35.
[342] Suzuki H. Chemical interaction of solute atoms with dislocations. Science Reports of the Research Institutes, Tohoku University. Ser. A, Physics, Chemistry and Metallurgy 1952;4:455–63.
[343] Schoeck G. The cold work peak. Scr. Metall. 1982;16(3):233–9.
[344] Mannan S, Rodriguez P. Strain-ageing in disordered CuAu. The Philosophical Magazine: A Journal of Theoretical Experimental and Applied Physics 1972;25(3):673–86.
[345] Chiba A, Kim M. Suzuki segregation and dislocation locking in supersaturated Co-Ni-based alloy. Mater. Trans. 2001;42(10):2112–6.
[346] Hooshmand M, Ghaziseidi M. Solute/twin boundary interaction as a new atomic-scale mechanism for dynamic strain aging. Acta Mater 2020;188:711–9.
[347] Smith T, et al. Segregation and ηphase formation along stacking faults during creep at intermediate temperatures in a Ni-based superalloy. Acta Mater 2015;100:19–31.
[348] Makineni S, et al. Elemental segregation to antiphase boundaries in a crept CoNi-based single crystal superalloy. Scripta Mater. 2018;157:62–6.
[349] Makineni S, et al. On the diffusive phase transformation mechanism assisted by extended dislocations during creep of a single crystal CoNi-based superalloy. Acta Mater 2018;155:362–71.
[350] Viswanathan G, et al. Segregation at stacking faults within the γ′phase of two Ni-base superalloys following intermediate temperature creep. Scripta Mater. 2015;94:5–8.
[351] Titus M, et al. High resolution energy dispersive spectroscopy mapping of planar defects in L12-containing Co-base superalloys. Acta Mater 2015;89:423–37.
[352] Eurich N, Bristowe P. Segregation of alloying elements to intrinsic and extrinsic stacking faults in γ′-Ni3Al via first principles calculations. Scripta Mater. 2015;102(1):87–90.
[353] Barba D, et al. Segregation assisted plasticity in Ni-based superalloys. Metallurgical and Materials Transactions A 2018;49:4173–85.
[354] Vorontsov V, et al. High-resolution electron microscopy of dislocation ribbons in a CMSX-4 superalloy single crystal. Acta Mater 2012;60:4866–78.
[355] Zener C, Hollomon J. Effect of strain rate upon plastic flow of steel. J. Appl. Phys. 1944;15(1):22–32.
[356] Kubin L, et al. Computer simulation of the low temperature instability of plastic flow. Acta Metall 1982;30(2):385–94.
[357] Zaiser M. Spatio-temporal aspects of low temperature thermomechanical instabilities: a model based on dislocation dynamics. Appl. Phys. A 1993;57(2):143–51.
[358] Tabin J, et al. Strain localization during discontinuous plastic flow at extremely low temperatures. Int. J. Solids Struct. 2016;97:593–612.
[359] Christian J, Mahajan S. Deformation twinning. Prog. Mater. Sci. 1995;39(1–2):1–157.
[360] D. Zhang et al. Deformation twinning (update). Reference Module in Materials Science and Materials Engineering, 2016.
[361] Boucher N, Christian J. The influence of pre-strain on deformation twinning in niobium single crystals. Acta Metall 1972;20(4):581–91.
[362] Thornton P, Mitchell T. Deformation twinning in alloys at low temperatures. The Philosophical Magazine: A Journal of Theoretical Experimental and Applied Physics 1962;7(75):361–75.
[363] Suzuki H, Barret C. Deformation twinning in silver-gold alloys. Acta Metall 1962;6(3):156–65.
[364] McRickard S. Twinning deformation in iron at 4 K. Phys. Status Solidi B 1966;18(1):89–97.
[365] Remy L. Kinetics of f.c.c. deformation twinning and its relationship to stress-strain behaviour. Acta Metall 1978;26(3):443–51.
[366] Krishnamurthy S, et al. Effects of deformation twinning on the stress-strain curves of low stacking fault energy face-centered cubic alloys. Practical Applications of Quantitative. Metallography 1984:41–64.
[367] Venables J. The electron microscopy of deformation twinning. J. Phys. Chem. Solids 1964;25(7):691–2.
[368] Meyers M, et al. The onset of twinning in metals: a constitutive description. Acta Metall 2001;49(19):4025–39.
[369] Bolling G, Richman R. Continual mechanical twinning: Part I: formal description. Acta Metall 1965;13(7):709–22.
[370] Richman R, Bolling G. Stress, deformation, and martensitic transformation. Metallurgical Transactions 1971;2(9):2451–62.
[371] Nilles J, Owen W. Deformation twinning of martensite. Metallurgical Transactions B 1972;3(7):1877–83.
[372] Pu E, et al. Effects of temperature and strain rate on tensile deformation behavior of superalloy UNS N10276. Mater. Sci. Eng., A 2017;699:88–98.
[373] Hornqvist M, et al. Dynamic strain aging in Haynes 282 superalloy. MATEC Web of Conferences 2014;14:16002.
[374] Shankar V, et al. Occurrence of dynamic strain aging in Alloy 617M under low cycle fatigue loading. Int. J. Fatigue 2017;100(1):12–20.
[375] Nembach E. The high temperature peak of the yield strength of γ′-strengthened superalloys. Materials Science and Engineering: A 2006;429(1–2):277–86.
[376] Singh R, Sahu J. Yield strength anomaly and dynamic strain ageing behaviour of recently developed advanced ultrasupercritical boiler grade wrought Ni-based superalloy IN 740H. Mater. High Temp. 2018;1878–6413.
[377] Hrutkay K, Kaoumi D. Tensile deformation behavior of a nickel based superalloy at different temperatures. Materials Science and Engineering: A 2014;599:196–203.
[378] Kaoumi D, Hrutkay K. Tensile deformation behavior and microstructure evolution of Ni-based superalloy 617. J. Nucl. Mater. 2014;454:265–73.
[379] Mo K, et al. Mechanism of plastic deformation of a Ni-based superalloy for VHTR applications. Jounal of Nuclear Materials 2013;441:695–703.
[380] Baird J. The effects of strain-ageing due to interstitial solutes on the mechanical properties of metals. Metallurgical Reviews 1971;16(1):1–18.
[381] Visweswara Rao C, et al. Dynamic strain aging, deformation and fracture behaviour of the nickel base superalloy Inconel 617. Materials Science and Engineering: A 2019;742:44–60.
[382] K. Bhanu Sankara Rao et al. Strain rate and temperature dependence of deformation and fracture behaviour of a Nimonic PE 16 superalloy. High Temperature Materials and Processes, 7(1):63–81, 1986.
[383] Mannan S. Role of dynamic strain ageing in low cycle fatigue. Bull. Mater. Sci. 1993;16(6):561–82.
[384] Jadav J, et al. Effects of strain rate and temperature on tensile properties, deformation and dynamic strain ageing behavior of Ni-base superalloy Superni 263. INAE Letters 2019;4:241–50.
[385] Wilcox B, Smith G. The Portevin-Le Chatelier effect in hydrogen charged nickel. Acta Metall 1964;12(4):371–6.
[386] Bergström Y, Roberts W. The application of a dislocation model to dynamical strain ageing in α-iron containing interstitial atoms. Acta Metall 1971;19(8):815–23.
[387] Bergström Y. A dislocation model for the strain-ageing behaviour of steel. Materials Science and Engineering 1972;9:101–10.
[388] R. Smallman. Modern physical metallurgy and materials engineering. Elsevier, 1 edition, 1999.
[389] Leslie W. Iron and its dilute substitutional solid solutions. Metallurgical and Materials Transactions B 1972;3(1):5–26.
[390] Ekaputra A, et al. Influence of dynamic strain aging on tensile deformation behaviour of alloy 617. Nuclear Engineering and Technology 2016;48(6):1387–95.
[391] Gupta C, et al. Effect of serrated flow on deformation behaviour of AISI 403 stainless steel. Materials Science and Engineering: A 2000;292(1):49–55.
[392] Zheng L, et al. Mechanism of intermediate temperature embrittlement of Ni and Ni-based superalloys. Crit. Rev. Solid State Mater. Sci. 2012;37(3):181–214.
[393] H. Hanninen et al. Dynamic strain aging of Ni-base alloys Inconel 600 and 690. Proceedings of the 12th International Conference on Environmental Degradation of Materials in Nuclear Power System, pages 1423–1430, 2005.
[394] Thomason P. A theory for the effects of strain-rate-sensitivity on ductile fracture. Metal Science Journal 1969;3(3):139–41.
[395] Jobba M, et al. Flow stress and work-hardening behaviour of Al–Mg binary alloys. Int. J. Plast 2015;65:43–60.
[396] Srinivas M, et al. Influence of dynamic strain ageing on mixed mode I/III fracture toughness of Armco iron. Mater. Sci. Eng., A 2007;443:132–41.
[397] Pardoen T, Brechet Y. Influence of microstructure-driven strain localization on the ductile fracture of metallic alloys. Phil Mag 2004;84(3–5):269–97.

[398] Y. Brechet. Plastic instabilities and their relation to fracture. Fundamental Aspects of Dislocation Interactions, pages 35–41, 1993.
[399] Graff S, et al. Finite element simulations of dynamic strain ageing effects at V-notches and crack tips. Scripta Mater. 2005;52(11):1181–6.
[400] Rodriguez P, Valsan M. High temperature low cycle fatigue. Sadhana 1995;20(1):123–64.
[401] K. Bhanu Sankara Rao et al. Dynamic strain ageing effects in low cycle fatigue. High Temperature Materials and Processes, 7(2):171–177, 1986.
[402] Kanazawa K, et al. Mapping of low cycle fatigue mechanisms at elevated temperatures for an austenitic stainless steel. Tetsu-to-Hagane 1988;74(6).
[403] Weisse M, et al. The cyclic deformation and fatigue behaviour of the low carbon steel SAE 1045 in the temperature regime of dynamic strain ageing. Acta Metall Mater 1993;41(7):2227–33.
[404] K. Bhanu Sankara Rao et al. On the low cycle fatigue deformation of Haynes 188 superalloy in the dynamic strain aging regime. Scripta Metallurgica et Materialia, 33(6):1005–1012, 1995.
[405] M. Gerland et al. Dislocation structure and corduroy contrast in a 316L alloy fatigued at (0.3–0.5) Tm. Fundamental Aspects of Dislocation Interactions, pages 226–229, 1993.
[406] Jadav J, et al. Strain controlled isothermal low cycle fatigue life, deformation and fracture characteristics of Superni 263 superalloy. Mater. Sci. Eng., A 2019; 760:296–315.
[407] J. Jadav et al. Comprehensive assessment of low cycle fatigue behavior of nickel-base superalloy Superni 263 in the range 298–1023 K. Transactions of the Indian National Academy of Engineering, 2020.
[408] K. Bhanu Sankara Rao et al. On the low cycle fatigue deformation of haynes 188 superalloy in the dynamic strain aging regime. Metallurgical and Materials Transactions A, 28:347–364, 1997.
[409] Srinivasan V, et al. Effects of temperature on the low cycle fatigue behaviour of nitrogen alloyed type 316L stainless steel. Int. J. Fatigue 1991;13(6):471–8.
[410] Srinivasan V, et al. High temperature time-dependent low cycle fatigue behaviour of a type 316L(N) stainless steel. Int. J. Fatigue 1999;21(1):11–21.
[411] Coffin L. The effect of quench aging and cyclic-strain aging on low carbon steel. J. Basic Eng. 1965;87(2):351–62.
[412] Robinson J, Shaw M. The influence of specimen geometry on the Portevin-Le Chatelier effect in an Al-Mg alloy. Materials Science and Engineering: A 1992;159 (2):159–65.
[413] Zdunek J, et al. The influence of specimens geometry on the PLC effect in Al–Mg–Mn (5182) alloy. Mater. Charact. 2007;58(1):46–50.
[414] Abbadi M, et al. On the characteristics of Portevin–Le Chatelier bands in aluminum alloy 5182 under stress-controlled and strain-controlled tensile testing. Materials Science and Engineering: A 2002;337(1):194–201.
[415] Hörnqvist M, Karlsson B. Temperature and strain rate dependence of the dynamic strain aging effect in an Al–Zn–Mg alloy. Mater. Sci. Technol. 2006;22(2): 213–22.
[416] Kovaks Z, et al. Localized deformation bands in Portevin-Le Chatelier plastic instabilities at constant stress rate. Materials Science and Engineering: A 2000;279 (1):179–84.
[417] F. Klose. Experimental and numerical studies on the Portevin-Le Chatelier effect in Cu-Al and Al-Mg in strain and stress controlled tensile tests. PhD Thesis, Verlag, 2004.
[418] Chmelik F, et al. Investigating the Portevin-Le Chatelier effect in strain rate and stress rate controlled tests by acoustic emission and laser extensometry techniques. Materials Science and Engineering: A 2007;462(1):53–60.
[419] Lebyodkin M, et al. Kinetics and Statistics of Jerky Flow: Experiments and Computer Simulations. Mater. Sci. Eng., A 1997;234–236:115–8.
[420] A. Karimi. Etude sur machine molle de la d éformation plastique h étérogéne cas d'un acier austénitique. PhD Thesis, Ecole des Mines de Paris, 1981.
[421] Balik F. The onset of Portevin-Le Chatelier instabilities in tensile testing. Mater. Sci. Eng., A 2001;316:102–8.
[422] Canadinc D, et al. On the negative strain rate sensitivity of Hadfield steel. Scripta Mater. 2008;59(10):1103–6.
[423] Mohammed S, Chen D. Effect of auto-tuning on serrated flow behaviour. Metals 2019;9(845).
[424] Clarke D, Hinton C. Adaptive control of materials-testing machines. Automatica 1997;33(6):1119–31.
[425] Lin Y, et al. Effects of initial microstructures on serrated flow features and fracture mechanisms of a nickel-based superalloy. Mater. Charact. 2018;144(1): 9–21.
[426] Marsh C, Kaoumi D. Serrated tensile flow in Inconel x750 sheets: effect of heat treatment. Mater. Sci. Eng., A 2017;707:136–47.
[427] Yuan L, et al. Mechanical properties and Portevin-Le Chatelier effect of a Ni-Cr-Mo alloy containing ordered phase with Pt2Mo-type structure at elevated temperature. Mater. Sci. Eng., A 2017;680(1):115–20.
[428] Koul A, Pickering F. Serrated yielding in Ni-Fe base superalloys at 700 C. Scr. Metall. 1982;16(2):119–24.
[429] Chen W, Chaturvedi M. On the mechanism of serrated deformation in aged Inconel 718. Materials Science and Engineering: A 1997;229(1–2):163–8.
[430] Chung D, et al. The characteristics of the barrier during serrated yielding in the γ′ precipitation hardened superalloys (Co-Ni-Cr-Ti system). Acta Metall 1976;24 (3):227–32.
[431] Pink E, et al. Serrated flow of aluminium alloys influenced by precipitates. Mater. Sci. Eng., A 2000;280:17–24.
[432] Tian B. Ageing effect on serrated flow in Al-Mg alloys. Mater. Sci. Eng., A 2003;349:272–8.
[433] Zhang G, et al. Influence of the γ′-phase morphology on the Portevin-Le Chatelier effect in a Ni-Co base superalloy. J. Mater. Sci. 2018;32(9):647–54.
[434] Cui C, et al. Effects of heat treatments on the serrated flow in a Ni–Co–Cr-base superalloy. J. Mater. Sci. 2011;46(16):5546–52.
[435] Kumar S, et al. Influence of precipitation on serrated flow in Al-5Zn-1Mg alloy. Mater. Sci. Technol. 2003;19:1344–8.
[436] Harun H, McCormick P. Effect of precipitation hardening on strain rate sensitivity and yield behaviour in an Al-Mg-Si Alloy. Acta Metall 1978;27:155–9.
[437] Thevenet D, et al. Characteristics of the propagating deformation bands associated with the Portevin-Le Chatelier effect in an Al-Zn-Mg-Cu alloy. Materials Science and Engineering: A 2000;291:110–7.
[438] Zhemchuzhnikova D, et al. Unusual behavior of the Portevin–Le Chatelier effect in an AlMg alloy containing precipitates. Mater. Sci. Eng., A 2015;639:37–41.
[439] Lebedkina T, et al. Effect of equal channel angular pressing on the Portevin–Le Chatelier effect in an Al3Mg alloy. Materials Science and Engineering: A 2014; 615:7–13.
[440] Sachdev A. Dynamic strain ageing of various steels. Metall. Trans. A 1982;13(10):1793–7.
[441] Ait-Amokhtar H, et al. Spatiotemporal aspects of jerky flow in Al–Mg alloys, in relation with the Mg content. Scripta Mater. 2006;54(12):2113–8.
[442] Horvath G, et al. Solute concentration dependence of strength and plastic instabilities in Al-Mg alloys. J. Mater. Res. 2004;20(2):331–7.
[443] Kral R, Lukac P. Modelling of strain hardening and its relation to the onset of Portevin-Le Chatelier effect in Al-Mg alloys. Materials Science and Engineering: A 1997;234:786–9.
[444] Cai Y, et al. Investigation of Portevin–Le Chatelier band strain and elastic shrinkage in Al-based alloys associated with Mg contents. Journal of Materials Science & Technology 2017;33(6):580–6.
[445] Onodera R, et al. The relation between the Portevin-Le Chatelier effect and the solid solubility in some binary alloys. Acta Metall 1983;31(4):535–40.
[446] Onodera R, et al. The Portevin-Le Chatelier effects in Cu-Ti, Cu-P and Cu-Si alloys. Acta Metall 1984;32(5):817–22.
[447] Chaturvedi M. Jerky flow in Co-Ni-Cr-C FCC alloys. Metallurgical and Materials Transactions B 1972;3(2):587–8.
[448] Grant B, et al. The effect of γ′ size and alloy chemistry on dynamic strain ageing in advanced polycrystalline nickel-based superalloys. Materials Science & Engineering A 2013;573:54–61.
[449] Rai R, Sahu J. Mechanism of serrated flow in a cast nickel base superalloy. Mater. Lett. 2018;210:298–300.
[450] E. Brandes and G. Brook. Smithels metal reference book. Reed Elsevier, 7 edition, 1992.
[451] Karunaratne M, Reed R. Interdiffusion of niobium and molybdenum in nickel between 900–1300°C. Defect and Diffusion forum 2005;230:420–5.
[452] Jung S, et al. Interdiffusion and its size effect in nickel solid solutions of Ni-Co, Ni-Cr and Ni-Ti systems. J. Mater. Sci. Lett. 1992;11:1333–7.
[453] Manikandan P, et al. High temperature tensile behavior of a nickel-based superalloy 55Ni-17Cr-12Fe-9Mo-2Nb-1.5Al used in launch vehicle applications. J. Mater. Eng. Perform. 2019;29(1):377–90.
[454] Max B, et al. Atomic species associated with the Portevin–Le Chatelier effect in superalloy 718 studied by mechanical spectroscopy. Metallurgical and Materials Transactions A 2018;49(6):2057–69.

[455] Gao Z, et al. Development of fine-grained structure in Ni-Cr-W based superalloy and its effect on the mechanical properties. Materials Science and Engineering: A 2017;682:156–63.

[456] S. Dymek et al. Effects of long range ordering, temperature and strain rate on deformation behaviour of a Ni-Mo-Cr alloy. Superalloys 1992, TMS, pages 685–694, 1992.

[457] Li X, et al. Effect of twins on the moderate temperature tensile deformation of a strengthened Fe-based superalloy. J. Alloy. Compd. 2009;467:383–9.

[458] Li Z, et al. Grain size dependence of the serrated flow in a nickel based alloy. Mater. Lett. 2015;150:108–10.

[459] Koizumi Y, et al. Suzuki segregation in Co–Ni-based superalloy at 973 K: an experimental and computational study by phase-field simulation. Acta Mater 2012; 60(6–7):2901–15.

[460] Zhang R, et al. Portevin-Le Chatelier effect in a wrought Ni-Co based superalloy. J. Alloy. Compd. 2020;818:152863.

[461] Jiang Z, et al. The mechanism for the serrated flow induced by Suzuki segregation in a Ni alloy. Materials Science and Engineering: A 2021;820:141575.

[462] D. McAllister. Shearing mechanisms and complex particle growth in nickel superalloy 718. PhD Thesis, Ohio State University, 2016.

[463] Charnock W. The influence of grain size on the nature of Portevin-Le Chatelier yielding. The Philosophical Magazine: A Journal of Theoretical Experimental and Applied Physics 1968;18(151):89–99.

[464] Miura S, Yamauchi H. Influence of grain size on the Portevin-Le Chatelier effect in Al-Mg alloys. Transactions of the Japanese Institute of Metals 1972;13(2): 82–8.

[465] McCormick P. Effect of grain size on serrated yielding in an Al-Mg-Si alloy. Phil Mag 1971;23(184):949–56.

[466] Narutani T, Takamura J. Grain size strengthening in terms of dislocation density measured by resistivity. Acta Metall Mater 1991;39(8):2037–49.

[467] Fujita H, Tabata T. Discontinuous deformaton in Al-Mg alloys under various conditions. Acta Metall 1977;25:793–800.

[468] Worthington P, Brindley B. Serrated yielding in aluminium-3% magnesium. Acta Metall 1969;17:1357–61.

[469] Koyama M, et al. Inverse grain size dependence of critical strain for serrated flow in a Fe-Mn-C twinning-induced plasticity steel. Philos. Mag. Lett. 2013;92(3): 145–52.

[470] Qian L, et al. Unusual grain-size and strain-rate effects on the serrated flow in FeMnC twin-induced plasticity steels. J. Mater. Sci. 2013;48:1669–74.

[471] Liu H, et al. Effect of grain size on dynamic strain aging behavior of C-bearing high Mn twinning-induced plasticity steel. Journal of Materials Research and Technology 2021;15:6387–94.

[472] Tian C, et al. Effect of solution treatment on the inverse dynamic strain aging of a Ni-Co base superalloy. Acta Metall Sin 2012;48(10):1223–8.

[473] Gabb T, et al. Orientation and temperature dependence of some mechanical properties of the single-crystal nickel-base superalloy René N4. Metall. Trans. A 1986;17(3):491–505.

[474] Beese A, et al. Absence of DSA in an additively manufactured nickel-base superalloy. Nature Communications 2018;9:2083.

[475] Varin R, et al. Discontinuous yielding in ultrafine-grained austentic stainless steels. Materials Science and Engineering 1987;94:109–19.

[476] Rosen A. Strain ageing of commercially pure aluminium. Materials Science and Engineering 1967;2:117–24.

[477] Weinstein A, et al. Dynamic strain aging of carbon doped Ni. Materials Science and Engineering 1971;8(4):198–202.

[478] Bolling G. Yield point phenomena in alpha brass and other face-centred cubic metals. The Philosophical Magazine: A Journal of Theoretical Experimental and Applied Physics 1959;4(41):537–59.

[479] Cribb W, Reed-Hill R. Static strain-aging in nickel 200 between 373 and 473 K. Metall. Trans. A 1977;8(1):71–6.

[480] Haasen P, Kelly A. A yield phenomenon in face-centered cubic single crystals. Acta Metall 1957;5(4):192–9.

[481] Birnbaum H. Unloading effects in crystals- the unloading yield point effect. Acta Metall 1961;9(4):320–6.

[482] Brown L. An interpretation of the Haasen-Kelly effect. Phil Mag 2010;90(31–32):4147–52.

[483] Marin M. Unloading effects in the plastic properties of copper single crystals. Phil Mag 1957;3(27):287–301.

[484] Titchener A, Davies G. Yield phenomena in polycrystalline copper. Philos Magaz: A J Theor Exp Appl Phys 1964;11(114):1225–32.

[485] Talonen J, et al. Static strain ageing of cold-worked austenitic stainless steel. High Nitrogen Steels-Int Conf 2004:113–22.

[486] De A, et al. Static strain aging behavior of ultra low carbon bake hardening steel. Scripta Mater 1999;41(8):831–7.

[487] Yuanyuan Y, et al. An overview of strain ageing in low carbon steels. Baosteel Tech Res 2014;8(2):55.

[488] Lebyodkin M, et al. On the similarity of plastic flow processes during smooth and jerky flow in dilute alloys. Acta Mater 2012;60(3):844–50.